Confocal Microscopy, Calorimetry and Permeability Studies on Giant Lipid Vesicles Containing Ceramides

Matthias Fidorra

PhD Thesis

MEMPHYS
Department of Physics and Chemistry
University of Southern Denmark
September 2007

Department of Physics and Chemistry
University of Southern Denmark

Campusvej 55, ▪ 5230 Odense M, Denmark Telephone: (+45) 6550 1000

Confocal Microscopy, Calorimetry and Permeability Studies on Giant Lipid Vesicles Containing Ceramides

By

Matthias Fidorra

Supervised by:

Professor Ole G. Mouritsen
Associate Professor Luis A. Bagatolli
Professor Thomas Heimburg

Thesis Submitted to the Faculty of Science, University of Southern Denmark , to fulfill the requirements for the PhD degree.

September, 2007

Preface

This thesis is submitted in partial fulfillment of the requirements for obtaining the Ph.D. degree in physics at the University of Southern Denmark. The thesis contains work in the field of membrane biophysics, with focus on lipid phase transitions and lipid membrane permeability. The work has been carried out at MEMPHYS - Center for Biomembrane Physics, Department of Physics and Chemistry, University of Southern Denmark in Odense and the Membrane Biophysics Group at the Niels Bohr Institute at the University of Copenhagen, Denmark. The research was done in the period from September 2004 to September 2007. Parts of the work were performed at the Jacobs University of Bremen (the former International University of Bremen) in the periods from January to March 2006 and from January to February 2007. In addition, a projected was performed in cooperation with the faculty of medicine at the University of Santiago. In relation with this work a short term visit of two weeks in Santiago was arranged in July 2007, to perform experiments and to get introduced to the data processing procedure.

This thesis is based on the following publications and preprints:

M. Fidorra, **L. Duelund**, **C. Leidy**, **A. C. Simonsen** and **L. A. Bagatolli**. (2006). Absence of Fluid-Ordered/Fluid-Disordered Phase Coexistence in Ceramide/POPC Mixtures Containing Cholesterol. *Biophys. J.* 90:4437–4451.

M. Fidorra and **L. A. Bagatolli** Fluid-Ordered/Fluid-Ordered Phase Coexistence in Cerebroside/POPC Mixtures Containing Cholesterol. *(in preparation)*

M. Fidorra, **T. Heimburg** and **H. Seeger**. Melting of Single Components in Binary Lipid Mixtures: A Comparison between FTIR Spectroscopy and Monte Carlo Simulations. *(in preparation)*

M. Fidorra, **R. Hartley**, **L. A. Bagatolli** and **S. Härtel**. Do Domains in Giant Unilamellar Vesicles Composed of Binary Lipid Mixtures Obey The Lever Rule? *(in preparation)*

Acknowledgements

This thesis obtains results from a variety of experiments on specialized devices at diverse locations. Therefore a lot of traveling and coordination was necessary. I would like to thank my supervisors, Ole G. Mouritsen, Luis A. Bagatolli and Thomas Heimburg for supporting all these journeys and for finding financial support for these projects. Additionally, they were always encouraging my work with their expertise in theory and experiments.
I would like to thank all MEMPHYS people for making MEMPHYS such a cosy place. Their office doors are open to anybody and there are no barriers to start discussions right away. A special thanks goes out to Lars Duelund, the lab manager. He was kindly around to order the things I needed and he helped with valuable hints on experimental setups and techniques. Another person I am grateful to is Inés Plasencia-Gil. She knew where I stock my things and so she usually was the person I addressed first if I forgot something during my various travels.
Most of my time I spent in Odense, but for several separated periods of time I stayed at the Niels Bohr Institute in Copenhagen. I thank the people of the Membrane Biophysics group for always welcome me warmly and keeping me up to date with their research progress.
Mathias Winterhalter agreed instantly when I asked him to introduce me to the Black Lipid Membrane technique. He hosted me twice at the School of Engineering and Science at the international University of Bremen. His expertise made the studies for the chapter on Black Lipid membranes possible, what I appreciate very much. Additionally, I want to thank all his students and the people in his lab for creating a nice atmosphere. Catalin Chimerel and Tivadar Mach have to be highlighted, because they shared their setups with me and followed the experiments with suggestions.
I would like to thank the people from the Anatomy and Developmental Biology Program at the Faculty of Medicine of the University of Santiago for making my short stay there a successful one. They arranged everything within short term to enable the experiments. Especially Alejandra Garcia has to be named, as she provided a replacement microscope when the setup which was designated to perform the experiments broke completely. Steffen Härtel, who was hosting me together with Alejandra made my journey a successful one. He arranged everything perfectly and always helped to find solutions to the problems which occurred. He introduced me into the evaluation of the confocal data and spent most of his time in pushing the data processing in order to get the results.
I would like to thank Heiko Seeger for being a very good lab mate and friend since I started my diploma thesis at the University of Göttingen. He spent a lot of time in proofreading my thesis.

I am grateful to all the people of the workshops at BMB of the University of Southern Denmark and at the Niels Bohr Institute of Copenhagen. They make proper constructions out of my plans and drawings and their skilled work made my experiments possible.

Finally, I would like to thank BioNet, the Villum Kann Rasmussen Foundation and Leo Pharma for financial support.

0.1 Abstract

Melting processes in lipid membranes lead to increased changes in heat capacity, enthalpy, entropy and compressibility of the membranes. These variables depend on the fluctuations of the system. The fluctuations are highest in the melting transition. Domain formation accompanies these events on different length scales.
A molecule which has great impact on lipid phase transitions is cholesterol and it seems to be a molecule with great importance in biological systems. It is abundant in most natural tissue. Within this thesis, model membranes which are composed of mixtures of synthetic lipids and lipid mixtures containing lipids extracted from natural tissues are investigated. The extracted lipids contain a mixture of lipids with different chainlength and therefore are no binary or ternary mixtures in the narrower sense anymore. Therefore this approach is a first step to understand the behavior of the more complicated biological membranes. This thesis concentrates on the lateral phase separation of lipid membranes. An emphasis is put on the impact of cholesterol to binary lipid mixtures. Additionally, experimental results obtained for binary lipid mixtures are put in relation to theoretical models in order to verify theoretical predictions. Furthermore, the temperature dependence of fluctuations is investigated in terms of membrane permeability.
The experiments which provide the results for this thesis were performed on different experimental setups, such as Confocal Fluorescence Microscopy, Two Photon Fluorescence Excitation Microscopy, Differential Scanning Calorimetry, Fourier Transform Infra Red Spectroscopy, Atomic Force Microscopy and conductance measurements on Black Lipid Membranes[1].
In the case of Fourier Transform Infra Red Spectroscopy, a new data analysis of lipid melting spectroscopic data is presented. The experimental results are accompanied by Monte Carlo simulations[2] and it is shown that the simulations serve a link to relate spectroscopic and calorimetric results. Additionally, a new technique is applied to Giant Unilamellar Vesicles to calculate gel/fluid area fractions. These results are compared to values predicted from thermodynamics. The studies presented here deepen the understanding of potential processes that might occur in biological membranes.

[1] In the study about POPC/ceramides in chapter 4 L. A. Bagatolli, L. Duelund, A. C. Simonsen and C. Leidy contributed with experimental results
[2] The simulations were performed by H. Seeger

0.2 Dansk resumé

Smelteprocesser fører til støre ændringer i varmekapacitet, entalpi og kompressibilitet af lipidmembranerne. Disse variabler afhænger af fluktuationer af systemet. Fluktuationerne er størst ved faseovergangen og domænedannelse sker på grund af fluktuationerne på forskellige størrelsesordner.
Et molekyle som har stor indflydelse på lipid faseovergangen er kolesterol. Kolesterol har en stor indvirkning på et bred spektrum af biologiske systemer og findes desuden i det meste væv. I denne afhandling er der anvendt modelmembraner som er sammensæt af syntetiske lipidblandiger samt lipidblandinger indeholdene lipider ekstraheret af naturlig væv. De ekstraherede lipider indeholder et blanding af lipider med forskellige kædelængder og er derfor ikke blot en binær eller tertiær blænding. Denne fremgangsmåde er derfor et forsøg på at forstå opføreslen af mere komplicerede biologiske membraner. Fokus i denne afhandling er lagt på lateral faseadskillelse i lipidmembraner. Der er lagt vægt på kolesterols indflydelse på binære lipidblændinger. Der ud over er experimentelle resultater skaffet fra lipid blændinger sammenholdt med teoretiske modeller for at verificere de teoretiske forudsigelser. Endvidere er temperaturafhængigheden af fluktuationer undersøgt med hensyn til membranens permeabilitet. De forsøg blev udført ved hjælp af forskellige tekniker, såsom Confocal Fluorescence Microscopy, Two Photon Fluorescence Excitation Microscopy, Differential Scanning Calorimetry, Fourier Transform Infra Red Spectroscopy, Atomic Force Microscopy og målinger af ledningsevne på Black Lipid Membranes[3].
Der er desuden præsenteret en nye metode til dataanalyse for smelting af lipider undersøgt med FTIR. Eksperimentelle resultater er ledsagt af Monte Carlo simulationer[4] og det er vist at simuleringer kan sammenføre resultaterne fra spektroskopi og kalorimetri. Der er desuden introduceret en ny teknik anvendt på GUV'er til at beregne gel/fluid areal fraktioner. Resultaterne er sammenlignet med teoretiske termodynamiske værdier. De ovennævente studier skaber en forbedret forståelse af potentielle processer som muligvis forekommer i biologiske membraner.

[3] Indenfor studiet af POPC/ceramider i kapitel 4 har L. A. Bagatolli, L. Duelund, A. C. Simonsen and C. Leidy sammenlægt nogle experimentelle dater
[4] Simuleringer blev udført af H. Seeger

Contents

Part I

Fundamentals

Chapter 1

Introduction

1.1 The biological cell membrane

One of the basics of life is compartmentalization. Organisms, cells and organelles need compartmentalization to keep their function upright, as different functional entities need different environmental conditions, for example ion concentrations, pH, etc. Every cell is a compartment and every organelle is a compartment within a compartment. The structural unit separating space and thereby forming compartments in living organisms is the membrane. It is composed of a diversity of lipids, proteins and sugars. However, the membrane is not only a barrier. It is a highly complex functional entity that enables a controlled flow of molecules and macromolecules to keep the cells and therewith the organism alive: Ions have to be balanced to keep a voltage gradient between inside and outside a cell upright, vesicles have to fuse with the membrane in order to release their content to opposite side of the membrane, molecules bind from outside the membrane and induce reaction cascades within the cells, for example in apoptosis, etc. Besides separating space it has been suggested that the membrane confines the three dimensional space to a plane and therewith facilitates reactions by increasing the possibility of concurrence of reaction partners [1]. In former times, the proteins in the membrane were thought to be responsible for all the actions taking place on and in the membranes and the lipids were accepted as a matrix holding the proteins in place. Considering the diversity of lipids in biological membranes should perplex already. Lipids make up about 30-80 wt% of membrane mass and usually contain hundreds of different lipid species. Besides Proteins (20-60 wt%) sugars are also abundant in biological membranes (0-10 wt% of the membrane mass).

1.1.1 Lipids

As mentioned in the above section, the wealth of lipid species is stunning. Lipids are completely or in most instances water insoluble but dissolve well in hydrophobic solvents. Lipids are divided into seven classes, namely fatty acids, triglycerides, waxes, phospholipids, sphingolipids, lipopolysaccharides, and isoprenoids. Lipids have a diversity of biological functions as signal molecules, hormones, vitamins, cofactors, pigments and they serve as membrane bricks, energy provider and energy storage. Within this thesis only the membrane forming lipids of the class of phospholipids and sphingolipids are of interest, as well as the sterol cholesterol. For sake of simplification, the structure of a lipid is usually divided into the headgroup region, the backbone region and the tail region (see figure 1.1). The polar headgroup region can be uncharged, neg-

atively charged or zwitterionic. The carbon chains are uncharged and therefore unpolar. Lipids with one to three hydrocarbon chains exist, varying in chainlength and degree of saturation. The chains are connected to the headgroup via esther or amide bonds in the backbone region.

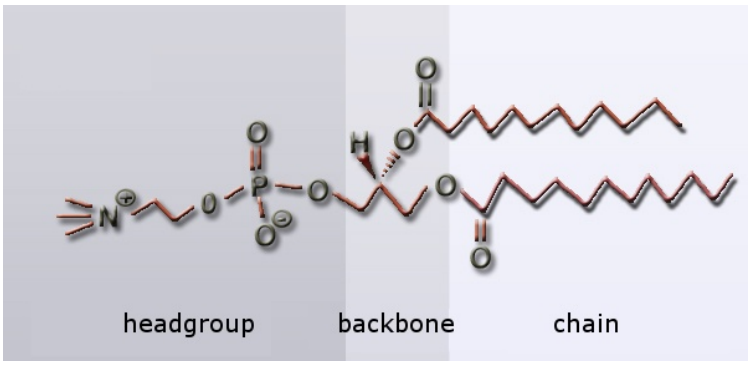

Figure 1.1
structure of the phospholipid DPPC.

Because of the hydrophobic character of the tail region, lipids form aggregates in polar solvents as water, since the contact of the methyl groups with water is energetically unfavorable. Within these aggregates the lipid headgroups face the water and the lipid chains face each other. Depending on the type of lipid, many structures are formed and some examples are shown in figure 1.2.

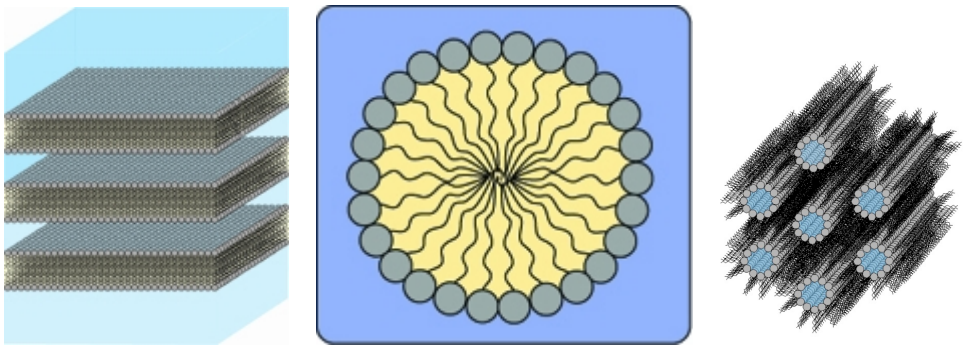

(a) Multi layered double layer (b) Micelle (c) Hexagonal

Figure 1.2
Lipids can form different structures in polar solvents in which the head groups face the water and the tails avoid to be in contact with water.

The structure of interest within this thesis is the lipid bilayer, usually in form of a planar membrane or a spherical vesicle. Depending on the experimental technique applied, single bilayers or multilayers are used, as will be described in chapter 3. With regard to unilamellar spherical vesicles, three sizes of vesicles are described in the literature: Small unilamellar vesicles (SUV), ranging from 1-100nm in diameter, large unilamellar vesicles (LUV), ranging from 100nm to 1µm and giant unilamellar vesicles (GUV) in the range from 1µm and larger.

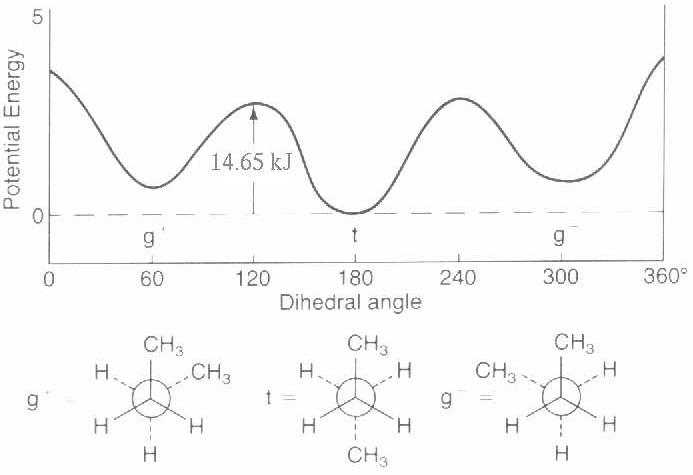

Figure 1.3
The potential energy between C-C bonds differs with rotation angle (dihedral angle). In the so-called *all-trans* configuration potential energy is in a global minimum and in the *gauche* confirmation the potential energy is a local minimum. *Figure taken from [2].*

The lipid chains can occur in different conformations as the C-C bindings can rotate if they are not hindered by double bonding. The potential energy of rotation around C-C bonds is shown in figure 1.3.
A lipid where all of the C-C bonds are in *all-trans* configuration is in an ordered state and a lipid with bonds in *gauche* configuration is in an unordered state. With regard to lipid membranes, the state of the lipid membrane depends on temperature. In the following we will consider a membrane consisting of a single lipid species, for example DPPC (see figure 1.1). At low temperatures all lipids in the membrane are in an ordered state and the arrangement of lipids is on a hexagonal lattice [3]. In this case the membrane is called *solid ordered* or a *gel*. If temperature is increased, a certain point will be reached where the lipids change from *all-trans* to *gauche* configuration and the lattice structure gets lost. In this case the membrane is called *liquid disordered* or *fluid*. The point where 50% of the lipids are ordered and 50% are disordered is called the transition midpoint. DPPC, for example, has a transition midpoint at 41.5°C. This point is called the melting point (T_m). During the melting transition the heat capacity, entropy and enthalpy of the lipid membrane system increases. The melting point depends on many factors, as for example the kind of lipid head group, lipid chain length and the degree of chain saturation [4–6], but also ionic strength and pressure [2].
Lipids show cooperative melting. Cooperative melting means that the melting of a lipid influences the melting of others. For membranes composed of single lipid species the melting cooperativity is highest.

The melting of lipid membranes is driven by competition between entropy and enthalpy. At high temperature the lipid chains show disorder and entropy is higher and at lower temperatures van der Waals interactions have the upper hand and the membrane is in gel. The balance between entropy and enthalpy is also affected by hydrogen bonding and by sterical aspects, such as bulky headgroups. The lipid melting transition temperature shifts to a higher temperature the longer the lipid chains are. Chain unsaturation lowers the melting temperature in comparison

to the saturated lipid, as rotation around double bonds is restricted. Therefore the order of the chains is lower [4–6]. During the melting transition the lipid area changes by about 25% and the membrane volume increases by about 4%. Ordered membranes are thicker than disordered membranes, the membrane thickness changes by about 1nm [7, 8]. In the phase transition the membrane permeability, compressibility and elasticity are maximal [9–11].

The melting cooperativity can be disturbed by other molecules dissolved in the membrane, for example other lipid species or peptides or cholesterol [12–14]. This will broaden the melting transition and areas with different properties will segregate laterally in the membrane. These areas are called phases and can be made vivid with microscopic techniques. In the case of lipid bilayers composed of a binary lipid mixture gel-fluid phase coexistence will occur (see figure 1.4).

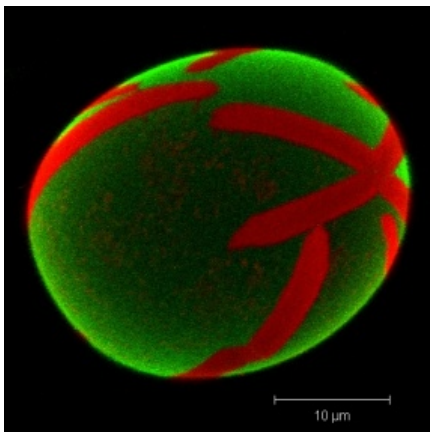

Figure 1.4
Confocal microscopy image of phase separation on a giant unilamellar lipid vesicle consisting of a binary lipid mixture at 20°C. The lipids used are DLPC/DPPC in a molar ratio of 30:70. Two different kinds of fluorescent lipid molecules showing preference for gel and fluid phase, respectively, are added to the membrane during vesicle preparation. Red areas correspond to gel phase domains and green areas correspond to fluid phase domains.

The interaction of steroids such as cholesterol with lipid membranes is special, as incorporation of small amounts of this molecule induces the formation of the so-called *liquid ordered* phase. This phase was first proposed by Ipsen in 1987 [15]. A model that tries to describe the cholesterol-lipid interactions is the *Umbrella Model* [16](see figure 1.5). Within this model the cholesterol is covered by the neighboring lipid headgroups to prevent exposure of the nonpolar cholesterol bodies to water. Cholesterol concentrations of more than 5% usually have an ordering effect on the lipid chains of liquid disordered membranes. Cholesterol in the gel phase disturbs the long range interactions so that the hexagonal lattice structure of the solid ordered phase is lost.

1.1.2 Membrane models

The widespread and accepted model of biological membranes is the *Fluid Mosaic Model* by Singer and Nicolson from 1972 [17] (see figure 1.6). This model describes the lipid bilayer as a homogeneous matrix where the proteins are embedded as transmembrane or peripheral proteins. In the vicinity of proteins and peptides, some kinds of lipids could be preferred to others, due to sterical restrictions or electrostatic interactions.
However, in 1969 calorimetric experiments already showed anomalies in heat capacity profiles of biological membranes. Based on these results lipid phase separation was suggested [18]. More calorimetric experiments were performed in the following years, also including synthetic lipids [19–23]. In 1977 Jain and White proposed a model implementing cluster formation of

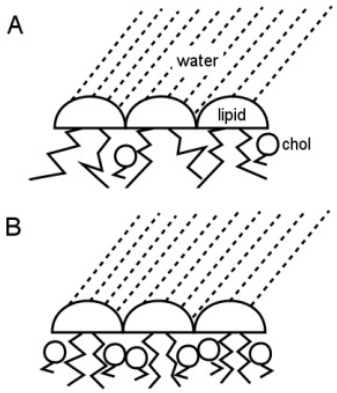

Figure 1.5
The umbrella model of Huang and Feigenson [16]. The lipid headgroups shield the small cholesterol molecule from the polar solvent. (*a*) At small cholesterol concentrations the lipid phase is not affected. (*b*) Increasing cholesterol concentration in the membrane leads to an ordering of the lipid chains. High cholesterol concentrations disturb the lattice structure of the solid ordered phase and the liquid ordered phase forms. *Figure taken from [16].*

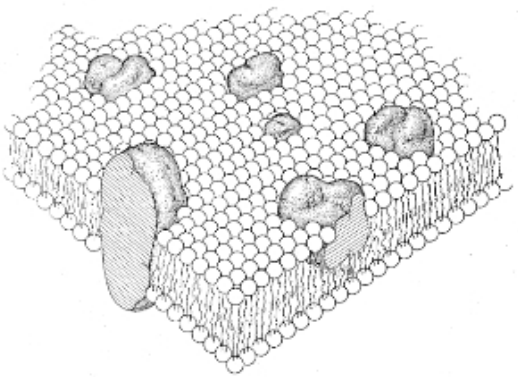

Figure 1.6
A biological membrane sketched after the *Fluid Mosaic Model* of Singer and Nicolson. The proteins are embedded in a homogeneous matrix of lipids. *Figure taken from [17].*

lipids, but this model did not gain much attention [24]. In 1984 Mouritsen and Bloom introduced the *Mattress Model* that allowed protein cluster formation in the membrane because the hydrophobic mismatch could force proteins to aggregate [25](see figure 1.7). The hydrophobic mismatch describes different length of hydrophobic parts of molecules that interact in a membrane. A strong mismatch of these parts is energetically unfavorable.
Fluorescence microscopy experiments on lipid monolayers made it clear that not only proteins could cluster, but also lipid molecules could separate laterally [26, 27]. These observations were also obtained with lipid bilayer systems later on [28, 29].
It was speculated that a structural change of the proteins in order to minimize the hydrophobic mismatch could alter or disturb their functioning [25, 30]. Indications of this come from experiments with PLA_2 that show that the latency period of PLA_2 activation is lowest in the phase transition of DPPC LUVs [31]. In 1997 Simons and Ikonen [32] proposed the existence of specialized domains, so called *rafts* that are supposed to be liquid ordered domains in a fluid environment. The existence of *rafts* is still under discussion and the main criticisms is that they might be formed during the special extraction process from the membrane [33].
What actually has been observed in model membrane systems composed of synthetic lipids and in model membrane systems composed of extracted natural lipids, are domains that range from

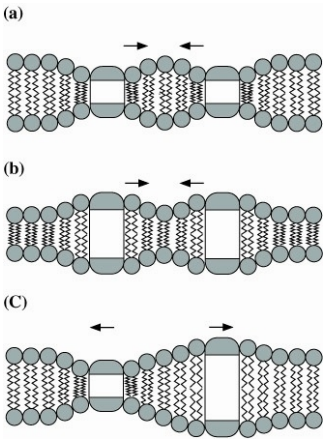

Figure 1.7
The hydrophobic mismatch between the hydrophobic parts of lipids and proteins could lead to aggregation of proteins (*a*,*b*) or to repulsion of proteins (*c*).

nanometers to micrometers in size. These domains were found by means of microscopy, such as light microscopy and atomic force microscopy (AFM) and also by fluorescence techniques such as Förster Resonance Energy Transfer (FRET) [28, 34–36]. A recent review discusses the observation of microdomains in bacterial membranes [37].
All in all, bearing in mind the experimental results from the past few years, it is clear that the lipid membrane is quite complex. It is not only a matrix to keep the proteins in place. It shows lateral heterogeneities, and in many cases these heterogeneities drive protein aggregation and alter protein function.

1.1.3 The stratum corneum of the skin

A very peculiar organ, where lipid membranes seem to have essential function, is the skin (see figure 1.8). The skin has the tricky challenge to keep the body from drying out by evaporation, but at the same time it has to help to control body temperature by evaporation. Additionally, the skin is the first barrier against intruders or dirt. The skin consists of different strata and its outermost layer is the stratum corneum (SC), which is the main barrier of the skin. It consists of an assembly of corneocytes and lamellar lipid bilayers, resembling a wall of mortar and bricks [38].
The corneocytes are completely flattened, dead cells that do not contain a nucleus or any cytoplasmic organelles. They consist of a very high fraction of keratin, a structure building protein and originate from a transformation of keratinocytes. Keratinocytes are the cells of the epidermis that are responsible for its renewal. During the transformation to corneocytes the keratinocytes are progressively filled by keratin. Keratin is a fibrous, water insoluble structural protein that accounts for 95% of all proteins in the epidermis. This protein gives the skin its protective function.
The lamellar lipid layers in between the corneocytes have to support the protective function of the corneocytes also, in order to make the stratum corneum a good barrier. The lipids found in the SC dominantly are ceramides, fatty acids and cholesterol. The most abundant chainlength of the SC ceramide lipids is C24-26, but also a small fraction with C16-C18 is present. Experiments indicate that most SC lipids form a gel phase, but a small subpopulation seems to form a fluid phase, too [39, 40]. In all mammalian stratum corneum tissue, a 13nm periodicity was detected with wide-angle X-Ray diffraction experiments of Bouwstra et al. [41]. This 13nm periodicity is a layering of bilayers with a crystalline outer part but a fluid central

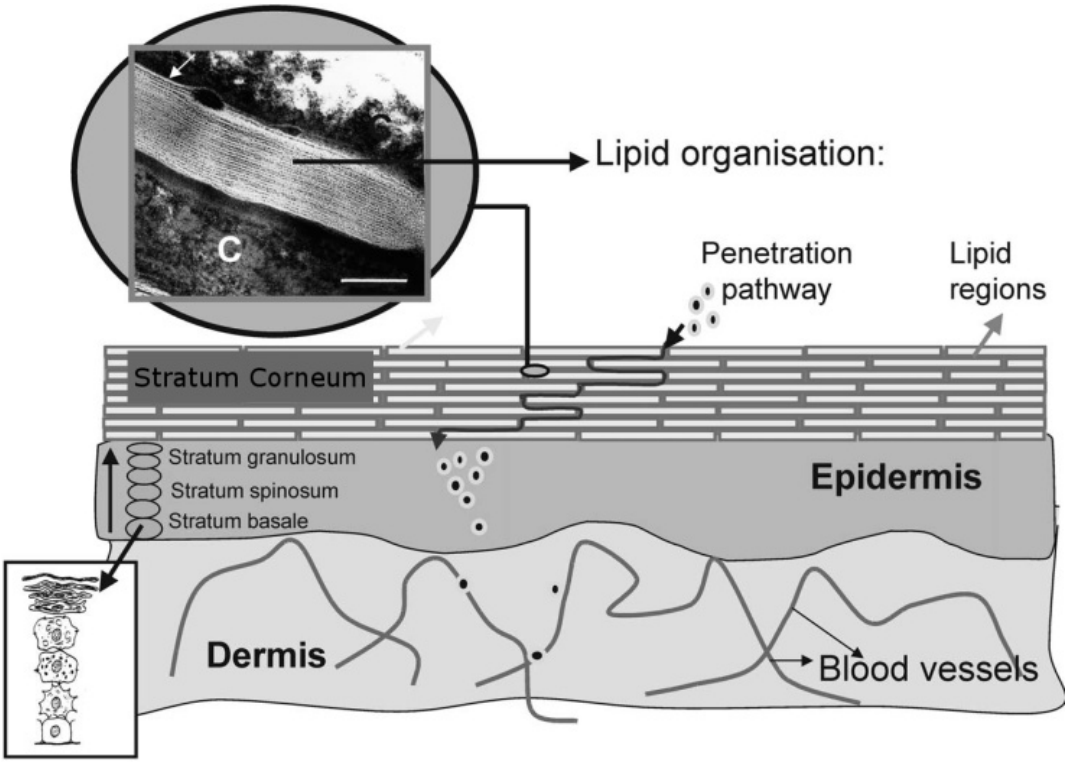

Figure 1.8
A sketch of a profile of mammalian skin. The skin consists of different layers, of which the Stratum Corneum (SC) is the outermost layer. The SC is the main barrier of the skin and consists of corneocytes and lipid membranes. Molecules which have to pass the skin barrier will pass through the lipid part of the SC. *Figure taken from [38].*

region. It is suggested that the crystalline structure serves the barrier function and the fluid phase makes the elastic properties of the skin [38].

As the lipid structures are reported to be the only continuous structure of the SC, substances applied onto the skin have to pass these regions. There are several approaches to facilitate the skin penetration of substances, for example by applying additional drugs that enhance the membrane fluidity or the drug solubility in the stratum corneum [42]. Vesicles can also be used as carriers for drugs [43]. Other techniques employ physical treatment, such as the use of an electrical gradient or electroporation [44, 45].

An interesting study on the diffusional transport over an oriented stack of membranes, such as those observed in the stratum corneum in between the corneocytes, was performed by Sparr and Wennerström [46]. They showed that a gradient in water chemical potential along a stack of membranes can change the phase behavior of the membranes and this affects the permeability of the membrane. This suggests that the lipid membranes of the SC are probably more fluid-like on the inside. On the outer layers water concentration is low and the membranes are likely more ordered. This leads to a non-linear water permeability, that matches experimental results well [46].

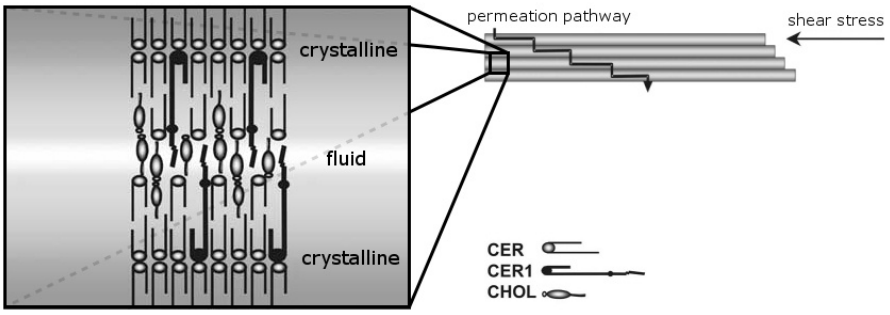

Figure 1.9
The sandwich model of the lamellar lipid layers in the skin. The long chain ceramides (CER1) make the 13nm spacing, cholesterol and the small chain ceramides (CER) induce fluidity in the central part. This sandwich structure serves the low permeability of the membrane but also its elasticity. *Figure taken from [38].*

1.1.4 The myelin sheath of the axons

A further membrane where it becomes clear that the absence of a lipid species has fatal effects for the organism, is the myelin membrane. The myelin membrane is an insulating membrane that surrounds the axon membrane of nerves in a multilayer assembly. Myelin consists to 80% of lipids whereof the major lipid component besides cholesterol are galactocerebrosides (20%). Experiments on mice have shown that mice that lack the galactocerebroside component in the myelin sheaf suffer from whole body tremor. Other fatal diseases related to myelination defects are multiple sclerosis and Krabbe's disease.
Nerve pulse propagation is faster in myelinated nerves than in unmyelinated. In myelinated nerves the myelin membrane is interrupted by ranvier nodes regularly, which results in a saltationary pulse propagation. It is in the ranvier nodes that the progressing action potentials are generated. In unmyelinated nerves the pules propagate in continuous waves. The widely accepted Hodgkin-Huxley [47] theory describes the pulse propagation on an electrical basis, but soliton propagation based theories are also discussed [48].

1.2 Motivation

The introduction of this thesis led the reader into the realm of lipids and emphasized that lipids are not simply bricks that build the membrane and keep proteins in place. A large diversity of lipids is found in biological membranes. Why so many different lipid species are necessary to form biological membranes is knot known yet in detail. However, the introduction to the stratum corneum in section 1.1.3 and the myelin sheath in section 1.1.4 indicate that the proper lipid species need to be present in order to assemble a membrane which is specialized to its particular function.
Additionally, there is increasing indications that the lipids do not only specialize the membrane itself. The function of proteins and enzymes seems to be related to the phase of lipid membranes also. Phase separation on the microscopic and macroscopic scale has been reported

from lipid model membranes [28, 29, 36], but is also discussed for native membranes [37]. The observation of macroscopic domain formation in model membranes composed of lung surfactant extracts strongly supports the prediction of domain formation processes in biological membranes [14]. Several authors speculate that domain formation could trigger or prevent signal cascades [49–51]. Cholesterol, that is abundant in most natural tissues, affects the phase behavior of lipid membranes strongly and is object of many studies. The influence of cholesterol to binary lipid mixtures is a hot topic right now.

This thesis is motivated by the investigations of the phase behavior of lipid model membranes composed of synthetic lipids and lipid extracts reported during the last decades. Model membranes strongly contribute to the establishment of theoretical models. However, the description of natural systems on a theoretical basis is yet too complicated. Generally theoretical works only concentrate on simple binary or ternary lipid mixtures. However, theory is a necessary tool to understand the basic mechanisms underlying natural systems. Natural systems are generally far too complex to separate the impact of a single lipid species to the system. Therefore, simple model membranes contribute valuable information about lipid-lipid and lipid-protein interactions which are difficult to detect in natural systems.
This thesis contributes to the characterization about binary lipid mixtures containing cholesterol and deepens the understanding of cholesterol/lipid interactions. However, binary lipid mixtures without cholesterol are also included in this work. The theoretical understanding of binary lipid mixtures is well established and this thesis wants to clarify theoretical models with experimental evidence.
Within the framework of this thesis different experimental techniques used to investigate the lipid phase behavior of lipid model membranes composed of synthetic lipids and lipid extracts from natural tissue are presented and applied. Thereby the thesis tries to stay in close contact with theoretical models. In this context, thermodynamic models are important tools to understand systems consisting of thousands of molecules.

After a short introduction to the underlying theory and the materials and methods applied within this thesis (chapter 2 and 3, respectively), chapter 4 and 5 concentrate on the experimental results of the lateral structure of lipid membranes containing ceramides and cerebrosides, respectively. Ceramides and cerebrosides both belong to the class of sphingolipids and can be converted into each other by enzyme activity. In chapter 6 a new data analysis for FTIR data, namely the difference spectra method, is introduced for the investigation of lipid phase transitions and applied to binary lipid mixtures. The results are compared with Monte Carlo simulations that are known to describe lipid phase behavior very well. Chapter 7 investigates pore formation events in the melting transition regime of lipid model membranes. In chapter 8 a new method to calculate the domain fraction of gel and fluid phases on Giant Unilamellar Vesicles displaying phase coexistence is presented. The results are compared with predictions from the ideal solution theory described in chapter 2.

Chapter 2

Theory

2.1 Phases and phase diagrams

2.1.1 Gibbs' phase rule

A conglomerate of molecules of different state of aggregation can display different homogeneous regions that are separated by interfaces. These homogeneous regions are called phases. Different phases display different properties, such as density and compressibility for example. Two phases are in equilibrium when their temperatures T_i, pressures p_i and chemical potentials μ_i are in equillibrium.

$$\begin{aligned} T_1 &= T_2 \\ p_1 &= p_2 \\ \mu_1(T_1, p_1) &= \mu 2(T_2, p_2). \end{aligned} \tag{2.1}$$

For a closed system with C components and P phases the following equilibrium conditions hold:

$$\begin{aligned} T_1 &= T_2 = ... = T_P \\ p_1 &= p_2 = ... = p_P \\ \mu_{1,1} &= \mu_{1,2} = 3.... = \mu_{1,P} \\ \mu_{2,1} &= \mu_{2,2} = 4.... = \mu_{2,P} \\ &... \\ \mu_{C,1} &= \mu_{C,1} = 5.... = \mu C, P \end{aligned} \tag{2.2}$$

where $\mu_{i,j}$ denominates the chemical potential of component i in phase j. These are $(P-1)(C+2)$ equations as conditions for chemical equilibrium. In order to be solvable, this system must hold the condition

$$F = C + 2 - P \geq 0. \tag{2.3}$$

F is the number of degrees of freedom of the system, that means the number of variables that can be changed independently without changing the phase composition P. For $F = 0$ all variables are defined explicitly. The equation

$$F = C + 2 - P \tag{2.4}$$

is called Gibbs' phase rule. In the case of the experiments conducted for this thesis pressure was held constant and only temperature was altered. In this case Gibbs' phase rule reduces to

$$F = C + 1 - P. \tag{2.5}$$

2.1.2 Ideal solution theory

The ideal solution theory is a thermodynamical approach to calculate phase diagrams of binary lipid mixtures [52]. Phase diagrams are a good way of mapping the phase behavior of compounds, in order to reveal under which conditions which phases coexist (see figure 2.1). The ideal solution theory considers different lipid species that interact as if they were molecules of the same lipid species. If an interaction parameter $\omega_{L1,L2}$ is introduced, describing the interaction between lipid species L1 and lipid species L2, lipids interacting ideal will have $\omega_{L1,L2} = \omega_{L1,L1} = \omega_{L2,L2}$. Lipid species interacting ideal will show complete miscibility in the gel phase. We consider x_A^S and x_A^L, the fractions of lipids of component A in liquid (L) and solid (S) phase, respectively and also x_B^S and x_B^L, the corresponding fractions of lipid species B. If both phases are in equilibrium at a temperature T, the potentials of gel and fluid phase are equal:

$$\begin{aligned} \mu_A^S &= \mu_A^L \\ \mu_B^S &= \mu_B^L \end{aligned} \tag{2.6}$$

The chemical potential of lipid species A in an ideal mixture is given as follows:

$$\begin{aligned} \mu_A^S &= \mu_A^{S,0} + RT \ln x_A^S \\ \mu_A^L &= \mu_A^{L,0} + RT \ln x_A^L \end{aligned} \tag{2.7}$$

with the Gibbs' free energies $\mu_A^{S,0}$ and $\mu_A^{L,0}$ of a mole of pure lipid A in the liquid or in the solid phase at temperature T. R is the gas constant. The same is valid for lipid species B. Some calculations lead to the fractions of both lipid species in solid and fluid phase [52]:

$$\begin{aligned} x_A^L &= \frac{e^{-A}(e^{-B}-1)}{e^{-B}-e^{-A}} \\ x_A^S &= \frac{e^{-B}-1}{e^{-B}-e^{-A}}, \\ x_B^L &= \frac{e^{-B}(e^{-A}-1)}{e^{-A}-e^{-B}} \\ x_B^S &= \frac{e^{-A}-1}{e^{-A}-e^{-B}}. \end{aligned} \tag{2.8}$$

with the terms

$$\begin{aligned} A &= -\frac{(\Delta H_A)_{T_A}}{R}\left(\frac{1}{T}-\frac{1}{T_A}\right) \\ B &= -\frac{(\Delta H_B)_{T_B}}{R}\left(\frac{1}{T}-\frac{1}{T_B}\right). \end{aligned} \tag{2.9}$$

ΔH_A and ΔH_B are the melting enthalpies of pure lipid species A and B, respectively. T_A and T_B are the corresponding melting transition midpoints. The equations 2.8 can be used to calculate theoretical phase diagrams. They are valid within the phase coexistence regime.

The lever rule can be used to calculate the relative proportion of liquid and solid phase of an ideal lipid mixture of an experimentally derived phase diagram [52](see figure 2.1):

$$x_S = \frac{x_s}{x_s + x_l} \tag{2.10}$$

$$x_L = 1 - x_S = \frac{x_l}{x_s + x_l} \tag{2.11}$$

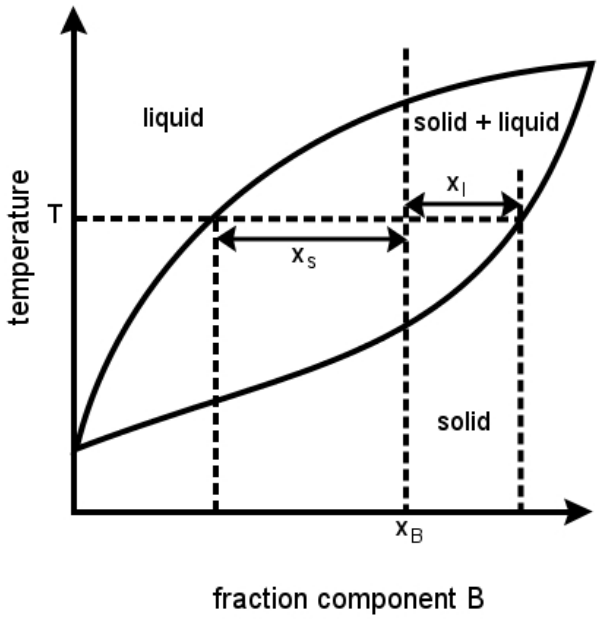

Figure 2.1
Sketch of a phase diagram to clarify the lever rule (equations 2.10 and 2.11).

x_S and x_L are the proportions of gel and fluid phase, respectively. x_s and x_l are defined the following way (see figure 2.1): If a vertical line is drawn at the selected lipid mixing ratio, x_s represents the distance from this vertical line to the liquidus point of the corresponding temperature. x_l is found the same way but looking for the solidus point on the solidus line at

the corresponding temperature. If a phase diagram is known, from calorimetry for example, the solid ordered and liquid ordered phase fractions can be calculated by measuring x_s and x_l and dividing each of them by the sum of both. The distances can be measured with an ordinary ruler for example.

2.1.3 Regular solution theory

The preceding section dealt with the theory of phase diagrams of binary lipid mixtures with ideally interacting lipid species. However, this will only be the case if both lipid species are virtually the same. The non-ideal behavior of real mixtures leads to an incomplete miscibility in some proportions of the lipids in the solid state.
Following Lee [52], the chemical potential of a regular lipid solution has to be rewritten as

$$\mu_A = \mu_A^0 + RT \ln(x_A j_A), \tag{2.12}$$

where the activity coefficient j_A describes the non-ideality of the lipid mixture.
The excess chemical potential can be defined as

$$\mu_A^e = RT \ln j_A, \tag{2.13}$$

that originates from the non-ideality of the lipid mixture. Similarly, the mixture has an excess free energy of

$$G^e = x_A \mu_A^e + x_B \mu_B^e \tag{2.14}$$

One possibility to find manageable expressions for these excess quantities is to assume that the entropy of the mixture approaches ideal behavior, but that the enthalpy of mixing is no longer zero, but is given by

$$\Delta H_M = \rho_0 x_A x_B \tag{2.15}$$

where ρ_0 is an interaction parameter relating to the difference in energy of like and unlike lipid species pair interactions:

$$\rho_0 = Z(2U_{AB} - U_{AA} - U_{BB}). \tag{2.16}$$

Z is the coordination number and U_{xx} is the molar energy of a lipid pair interaction with $x \in \{A, B\}$. It follows that

$$\mu_A^e = \rho_0 x_A^2 \mu_B^e = \rho_0 x_B^2 \tag{2.17}$$

If both solid and liquid phases are regular solutions, the chemical potentials in the solid phase are given by

$$\begin{aligned} \mu_A^S &= \mu_A^{S,0} + RT \ln x_A^S + \rho_0^S (1 - x_A^S)^2 \\ \mu_B^S &= \mu_B^{S,0} + RT \ln(1 - x_A^S) + \rho_0 (x_A^S)^2, \end{aligned} \tag{2.18}$$

and similarly for the liquid phase:

$$\begin{aligned} \mu_A^L &= \mu_A^{L,0} + RT \ln x_A^L + \rho_0^L (1 - x_A^L)^2 \\ \mu_B^L &= \mu_B^{L,0} + RT \ln(1 - x_A^L) + \rho_0 (x_A^L)^2. \end{aligned} \tag{2.19}$$

The condition for liquid and solid phase to be in equilibrium is $\mu_A^L = \mu_A^S$ and $\mu_B^L = \mu_B^S$ and therefore

$$\ln \frac{x_A^L}{x_A^S} + \frac{\rho_0^L(1-x_A^L)^2 - \rho_0^S(1-x_A^S)^2}{RT} = -\frac{\mu_A^{L,0} + \mu_A^{S,0}}{RT} \tag{2.20}$$

This leads to

$$\ln \frac{x_A^L}{x_A^S} + \frac{\rho_0^L(1-x_A^L)^2 - \rho_0^S(1-x_A^S)^2}{RT} = -\frac{(\Delta H_A)_{T_A}}{R}\left(\frac{1}{T} - \frac{1}{T_A}\right) \tag{2.21}$$

$$\ln \frac{1-x_A^L}{1-x_A^S} + \frac{\rho_0^L(x_A^L)^2 - \rho_0^S(x_A^S)^2}{RT} = -\frac{(\Delta H_B)_{T_B}}{R}\left(\frac{1}{T} - \frac{1}{T_B}\right) \tag{2.22}$$

ΔH_A and ΔH_B are the melting enthalpies of pure lipid species A and B, respectively. T_A and T_B are the corresponding melting transition midpoints. These equations are of transcendent nature and therefore can only be solved numerically. There are several issues that make these calculations inaccurate, namely the assumption that the entropy of the solution approaches ideal behavior and that the enthalpy of mixing can be described by equation 2.15. Additionally, it does not take into account interaction energies for lipids of different states.
In order to get a more precise picture of the phase behavior, Monte Carlo Simulations were introduced. These Simulations include cooperativity parameters for lipids of different states and describe the phase behavior of lipid membranes well (see section 2.2).

2.1.4 Ternary phase diagrams

Concerning lipid mixtures, the description of binary phase diagrams is widely advanced already, but the description of ternary phase diagrams for binary lipid mixtures and cholesterol is still at the beginning. Recently, Feigenson summed up experimental results from the past years and drew the conclusion that the data obtained up to now fits two different ternary phase diagrams [53](see figure 2.2).
The important fact for the Type I phase diagram is that no regions of liquid disordered domain separation are observed by means of optical microscopy. At low cholesterol concentrations (up to 0.16 mole fractions) macroscopic liquid disordered / solid ordered phase coexistence is observed [13]. Above 0.16 mol % cholesterol, the domain pattern vanishes abruptly. However, FRET experiments indicate that with a cholesterol fraction of up to 0.25 phase separation occurs [54].
The Type II phase diagram (see figure 2.2) shows at least three regions with two-phase coexistence and one region with three-phase coexistence [13]. In the lipid mixtures corresponding to the Type II phase diagram, cholesterol shows higher preference for the gel phase rather than the fluid phase. This is not the case for the Type I phase diagram, where cholesterol has essentially the same solubility in gel and fluid phases.
At very high cholesterol concentration, both phase diagrams show coexistence of cholesterol monohydrate and liquid ordered phase. The weakness of both phase diagrams presented might be that they are drawn from observations with fluorescence microscopy. Several techniques show that domains smaller in size than the resolution of optical microscopes can exist [35, 54, 55].
Mean field theory approaches to simulate ternary lipid mixtures with cholesterol exist, and these are in agreement with experimental results [56]. These calculations verify that addition of cholesterol disorders the gel phase and that the chain order in the liquid ordered phase is

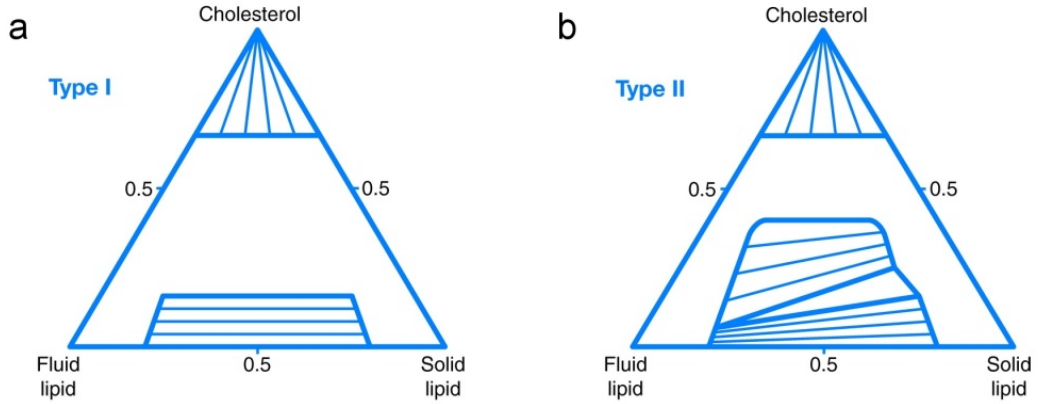

Figure 2.2
Two ternary phase diagrams that seem to be sufficient to map the phase behavior observed for three component mixtures up to date. (*a*) The Type I phase diagram: No macroscopic liquid disordered phase separation is observed with optical microscopy but with other techniques. (*b*) The Type II phase diagram: At least three regions of two-phase coexistence and one phase of three-phase coexistence are observed on the macroscopic scale. *Figure taken from [53].*

higher than in the liquid disordered phase. These mean field theory approaches have also been used to calculate ternary lipid mixtures without cholesterol [57].

2.2 Monte Carlo Simulations

2.2.1 Introduction

The regular solution theory suffers from several disadvantages that can be overcome with other approaches. A lattice model based on statistical mechanics was introduced by Doniach in 1978 [58], only considering two possible states of the lipids, namely one excited state and one ordered all-trans state. This model estimated the melting points of saturated lipids and permeability properties accurately.
Pink et al. [59] introduced another lattice model, the so called *Pink Model*, where each lipid can be in one of ten states, one all-trans, one molten and eight intermediate states. The model was successfully applied to describe experimental Raman scattering experiments on DPPC membranes.
Sperotto and Mouritsen applied the Pink model to proteins incorporated into lipid bilayers by introducing lipid-protein interaction constants, such as hydrophobic thickness and hydrophobic matching between the lipid and protein hydrophobic thicknesses, in accordance with the mattress model [60].
This model was then applied to binary lipid mixtures and successfully described the lipid phase diagram of binary mixtures of saturated phosphocholines and also gave information about the local structure within the membrane plane [61, 62]. However, for the description of the melting of one and two species lipid membranes a two state Ising model for the lipid melting is sufficient [63–65]. This two state model can also be used to describe the influence of proteins on the lipid melting transition [12, 66].

An advantage of Monte Carlo Simulations is that besides the information on the location of the phase diagram boundaries, additional information about heat capacity, enthalpy, lipid/protein clustering, permeability and diffusion can be obtained [64–68].
For the simulations conducted to obtain the results presented within this thesis, the model of Sugar et al. [65] was adopted and applied to a DMPC/DSPC binary lipid mixtures with a deuterated DMPC species used[1]. Information with regard to the melting of the single lipids could be obtained from the simulations and were compared to Fourier Transform Infra Red (FTIR) spectroscopy experiments in chapter 6. The following description of the Monte Carlo simulation theory can already be found in H. Seeger's PhD Thesis [68], as he performed the simulations. It is presented here for the sake of clarity and integrity.

2.2.2 Monte Carlo simulations of a binary lipid mixture

Monte Carlo simulations were applied to a dDMPC-d54/DSPC[2] system based on the two state Ising Model. The lipid chains are arranged on a hexagonal lattice with n lattice sites. Only two states are allowed for the lipids, namely one ordered (o) and one disordered (d) state. The coordination number z of the lipids equals 6.
Each lattice site contains one lipid chain and both lipid chains are allowed to be in opposite state. The lattice is provided with periodic boundary conditions. Due to these boundary conditions the lipid matrix resembles a torus. A toroid structure would imply curvature effects [69], however, curvature is not implemented in the model.
The enthalpies and entropies of the ordered and disordered chains depend on the lipid species and are assigned the symbols ΔH_i and ΔS_i in the following. $i = \{1,2\} = \{\text{dDMPC-d54,DSPC}\}$ stands for the two lipid species. There are two relations that are needed for an algebraic transformation of the systems Hamiltonian. The first is a relation between the total number of lipid chains and the number of pairs of nearest neighbor chains. Another relation is between the number of chains of certain state and species and the number of given pairs of nearest neighbor chains:

$$\frac{z}{2}N = N_{11}^{oo} + N_{11}^{od} + N_{11}^{dd} + N_{12}^{oo} + N_{12}^{od} + N_{12}^{do} + N_{12}^{dd} + N_{22}^{oo} + N_{22}^{od} + N_{22}^{dd} \tag{2.23}$$

$$zN_i^m = 2 \cdot N_{ii}^{mm} + N_{ii}^{mn} + N_{ij}^{mm} + N_{ij}^{mn} \tag{2.24}$$

where $(i \neq j)$ and $(m \neq n)$. N is the total number of lipids, N_i^m is the number of chains of species $i = 1,2$ in state $m = o, d$ and N_{ij}^{mn} is the total number of nearest neighbors of species i and j in states m and n.
For a certain lipid matrix configuration $\mathbf{S}$ the energy $E(\mathbf{S})$ and the degeneracy $f(\mathbf{S})$ is given by:

$$E(\mathbf{S}) = \sum_{i=1}^{2}\sum_{m=o}^{d} E_i^m N_i^m + \sum_{m=o}^{d}\sum_{n=o}^{d}\sum_{i=1}^{2}\sum_{j=1}^{2} E_{ij}^{mn} N_{ij}^{mn} \tag{2.25}$$

$$f(\mathbf{S}) = \prod_{i=1}^{2}\prod_{m=o}^{d} (f_i^m)^{N_i^m} \cdot \prod_{m=o}^{d}\prod_{n=o}^{d}\prod_{i=1}^{2}\prod_{j=1}^{2} (f_{ij}^{mn})^{N_{ij}^{mn}}. \tag{2.26}$$

[1] The simulations were performed by H. Seeger.
[2] dDMPC-d54 is a DMPC lipid where all hydrogen atoms of the lipid chains are replaced by deuterium atoms. dDMPC-d54 has a chainlength of 14 carbon atoms and DSPC has a chainlength of 18 carbon atoms.

E_i^m is the energy of a lipid of species i in state m and the degeneracy due to different localizations and orientations of the rotational isomers in the lipid chain is represented by f_i^m. The van der Waals interactions between the lipid chains are short range interactions, so that only the nearest neighbor interaction energies E_{ij}^{mn} with degeneracies f_{ij}^{mn} are considered.
The probability of finding a certain configuration $\mathbf{S}$ is given by:

$$p(\mathbf{S}) = \frac{e^{-\frac{\chi(S)}{k_B T}}}{Q(N_1, N_2, T, V)}, \tag{2.27}$$

with $\chi(\mathbf{S}) = E(\mathbf{S}) - k_B T \cdot \ln f(\mathbf{S})$, k_B the Boltzmann constant, T the temperature and $Q(N_1, N_2, T, V)$ the partition function.
Together with the equations 2.23, 2.24, 2.26 and 2.26 $\chi(\mathbf{S})$ can be rewritten as a sum of a configuration dependent and a configuration independent part:

$$\chi(\mathbf{S}) = chi_{const}(\mathbf{S}) + chi_{conf.}(\mathbf{S}) \tag{2.28}$$

with

$$\begin{aligned} \chi_{const}(\mathbf{S}) &= N_1 \left\{ (E_1^o - kT \cdot \ln f_1^o) + \frac{z}{2}(E_{11}^{oo} - kT \cdot \ln f_{11}^{oo}) \right\} \\ &+ N_2 \left\{ (E_2^o - kT \cdot \ln f_2^o) + \frac{z}{2}(E_{22}^{oo} - kT \cdot \ln f_{22}^{oo}) \right\} \end{aligned} \tag{2.29}$$

and

$$\begin{aligned} \chi_{conf.}(\mathbf{S}) &= N_1^d(\Delta H_1 - T\Delta S_1) + N_2^d(\Delta H_2 - \Delta S_2) \\ &+ N_{11}^{od}\omega_{11}^{od} + N_{12}^{oo}\omega_{12}^{oo} + N_{12}^{od}\omega_{12}^{od} \\ &+ N_{12}^{dd}\omega_{12}^{dd} + N_{12}^{do}\omega_{12}^{do} + N_{22}^{od}\omega_{22}^{od}, \end{aligned} \tag{2.30}$$

with the following definitions:

$$\Delta H_i = \left\{ E_i^d + \frac{z}{2} E_{ii}^{dd} \right\} - \left\{ E_i^o + \frac{z}{2} E_{ii}^{oo} \right\}, \tag{2.31}$$

$$\Delta S_i = k_B \cdot \ln f_i^d - k_B \cdot \ln f_i^o - \frac{z}{2} k_B \cdot \ln \frac{f_{ii}^{oo}}{f_{ii}^{dd}}, \tag{2.32}$$

$$\omega_{ij}^{mn} = \left[E_{ij}^{mn} - \frac{E_{ii}^{mm} + E_{jj}^{nn}}{2} \right] - k_B T \cdot \ln \frac{f_{ij}^{mn}}{\sqrt{f_{ii}^{mm} f_{jj}^{nn}}} \tag{2.33}$$

During the simulation only the free energy difference between the two configurations is needed and therefore the configuration independent part can be neglected.
This means that in the case of a binary lipid mixture only ten parameters have to be determined. These are the enthalpy and entropy change during the melting transition of both single lipid components and a total of six interaction parameters. All interaction parameters can be deduced from heat capacity profiles that can be obtained with Differential Scanning Calorimetry.
The change in enthalpy during the lipid melting transition for the single lipid species is calculated by integration of the heat capacity. The Gibbs free energy $\Delta G_i(T_{m,i}) = \Delta H_i - T_{m,i}\Delta S_i$ equals zero at the melting transition midpoint, as the chemical potential of both phases are equal.

The melting transition temperature is also obtained from the heat capacity profile and is used to calculate the change in entropy during the melting transition

$$\Delta S_i = \frac{\Delta H_i}{T_{m,i}}. \tag{2.34}$$

The six interaction parameters are deduced by comparing heat capacity profiles simulated to the heat capacity profiles measured and changing the parameters until the profiles overlap. Usually the interaction parameters are found by comparing many different heat capacity profiles for different mixing ratios, including the single lipid species and if a set of interaction parameters is found the parameters are constant throughout the whole composition range of the lipid mixture.

Monte Carlo simulations perform a random walk through the phase space of the lattice model described above. Each phase state is accepted with a certain probability. In each step of a Monte Carlo simulation the chains of a randomly picked lipid are allowed to change state and the lipid is allowed to diffuse. Diffusion is the exchange of the position with a neighboring lipid. One Monte Carlo Simulation step is performed in the following way:

- The simulation starts from the actual configuration $\chi(\mathbf{S}_2)$ and a new configuration $\chi(\mathbf{S}_1)$ is generated by performing one of the possible Monte Carlo steps: (i) A change of state of a lipid chain from ordered to disordered or the other way round. (ii) the lipid is allowed to make a diffusion step. (iii) Four lipid chains perform a rotation. After this the energy of the new configuration is calculated.

- The energy difference between the old configuration and the new configuration is calculated and used to calculate a Boltzmann factor K that gives a probability P

$$\Delta G = \chi_{conf}(\mathbf{S}_2) - \chi_{conf}(\mathbf{S}_1) \tag{2.35}$$

$$K = e^{-\frac{\Delta G}{RT}} \tag{2.36}$$

$$P = \frac{K}{K+1}. \tag{2.37}$$

  R is the gas constant and T the temperature.

- A random number RAN is generated with $RAN \in \}0,1\{$ and if $RAN \leq P$ the new configuration is accepted or rejected if $RAN > P$.

This algorithm is the so called Glauber algorithm [70].
With this algorithm and the possible Monte Carlo steps (i) to (iii) a Monte Carlo cycle is defined the following way:

- In the first N steps a lipid chain is picked randomly and depending on the result of the Glauber algorithm its state is changed or not.

- In the next N steps two lipids are chosen which shall perform a diffusion step if the Glauber algorithm accepts the new configuration

- In the last N steps four chains are chosen which might undergo a rotational step.

N is the number of lattice points.

From the Monte Carlo simulations the heat capacity can be derived from the fluctuations in enthalpy H:

$$\Delta c_p = \frac{\overline{H^2} - \overline{H}^2}{NRT^2}. \tag{2.38}$$

This is the so called *fluctuation dissipation theorem* which can be derived from statistical physics relations [71] or from linear response theory [72]. In the left panel of figure 2.3 the enthalpy fluctuations of a DMPC/DSPC equimolar mixture at different temperatures are plotted. The fluctuations are stronger at a temperature within the phase coexistence regime (upper trace in the left panel of figure 2.3). In the right panel the simulated heat capacity profile of a DMPC/DSPC 50:50 mixture is compared to the corresponding heat capacity profile measured with DSC. Both match well.

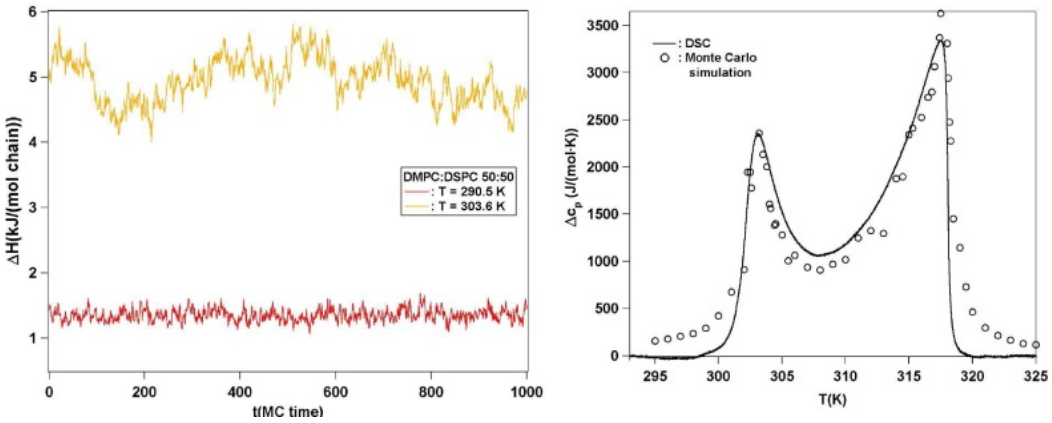

Figure 2.3
The heat capacity can be calculated from the enthalpy fluctuations in Monte Carlo simulations. (*left*) The fluctuations are stronger at a temperature where the membrane is in the phase transition regime (compare right figure to left figure). The enthalpy traces are simulations of a DMPC/DSPC 50:50 mixture. (*right*) The heat capacity profile of a DMPC/DSPC 50:50 mixture calculated from Monte Carlo simulations fits the experimental heat capacity profile well. *Figure taken from [68]*

2.3 Fluctuations

From figure 2.3 in the preceding section it can be seen that the fluctuations in enthalpy are higher, the higher the corresponding heat capacity value is. By switching off the diffusion steps during a Monte Carlo simulation, local fluctuations can also be mapped by defining the local fluctuations of a lipid chain $f(i,j)$ as:

$$f(i,j) = \langle S(i,j,t)^2 \rangle - \langle S(i,j,t) \rangle^2. \tag{2.39}$$

$S(i,j,t)$ can adopt the values $S(i,j,t) = 1$ for an unordered lipid chain and $S(i,j,t) = 0$ for an ordered chain. With this approach Seeger [68] mapped the local fluctuations of an equimolar mixture of DMPC/DSPC. It can be seen from figure 2.4 that the fluctuations are strongest

when the temperature belongs to a high heat capacity value (compare the heat capacity profile in figure 2.3 to the fluctuations in figure 2.4)[3].

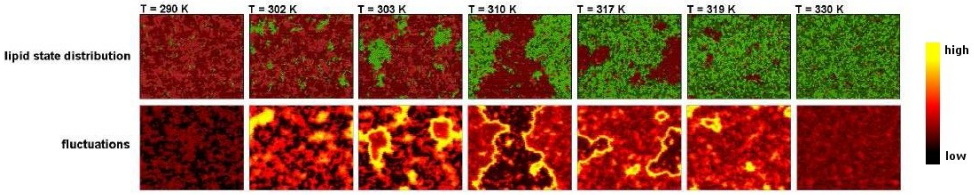

Figure 2.4
Lipid state distribution and local fluctuations of a DMPC/DSPC 50:50 membrane at different temperatures. (*upper row*) domain formation in the membrane. Red areas correspond to solid lipids, green areas correspond to disordered lipids. (*lower row*) Local fluctuations. Dark areas correspond to low fluctuations, light areas to high fluctuations. *figure taken from [68].*

In the region between the two peaks of the heat capacity profile (at 310K) large domains form in the membrane plane and the fluctuations are highest at the phase boundaries. A comparison of the fluctuations in fluid and gel phase domains indicates that higher fluctuations occur in the fluid phase. At temperatures where the peaks of the heat capacity profile are located the whole membrane shows strong fluctuations (302K and 319K, respectively) and the interfacial regions are difficult to separate.
Cruzeiro-Hansson and Mouritsen [73] reported that the interfacial area is highest in the melting transition and by assigning a high permeation rate to the domain interfaces they were able to simulate the permeability of DPPC vesicles to Na^+ ions. Papahadjopoulos et al. reported that the ion permeability of DPPC membranes is highest in the melting transition [9](see figure 2.5).

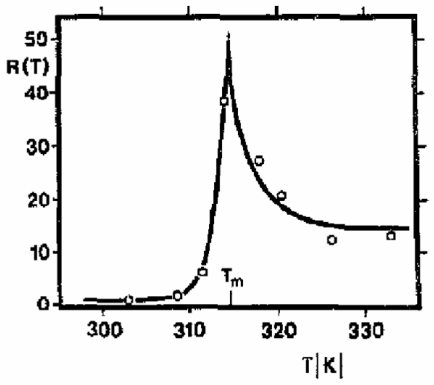

Figure 2.5
Comparison between Na^+ efflux experiments [9] and MC simulations of the permeability of DPPC vesicles with varying temperature [73]. The permeability is highest at the phase transition temperature T_m. *Figure taken from [73].*

[3] At this point one has to be careful. Enthalpy and entropy are calculated from macroscopic fluctuations, not from local fluctuations. However, if the heat capacity is increased, strong local fluctuations will occur and the screenshots of the Monte Carlo simulations can indicate their distribution.

As shown in the preceding chapter, not only the local fluctuations are high at high heat capacity values, but also the global fluctuations are highest [74], as can be seen from the fluctuations in enthalpy. It can be shown experimentally that the fluctuations in volume and area and therewith the area and volume compressibilities κ_T^{vol} and κ_T^{area} are also highest in the melting transition [11, 75].

$$c_p = \frac{\overline{H^2} - \overline{H}^2}{RT^2} \tag{2.40}$$

$$\kappa_T^{vol} = \frac{\overline{V^2} - \overline{V}^2}{\overline{V} \cdot RT} \tag{2.41}$$

$$\kappa_T^{area} = \frac{\overline{A^2} - \overline{A}^2}{\overline{A} \cdot RT}. \tag{2.42}$$

As a consequence, volume and area compressibilities can be related to the heat capacity [11]

$$\Delta\kappa_T^{vol} = \frac{\gamma_{vol}^2 T}{\overline{V}} \Delta c_p \tag{2.43}$$

$$\Delta\kappa_T^{area} = \frac{\gamma_{area}^2 T}{\overline{A}} \Delta c_p. \tag{2.44}$$

Nagle and Scott [76] showed theoretically, that membranes may exist in a near-critical state and large-scale fluctuations in density occur in the phase transition. They suggested that this might lead to cavity opening. This cavity opening could facilitate the permeation of ions through the hydrophobic core of the membrane. Besides the permeation experiments of Papahadjopoulos et al. [9], Black Lipid Membrane (BLM) experiments of Antonov et al. also show that permeability is highest in the melting transition [77, 78].
As the area and volume fluctuations are proportional to the heat capacity, we propose that also pore formation and therefore the membrane permeability p_M is proportional to the excess heat capacity of lipid bilayers.

$$p_M \propto \Delta c_p \tag{2.45}$$

This proposal will be investigated in chapter 7.

A question that is still not solved is whether hydrophilic or hydrophobic pores occur in the melting transition. Antonov et al. propose hydrophillic pores as they can block the pores with PEGs[4] of a certain size. They also measure the pore size and the pore number. The pore number agrees well with theoretical predictions from Freeman et al. [79]. Interestingly, Antonov et al. mention that the type of pore formed in BLM experiments depends on the experimental conditions. If the pores are formed by *electroporation*, hydrophobic pores are formed. In the case of the *soft perforation* hydrophilic pores are formed [77].
In MD simulations Gurtovenkov and Vattulainen [80] observe the formation of hydrophilic pores but also ion permeation along water defects that span the bilayer.

[4] Polyethylene glycol (PEG) is a polymer with the sum formula $C_{2n}H_{4n+2}O_{n+1}$. Depending on the chainlength it has different sizes.

Chapter 3

Materials and Methods

This chapter describes the experimental sample preparations used. Additionally, the experimental techniques used are briefly explained. The section *Materials* introduces the lipids and dyes used, the section *Sample preparation and experimental parameters* details how the samples were prepared, which instrumentation was used and which particular settings were applied. The section *Methods* provides some background information on the methods applied.

3.1 Materials

The lipids 1,2-Dilauroyl-sn-Glycero-3-Phosphocholine (DLPC), 1,2-Dimyristoyl-sn-Glycero-3-Phosphocholine (DMPC), 1,2-Dipalmitoyl-sn-Glycero-3-Phosphocholine (DPPC), 1,2-Distearoyl-sn-Glycero-3-Phosphocholine (DSPC), 1,2-Dioleoyl-sn-Glycero-3-Phosphocholine (DOPC), 1-Palmitoyl-2-Oleoyl-sn-Glycero-3-Phosphocholine (POPC), porcine brain ceramides ((2S,3R, 4E)-2-acylamino-1,3-octadec-4-enediol), porcine brain galactosyl ceramides (cerebrosides), GalBeta1-3GalNAcBeta1-4(NeuAcAlpha2-3)GalBeta1-4GlcBeta1-1'-Cer (Gangliosides G_{M1}) and cholesterol were purchased at Avantilipids (Alabaster, AL, USA) as powder and used without further purification. The probes 2-(4,4-difluoro-5,7-dimethyl-4-bora-3a, 4a-diaza-s-indacene-3-pentanoyl)-1-hexadecanoyl-sn-glycero-3-phosphocholine (Bodipy), 1,1'-dioctadecyl-3,3,3',3'-tetramethylindocarbocyanine perchlorate (DiI-C_{18}), Fluorescent labeled Cholera Toxin B subunit (CTB) and 6-dodecanoyl-2-dimethyl-aminonaphthalene (Laurdan) were purchased from Invitrogen (Carlsbad, CA, USA).

3.2 Sample preparation and experimental parameters

3.2.1 Giant Unilamellar Vesicles (GUVs) for microscopy

Sample preparation on platinum wires

Lipid stock solutions from lipid powder were prepared in chloroform/methanol 2:1 and then mixed in the desired lipid mixing ratio with a final lipid concentration of 0.2 to 0.3 mg/ml. In the case of experiments with DiI-C_{18} or Bodipy as fluorescent probes, dye stock solution in methanol was added to these stock solutions. The dye concentration in respect to lipid concentration was 0.4% for Bodipy and 0.25% for DiI-C_{18}. Laurdan (0.125mM in dimethyl sul-

foxide (DMSO), 1µl on 500µl vesicle solution) was added to the vesicles after vesicle formation.

To prepare the dried lipid film, 3µl of the lipid stock solution were evaporated on each of the platinum wires of an electroformation setup [81] and the wires were placed in vacuum for several hours to evaporate solvent residues. After that procedure the wires were hydrated in the wells of the electroformation chamber in a 0.2mol/l sucrose buffer. The sucrose buffer was preheated to a temperature above the liquidus point of the corresponding lipid mixture. The hydration was performed for about 30 minutes. After the hydration an alternate current with an amplitude of U=1.3V and a frequency of f=10Hz was applied to the platinum wires. The generated electric field between the two platinum wires drives vesicle formation[1]. After 15 minutes the frequency of the alternating current was decreased to 1Hz, which is reported to facilitate vesicle separation from the platinum wires (personal communication with L.A. Bagatolli). After additional 15 minutes vesicle formation was stopped and the vesicles in sucrose buffer were mixed with an isoosmolar glucose solution into the wells of LabTek™ chambers (NUNC, Rochester, NY, USA). The mixing results in different densities inside and outside the vesicles and because of the higher density inside, the vesicles settle down to the bottom of the LabTek™ chamber, where they can be observed with a microscope.

A disadvantage of this approach is that the vesicles sometimes float around the bottom of the LabTek™ chamber and this leads to a mismatch of the center of the acquisition planes for an image stack (acquisition of a single picture of a stack usually takes about one second with the Zeiss LSM510 Meta and the settings needed for our experiments). A projection of the stack to make a 2D or 3D projection becomes impossible in this case. A solution of this problem is the formation of lipid half spheres on ITOs. This method is explained in the next section.

Sample preparation on ITOs

ITOs are Indium-Tin-Oxide covered glass slides. They are transparent for light and it is possible to apply a current through the covering ITO layer. This makes them well-suited for vesicle formation and observation. By choosing the right amount of lipid for the preparation, it is possible to form immobile lipid half spheres on the ITO that are suitable to handle in terms of making confocal image stacks that can then be processed to 3D pictures of the lipid half spheres. The lipid half spheres are immobile in comparison to vesicles formed on platinum wires (see section above). Depending on whether the lipids were dissolved in a chloroform/methanol 2:1 mixture or trifluoroethanol (TFE) three slightly different preparation methods were applied. These methods differ only in how the lipid film is spread on the ITO (Thin Film Devices, Anaheim, CA, USA). TFE has a lower surface tension than a chloroform/methanol mixture and therefore wets the surface better, easily providing a smooth lipid film. In the case of chloroform, the lipid film does not get homogeneous without special treatment. It is possible to form vesicles but they do not seem to be unilamellar as no phase separation was observed. Therefore the following protocols were applied:

- If the lipids were dissolved in chloroform/methanol 2:1, which was the case for ceramides and cerebrosides containing lipid mixtures, 50µl of a 3mg/ml lipid stock solution were put

[1] There are models on how vesicle formation might take place [82–85], but the mechanism of this vesicle growth is not yet completely understood.

on the conducting side of an ITO rotating in a spin-coater KW-4A (Chemat, Northridge, CA) for 30 seconds at 3000rpm.

- A second method by which a lipid film can be formed from chloroform/methanol was introduced when no TFE was available during a visiting period at the University of Santiago de Chile. A droplet of 10µl stock solution (c=3mg/ml) is placed in the center of the conducting side of an ITO and smeared with a coverslip until the solvent is evaporated.
- If the lipids were dissolved in TFE, which was usually the case for lipid mixtures only consisting of phospholipids with phosphocholine headgroups, 6µl of lipid stock solution were spread on an ITO (Thin Film Devices, Anaheim, CA, USA) and evaporated. The concentration of the lipid stock solutions for forming lipid half spheres on ITOs was 1mg/ml to 2mg/ml in TFE.

Dye/lipid ratio were 0.4% for Bodipy, 0.2% for Dil-C_{18} and 1% for Laurdan. After the lipid film was placed on the ITO using one of the three methods described above, it was placed under vacuum for at least 2 hours to evaporate solvent residues. After the removal of the organic solvent the ITO was assembled into a self built electroformation chamber [81] and hydrated in MilliQ water (17.5MΩ; Millipore, Billerica, MA, USA) for about 30 minutes. The MilliQ water was preheated to a temperature above the liquidus point of the lipid mixture. The hydration step was followed by the application of an alternate current with an amplitude of 1.3V and a frequency of 10Hz. The electroformation was carried out for 15 minutes and after that the vesicles on the ITO could be observed in the electroformation chamber in the microscope.

The microscope filter settings

The fluorescent probes used in the experiments were excited with a Argon laser at 488nm (Bodipy), a 543nm HeNe laser (Dil-C_{18}) and a Til:Sapphire laser at 790nm for Laurdan. The Ti:Sapphire laser is a tunable MaiTai laser from Spectra Physics (Mountain View, CA, USA). Image acquisition was done with a LSM 510 Meta (Zeiss, Jena, Germany). The bandpass filters applied for Laurdan were a bandpass filter 390-465nm for the emission in the blue and a bandpass filter 500-550 for the emission in the green spectral region. Image acquisition was done with a LSM 510 Meta (Zeiss, Jena, Germany).
GP values were calculated using the SimFCS package of the Globals for Images software developed at the Laboratory for Fluorescence dynamics at Irvine University of California.

The beam path of the confocal microscope Zeiss LSM 510 Meta used for the experiments is sketched in figure 3.1 and the setup is described for a DLPC/DPPC 30:70 lipid mixture in the following. The mixture contains the fluorophores Bodipy and Dil-C_{18} to label the fluid phase and the gel phase respectively (Figure 3.7). The absorption maximum of Bodipy is at 503nm and its emission maximum is at 512nm. To excite this dye an argon laser with a wavelength of 488nm was chosen. Dil-C_{18} has its absorption maximum at 549nm, the emission maximum is at 565nm. For excitation of Dil-C_{18} a HeNe laser with a wavelength of 543nm was chosen. The spectra of Bodipy and Dil-C_{18} do not overlap significantly, so that the two data acquisition channels for Bodipy and Dil-C_{18} fluorescence can be scanned simultaneously. The laser light is reflected on the first beam splitter (HFT UV/488/543/633) and is focussed on the sample through a 40x magnification objective (Figure 3.1).
The fluorescence light that has a higher wavelength than the exciting laser light passes the objective and also the first beam splitter that is transparent for light of that wavelength. A

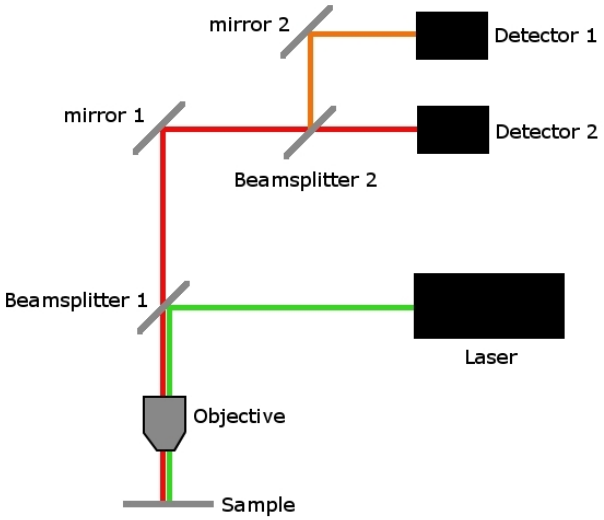

Figure 3.1
Example for a beam path setup of a confocal microscope. The exciting laser light is indicated in green color and the fluorescence light coming from the sample is indicated in red and orange colors respectively.

mirror guides the light onto a second beam splitter (NFT 545) that reflects the fluorescent light of the Bodipy fluorescence and is transparent for the fluorescence light of the Dil-C_{18} probe. The reflected Bodipy fluorescence light is guided by a mirror through a bandpass filter (BP 500-530 IR) to filter laser light and falls onto the detector of channel 1. The Dil-C_{18} fluorescence light that is passing the second beam splitter passes through a longpass filter (LP 560) and reaches the detector on channel 2.

3.2.2 Multilamellar vesicles for calorimetry

In order to prepare multilamellar lipid dispersions in destilled water, lipids from stock solution in chloroform were mixed in the ratio desired and the solvent was evaporated under a stream of nitrogen. Then the samples were placed under vacuum for several hours.
After removal of the organic solvent, the lipids were hydrated with destilled water that was preheated above the liquidus point of the corresponding lipid mixture and kept stirring at this temperature for 30 minutes. The final lipid concentration was 10-20mM. After that the sample was degassed for 15 minutes and one of the following two protocols to proceed were chosen, depending on whether the calorimetric scans should be performed partly below the freezing point of water (i) or above (ii).

i.) The sample was filled into the sample cell of the calorimeter and the reference cell was filled with destilled water.

ii.) The sample was filled into a capillary and centrifuged at 3000rpm for 15 minutes, to settle the vesicles in the lower part of the capillary. The capillary was then put into the sample cell of the calorimeter that was filled with a mixture of ethylene glycol/water 60:40 to

prevent water freezing when scanning below the water freezing point. The reference cell of the calorimeter was filled with the same ethylene glycol/water mixture.

The second protocol has to be used to protect the cell of the calorimeter, because the cell would burst if water freezes inside. The mixture of ethylene glycol/water used lowers the freezing point of water for about 23°C. The capillary is used so as not to contaminate the lipid sample with the ethylene glycol, which would change the lipid melting behavior. It would probably lower the lipid melting transition temperature and decrease the cooperativity of the melting transition and therefore the peak width.
Calorimetric scans were performed at a scan rate of 15 degrees per hour. Data evaluation was done with a procedure for the IGOR software (WaveMetrics, Portland, OR, USA), that was written by T. Heimburg.

3.2.3 Multilamellar vesicles for Fourier Transform Infrared Spectroscopy

The preparation of the multilamellar vesicles for FTIR spectroscopy differed from the preparation of multilamellar vesicles for calorimetry only in so far as that after the 30 minutes of hydration, five freeze thaw cycles were applied. This was done because of the lipid concentration for the FTIR samples was 50mg/ml. At this high lipid concentration the freeze thaw cycles facilitate hydration of the lipids.

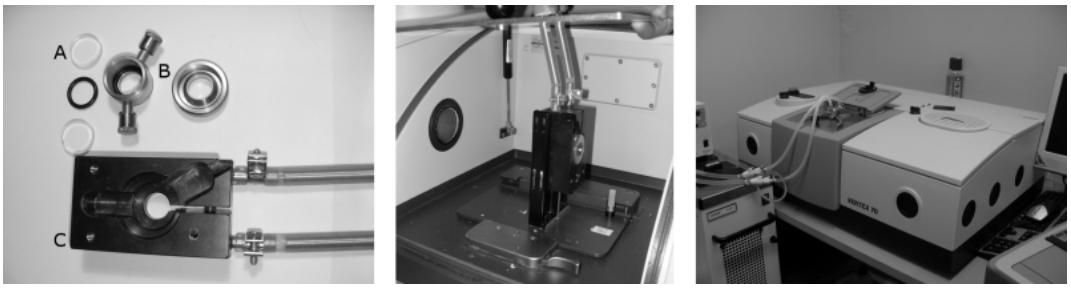

Figure 3.2
Sample preparation and measurement apparatus for the FTIR experiments. (*left*) A CaF_2 window (A) was placed in the sample holder (B). 15µl of the sample solution were placed on the glass and another CaF_2 window was placed on top. After that, the lid of the sample holder was closed and placed in a heatable metal block (C). (*middle*) The metal block was placed in the measurement compartment of the FTIR. (*right*) The FTIR spectrometer used for the experiments. The temperature adjustable metal block was removed from the beampath every second scan by a handle. This was done in order to obtain a proper background signal for the final data processing procedure.

After hydration, the sample was degassed for 15 minutes and 15µl of the lipid solution were put between the two CaF_2 windows (A in figure 3.2) of the sample holder (B in figure 3.2). In the end, the sample holder was placed into a self-built heatable frame (C in figure 3.2) supplied by a water bath (DC30-K20, Thermo Haake, Karlsruhe, Germany) and was placed in the investigation chamber of the FTIR instrument (Vertex70, Bruker, Ettlingen, Germany). In order to eliminate a possible water vapor signal in the spectra, the spectrometer was flushed with nitrogen for 30 minutes before and kept flushed during the measurements.
To perform the experiments, a temperature ramp was driven with a scan rate of 20 degrees

per hour and 30 scans were averaged for each temperature point. After a sample scan, a background scan was taken at each temperature point, in such a way that the sample chamber was lifted out of the spectrometer beam path by a handle manually.

Data acquisition was performed with the OPUS software that comes along with the Vertex70 instrument and data analysis was done with a self-written procedure implemented with the IGOR data analysis software (WaveMetrics, Portland, OR, USA). The procedure is explained in the methods section (section 3.3.8).

3.2.4 Black Lipid Membranes

Black Lipid Membranes were formed following the technique described by Montal and Mueller [86]. A hole was made into a 25µm thick teflon foil (see left panel of figure 3.5) with a spark generator (Electro-Technic Products INC, Chicago, IL, USA). The teflon foil was glued between two teflon blocks with silicon glue and the glue was allowed to dry for about 2 hours (see figure 3.5). This procedure enables the provision of two reservoirs separated by the teflon foil.
To form a bilayer membrane over the hole in the teflon foil, the foil was first prepainted with an alkane in solvent, to facilitate membrane formation (see figure 3.3). Two different mixtures of alkanes in solvent were used, depending on the lipids used:

- The hole in the teflon foil was prepainted with about 1µl of 1-10% hexadecane in Pentane on both sides (DOPC/DPPC experiments).
- The hole in the teflon foil was prepainted with 1µl of 25mg/ml lipid in a mixture of n-decane/$CHCl_3$/MeOH 7:2:1 on one side of the teflon foil [77] (DPPC and DMPC/DSPC experiments).

After the prepainting procedure, the block carrying the teflon foil was placed on a peltier device that was controlled by a Dagan HCC-100A bath temperature controller (Dagan Corporation, Minneapolis, MI, USA) and the temperature was set higher than the melting temperature of the lipid component melting at higher temperature.
After that the lipid film was spread on the buffer surface and depending on the lipid mixture used two different protocols were applied:

- 1µl of lipid in pentane was spread on the buffer surface (DOPC/DPPC mixture).
- 1µl of 25mg/ml lipid in n-decane/$CHCl_3$/ 7:2:1 was spread on the buffer surface (DPPC and DMPC/DSPC membranes).

Lipid membrane formation was verified by application of a triangular voltage signal with an Axopatch 220B patch-clamp amplifier (Molecular Devices, Sunnyvale, CA, USA). Membrane formation could be observed by a capacitive current behavior. If no membrane formed, a short circuit current was measured. The capacitance value also gave information on whether the membrane leaked or the hole in the teflon foil was just blocked by dirt or an air bubble. This is described in section 3.3.9 in detail.
The amplifier was connected to a computer via a Digimess 1440 digitizer and operated with the pCLAMP 10 software (both Molecular Devices, Sunnyvale, CA, USA).

How the membrane forms in detail is not known yet. There are no experimental indications to show whether the membrane forms on one side of the teflon film or if it covers both sides

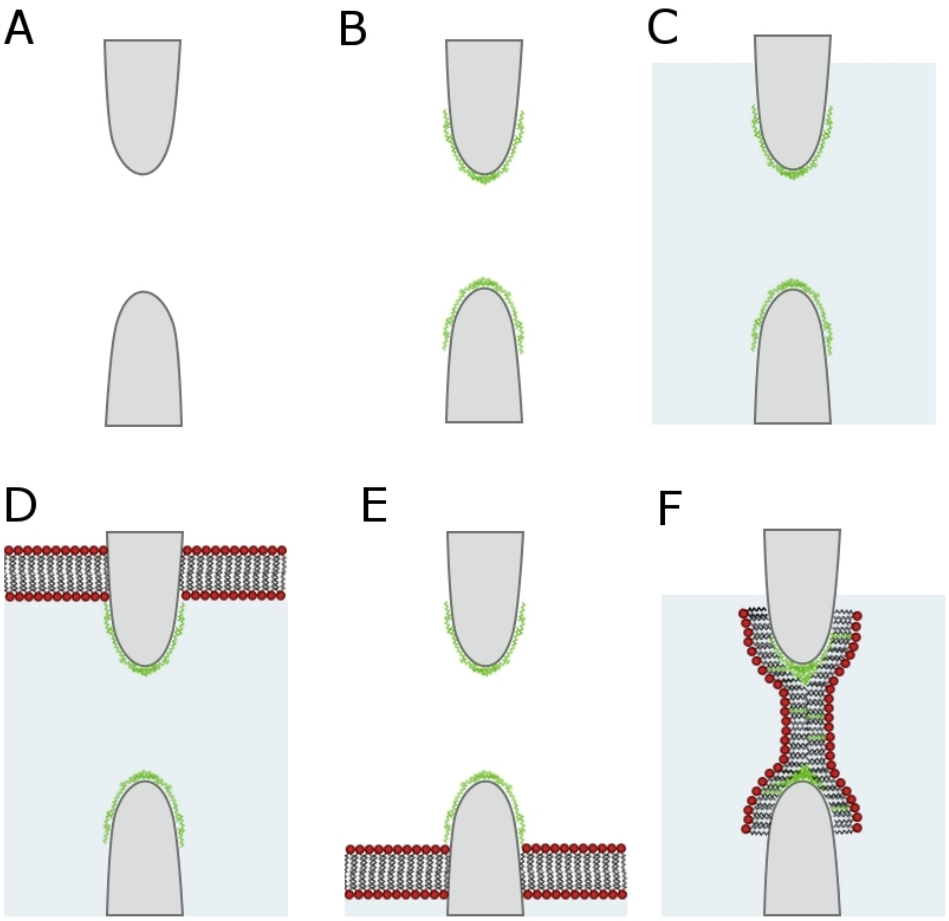

Figure 3.3
The formation of Black Lipid Membranes. (*A*) The opening in the teflon film. (*B*) The teflon film region with the hole is prepainted an alkane in solvent. (hexadecane for example, pictured in green) (*C*) Buffer is filled into the sample compartment. (*D*) A lipid film is spread on the buffer surface. (*E*) The buffer level is lowered below the hole in the teflon film. (*F*) The water level is raised again and the lipid bilayer forms. Alkane fractions might be present in the membrane.

as shown in picture 3.3. It is known that following this procedure a single bilayer forms over the hole. This has been verified by insertion of single OmpF (outer membrane porin F) protein channels. OmpF is a trimer and each monomer acts as channel, so that three distinct current steps could be observed . Protein channel conductance would not occur in a multilayer system (personal discussion with T. Mach). A picture of a bilayer is shown in figure 3.4. A thick annulus consisting of lipid and solvent covers the rim of the aperture. The lipid membrane forms in the central region [87].

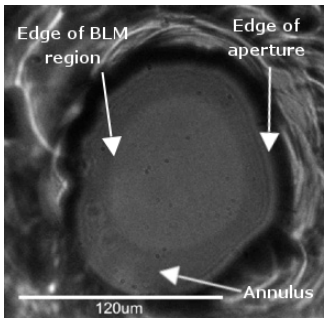

Figure 3.4
A picture of a BLM formed over a glass aperture. On the rim of the aperture a lipid/solvent annulus forms. The lipid bilayer is the bright area in the central region. *Figure taken from [87].*

When performing the experiments, it turned out that both kinds of membrane prepainting did not give different results concerning membrane capacitance, neither did the two different solvents used for spreading the lipid film on the buffer surface. Measurements were performed in the voltage clamp mode with an output gain $\alpha = 2$ and a 10kHz bessel filter applied.

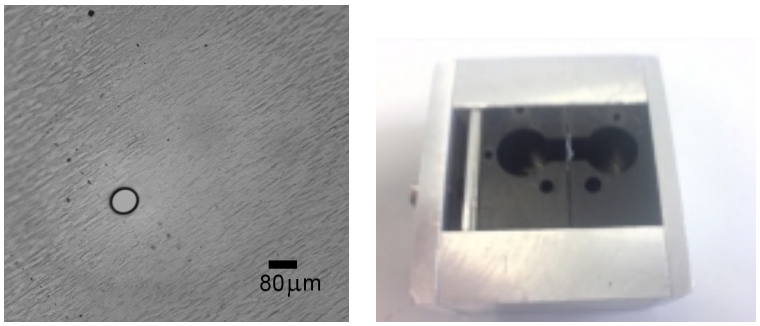

Figure 3.5
(*left*) A hole molten into a teflon film with a spark generator. (*right*) The teflon film separates two compartments in the sample chamber.

3.2.5 Supported bilayers for Atomic Force Microscopy

The supported membranes were formed on freshly cleaved mica (Plano, Wetzlar, Germany) with a size of $8x8mm^2$ with the spin-coating protocol [88]. A 20µl droplet of lipid in hexane/methanol (97:3) was placed onto the mica support that was placed on a spin coater (Chemat KW-4A, Northridge, CA). The mica was spun with 3000rpm for 40 seconds directly afterwards. After overnight storage under vacuum, the sample was hydrated in MilliQ water and annealed to 65°C for one hour to yield a single and highly uniform supported membrane. Excess lipid was removed by washing with fresh MilliQ water that was heated to about 65°C. The effect of washing was monitored continuously. Epi-fluorescence microscopy of the supported membrane was performed with the sample placed in a microscope chamber (LabTek™) on a Nikon TE2000 inverted microscope (Nikon, Badhoevedorp, The Netherlands), using a 403 long working distance (ELWD) objective. Fluorescence excitation was done with a halogen lamp and using a G-2A filtercube (Nikon). Fluorescence images were recorded with a Coolsnap CF

camera (Photometrics, Tucson, AZ). The samples were measured with the atomic force microscope using a PicoSPM (Molecular Imaging, Tempe, AZ). A homemade fluid cell was used and the AFM was operated in magnetic tapping mode (MAC) using MAC levers operated around their resonance frequency of 25 kHz (in water) with a force constant of $k_{MAClever}$=2.8 N/m (nominal). The scan rate used for imaging was in the range of 1.2 – 1.9 Hz for all cases. The free amplitude for tapping mode imaging was in all cases at ∼8.5 V, and the amplitude on scanning was ∼6.5 V.

3.3 Methods

3.3.1 Confocal fluorescence microscopy

The axial resolution of a microscope is given by

$$d_{min} = \frac{\lambda_0}{NA_{obj} + NA_{cond}}, \tag{3.1}$$

where d_{min} is the minimal resolvable distance in a periodic grating, λ_0 is the wavelength of the light used in vacuum and NA_{obj} and NA_{cond} are the numerical apertures of the objective and condenser, respectively. The numerical aperture is given as

$$NA = \eta \cdot sin\alpha. \tag{3.2}$$

η is the refractive index of the immersion medium and α is half of the maximal angle of the light cone of the light coming from the sample and being acceptable by the objective or emerging from the condenser.

Equation 3.1 defines the lateral resolution of a microscope by means of a line grating, but this definition can also be extended to the imaging plane. In this case the objects to resolve are defined as point objects. The image of a point itself is not a point but a circular Airy diffraction pattern and two close objects can only be resolved if their first minima in the Airy pattern are separated by at least

$$r_{Airy} = 0.61\frac{\lambda_0}{NA_{obj}}. \tag{3.3}$$

r_{Airy} is called the Airy-radius.
Of course the airy pattern also extends along the z-axis and therefore an axial resolution along the optical axis can be defined as

$$z_{min} = \frac{2\lambda_0\eta}{(NA_{obj})^2} \tag{3.4}$$

z_{min} is the distance from the center of the 3D diffraction pattern to the first axial minimum. A problem that arises with conventional epifluorescence microscopes, is that the image of the sample shows low contrast for thick samples. This low contrast occurs when the depth of field, that theoretically should be equal to the axial resolution, is bigger than the axial resolution of the microscope. The depth of field δ is defined as

$$\delta = \frac{1}{4}(z_{min^+} - z_{min^-}), \tag{3.5}$$

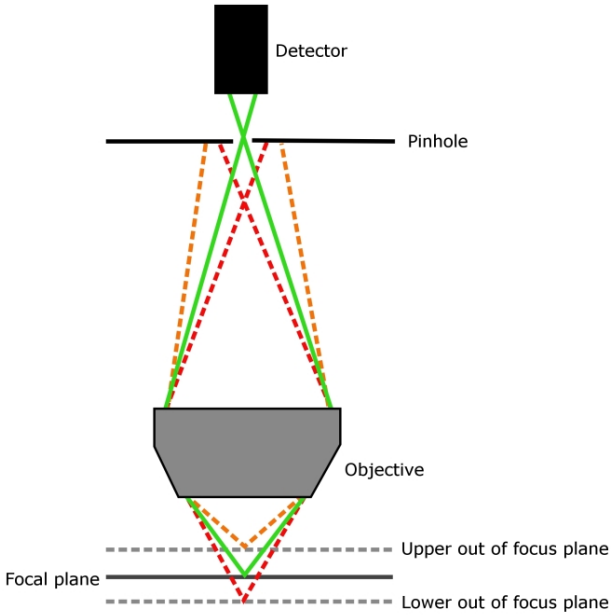

Figure 3.6
Light emerging from planes above or below the focal plane is blocked by the pinhole. This blocking leads to a higher contrast in the axial direction as the blocked light cannot blur the image taken by the detector.

where z^{+}_{min} and z^{-}_{min} are the distances from the central maximum in the 3D diffraction pattern to the first minimum in the 3D Airy pattern along the optical axis. Each illuminated spot in the sample has a cone shaped intensity that reaches above and below the focal plane and each fluorescent object in this region will emit fluorescent light that will reach the detector and blur the image if it is not coming from the focal plane. This means that the apparent depth of field is greater than the axial resolution. To eliminate the blurring effect due to out of focus fluorescence, confocal microscopes are equipped with a pinhole in front of the detector that blocks light coming from planes above and below the focal plane. This increases the contrast of the images and leads to a sectioning effect. The basic concept of a confocal microscope is shown in figure 3.6.

If stacks of confocal pictures with a picture stack spacing of about 1µm in z-direction are chosen, a three dimensional picture of the object of interest can be generated (the left and the middle picture in figure 3.7 show this for a stack spacing of 0.2µm).

3.3.2 3D Deconvolution

The image of a point of the sample does not become a point in the image, but it is a blurred spot because the light from the point had to pass lenses, pinholes and apertures. The way each

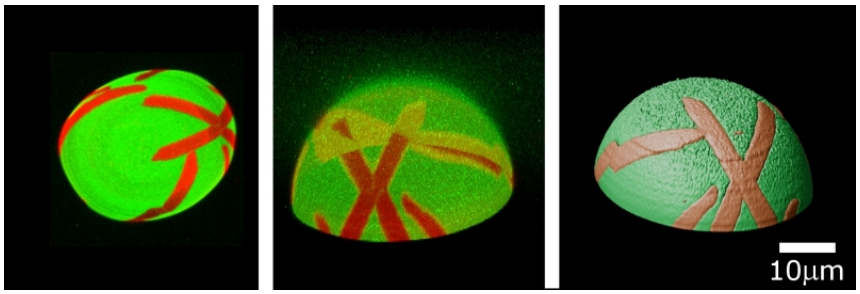

Figure 3.7
(*Left*) A 2D projection of a stack of vesicle pictures. (*Middle*) A projection of the same stack of vesicle pictures along a vector different from the optical axis. The image was done with the Zeiss LSM Image Browser and generates a 3D effect. (*Right*) The vesicle stack was deconvoluted and a 3D picture was constructed with the Huygens software.

image point is converted to a blurred spot is described by the point spread function (PSF), which simply is the image of a single point. The PSF is the mathematical way to describe the degrading effect the optical parts of a microscope have on the image. The image is the sum of all blurred image points, as the imaging process is a linear process.
The mathematical function to describe imaging of a point with the microscope is the convolution — the image is the convolution of the object with the point spread function. The original image can be recalculated if the PSF of the microscope setup is known. It can be calculated if all components in the optical beam path are known, or it can be measured with small beads that are smaller than 30% of the microscope resolution. In order to do a proper deconvolution image, details should be recorded at least at PSF scale, so that all necessary information is collected, because deconvolution works on the PSF scale.

An example of a picture processed with the 3D deconvolution software "Huygens" that is distributed by SVI (Hilversum, Netherlands) is shown in figure 3.7.

To generate deconvoluted 3D objects, stacks of pictures of the object of interest have to be recorded with a microscope. To get enough information for a proper deconvolution, the image acquisition parameters have to be set right. The pixel width settings used for the Zeiss LSM 510 Meta with a 40x water immersion objective was 50-80nm in the imaging plane and 200-300nm in the axial direction. The radius of the pinhole was set to 1 to 1.5 Airy.

3.3.3 Calculating gel/fluid area fractions from GUVs displaying phase coexistence

GUVs consisting of a binary lipid mixture of DLPC/DPPC display macroscopic phase coexistence at room temperature. The domains can be made visible by adding small amounts of fluorescent dyes. In this case Bodipy (1 mol %) and DiI-C_{18} (0.5 mol %) were used to label the fluid phase and the gel phase, respectively.
The images were deconvoluted with the Huygens Professional deconvolution software supplied by SVI (see section above). Image processing routines were implemented into the IDL Data Visualization & Analysis platform by Dr. Steffen Härtel. The routines based on intensity thresholds, morphological filtering and active contours [89, 90] were applied to the confocal image

stacks and resulted in a complete segmentation of gel and fluid areas in the optimal case. However, overlap of gel and fluid areas was observed in many cases and will be discussed in chapter 8. An example of a segmentation is shown in figure 3.8.
An active surface model was adjusted to the 3D reconstruction of the accumulated 2D planes and projected onto the surface of a sphere that was fitted to the data (see figure 3.9). The sphere radius was calculated from the confocal image stacks. For this purpose, 200 spheres were calculated from randomly selected data points of the original data. Mean values or x, y, z and r were calculated from the median-40 values of this set. Median-40 means that the lower 30 and the upper 30 of the 200 randomly selected values for x, y, z and r were not taken into account for the calculation of the mean.

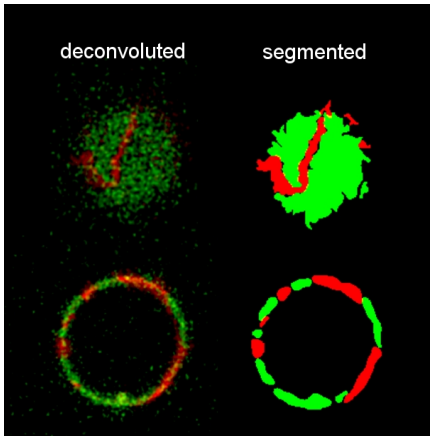

Figure 3.8
Segmentation applied to deconvoluted vesicle images. The image stacks were obtained with confocal microscopy. (*left*) Two deconvoluted images from the top and equatorial region of a vesicle. (*right*) The corresponding images after the segmentation. Gel and fluid domains (red and green, respectively) are well separated.

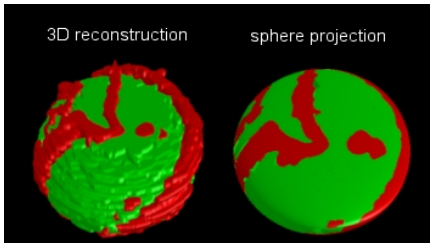

Figure 3.9
3D reconstruction and sphere projection of segmented image stacks. (*left*) A 3D reconstruction of a deconvoluted and segmented vesicle stack. (*right*) The 3D reconstruction is projected to a sphere to calculate the gel/fluid area fractions. The pictures display a DLPC/DPPC 30:70 vesicle. Red areas correspond to gel phase and green areas to fluid phase, respectively.

The domains were approximated by a triangle polygons and the surface calculated from these polygons.

3.3.4 Two Photon Microscopy

Fluorescence occurs when a photon with an energy greater than the energy of the gap between the ground level and the first excited state is absorbed by a fluorophore and raises an electron from the ground state to an excited state 3.10. The electron is usually excited to one of the vibrational modes of the first excited state and by energy loss relaxes to the first vibrational state. After a short time, usually in the nanosecond range, the electron relaxes to the ground state and energy in the form of a photon is released. Because of the energy dissipation through

relaxation within the vibrational modes, the emitted light has slightly less energy, i.e. a longer wavelength compared to the initially absorbed light.

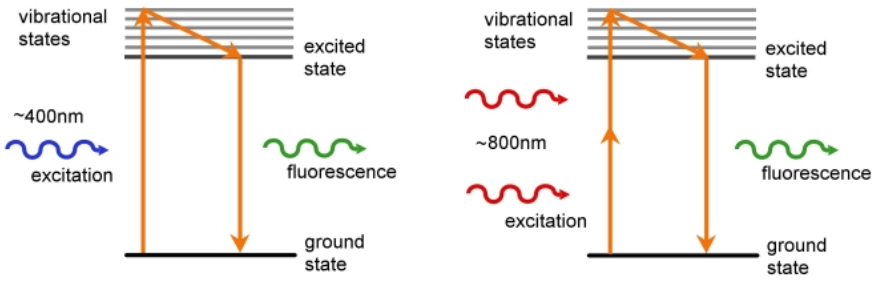

Figure 3.10
(*left*) One photon excitation of a fluorophore. (*right*) Two photon excitation of a fluorophore.

Fluorophores cannot only be excited from the ground state by a single photon, but also by means of two photons. Two photon excitation is a nonlinear process where two photons with half the energy of a photon that would induce one photon excitation are absorbed simultaneously by a fluorophore and excite the dye molecule [91, 92].
To induce two photon excitation a high photon density is needed, which is usually generated by high peak-power lasers and focussing of the laser beam by a high numerical aperture objective. The advantage of pumped lasers to continuous lasers is that the average intensity is lower with pumped lasers, so that damage to the sample is reduced. The intensity has to be high enough to yield the photon density in the focal volume required.
Two photon excitation has some advantages over one photon excitation:

- The photon density needed for two photon excitation is only high enough in the focal spot. As a consequence two photon microscopy has an inherent axial contrast and the confocal effect is achieved without a pinhole to block light coming from above and below the focal plane, as no fluorophores are excited outside the focal spot 3.11.

- The excitation and emission spectra do not overlap, so that the whole bandwidth of emission can be used (figure 3.12).

- Photobleaching is reduced because only the focal spot is illuminated and not the whole axial region, as in laser scanning microscopy or epifluorescence microscopy.

- Light scattering has a strong wavelength dependence ($\sim \lambda^{-4}$). This means that light of longer wavelength is scattered less in tissue so that the light can penetrate deeper into the tissue.

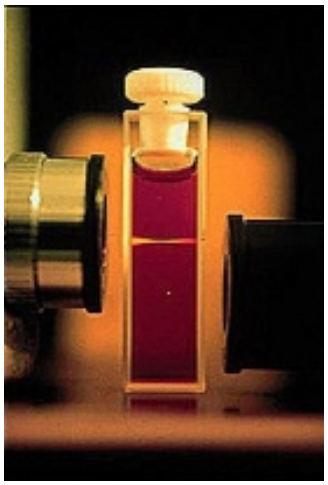

Figure 3.11
Picture showing the excited area of a sample with one (upper light trace) and two photon excitation (lower light dot). In two photon microscopy only fluorophores in the confocal spot get excited. *Picture provided by L.A. Bagatolli.*

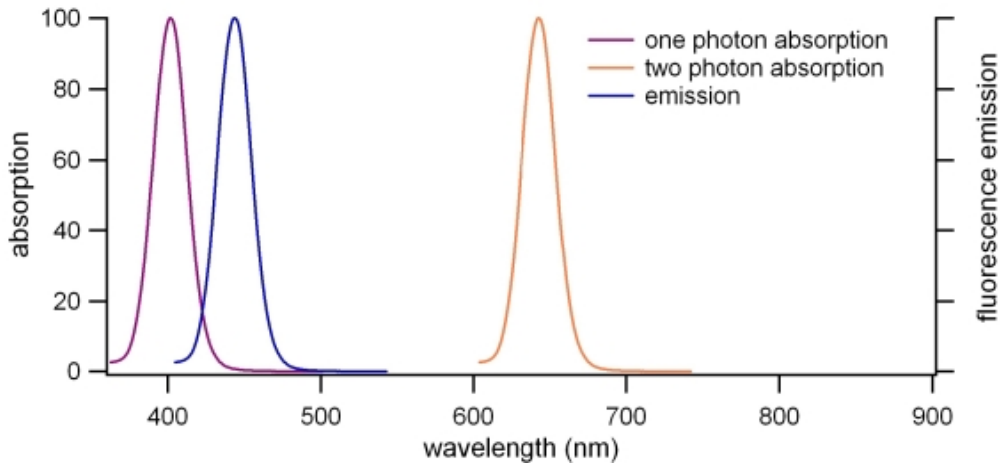

Figure 3.12
Sketch to compare the position of the absorption and emission peaks in one photon and two photon excitation. The absorption spectra for one photon excitation overlaps with the emission spectrum, whereas the absorption and emission spectra for two photon excitation do not overlap.

- For dyes that have their one photon excitation maximum in the UV, special UV optics need to be used. UV optics are quite expensive and are not required if the same fluorescent probe is excited with two photon excitation.

Disadvantages of two photon microscopes are:

- Highly pigmented tissue absorbs infrared light and in this case two photon microscopy is not applicable.
- Two photon lasers are still quite expensive and double the cost in comparison to a one photon confocal microscope.

A comparison of the resolution of a confocal and a two photon microscope depends on whether the excitation wavelength λ_{ex} or the fluorophore is held fixed. If the excitation wavelength

is held fixed, a one photon confocal microscope in the UV has a two times better resolution (∼500nm) than a two photon microscope operated in the IR (∼900nm) [93]. However, the two photon laser scanning microscope resolution can be improved by using a spatial filter in front of the detector. This kind of microscope is called a confocal two photon laser scanning microscope and its resolution is the same as for a one photon microscope [93]. The axial resolution can be further improved to about 100nm if illumination from nearly all directions is used, which is realized in a 4Pi setup [94].

3.3.5 Photoselection effect

The photoselection effect can be used in lipid vesicles to distinguish gel phase and fluid phase domains [92, 95]. In the case of Laurdan it originates from the orientation of the Laurdan transition moment relative to the electric field component of the laser light used for excitation of the Laurdan molecules.
For example, the laser light of the earlier described Ti:Sapphire laser can be made circular polarized and the electric field vector will then oscillate in the imaging plane (see figure 3.13). The transition moment of Laurdan is parallel to the membrane normal, and thus to the chains in the lipid bilayer. In the fluid phase the lipid chains wobble, so that the orientation of the Laurdan transition moment often differs from being parallel to the membrane normal and therefore excitation of the Laurdan probe in the fluid phase will occur. In the gel phase the membrane is very stiff and therefore the Laurdan transition moment alignment is very much restricted to the direction of the membrane normal. That means, that if a gel phase domain is situated at the top or bottom part of a vesicle, the Laurdan probe in this domain cannot be excited and the domain stays dark. If the gel domain is situated in the equatorial region of a vesicle it can always be observed because the circular polarized laser light always has a component that will be parallel to the Laurdan transition moment.

The GUV experiments with POPC/cerebrosides were performed on a Zeiss LSM 510 equipped with a two photon laser. In this case, linear polarized laser light was available only and not circular polarized laser light, as with the two photon microscope used for the GUV experiments with POPC/ceramide mixtures. With linear polarized laser light, if a gel domain is situated in the equatorial region of the vesicle, Laurdan can be excited by the excitation light only if the part of the membrane is parallel to the direction of the electrical field vector of the linear polarized laser light. Laurdan will not be excited if the Laurdan transition moment is perpendicular to the electrical field vector of excitation light. This means that for linear polarized laser light in the equatorial region of a vesicle displaying gel phase, there are regions where Laurdan can be excited and cannot be excited. Because of the photoselection effect, areas to calculate Laurdan GP values have to be selected very carefully in this case (see next section for a description of the GP values).

3.3.6 Laurdan and the Generalized Polarization Function

Laurdan has several unique properties that make it ideal to assign the phase of domains in lipid bilayers [92, 95]. These are

- A shift in the Laurdan emission spectrum from green in the fluid phase to blue in the gel phase
- Laurdan distributes homogeneously in membranes displaying phase coexistence.

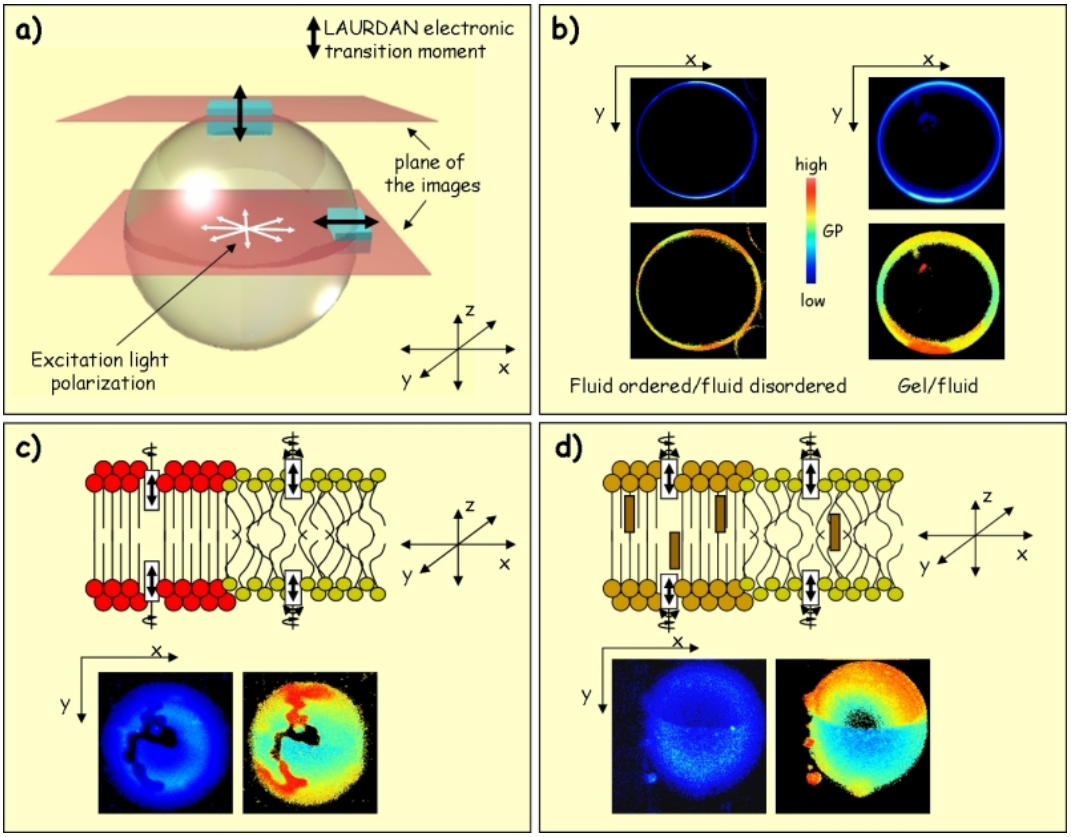

Figure 3.13
The photoselection effect is due to a misalignment of the Laurdan transition moment in respect to the polarized laser light. Gel phases in the top region of a vesicle cannot be observed because in this case the electric field vector of the polarized laser light is perpendicular to the Laurdan transition moment and no excitation of the fluorescent probe occurs. *(a)* Sketch showing the orientation of the Laurdan transition moment alignment in top and equatorial region of a vesicle. The laser light is circular polarized in the imaging plane. *(b)* Fluorescence intensity and GP value images, top and bottom row, respectively. The GP value in the fluid phase is lower than in fluid ordered or solid ordered domains. *(c)* Photoselection effect in the top region of a vesicle. The Laurdan transition moment in the gel phase (red) is restricted because of the firm, condensed gel phase and therefore perpendicular to the electric field vector of the polarized laser light. Therefore no Laurdan excitation occurs. In the fluid phase (green) the chains wobble and therefore the Laurdan transition moment can be excited by the polarized laser light. *(d)* The same as for gel/fluid phase coexistence happens in the case of fluid disordered/solid ordered phase coexistence. The rectangles in the membrane sketch represent cholesterol molecules. *Figure printed with permission from L. A. Bagatolli.*

- Laurdans transition moment is aligned parallel to the membrane normal, i.e. parallel to the hydrophobic lipid chains.

The shift in the emission arises from dipolar relaxation processes of the solvent that are in the same timescale of the fluorescence lifetime of the fluorophore. If a reorientation of the solvent dipoles around the probe transition moment occurs, energy from the excited state of the fluorophore is transferred to the solvent molecules. This results in a continuous red shift in the emission spectrum from blue in the gel phase to green in the fluid phase, as solvent dipole relaxation processes are slower in the gel phase and less energy is transferred (figure 3.14).

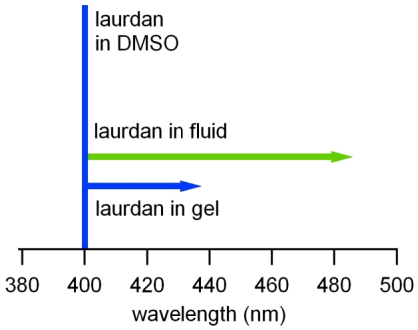

Figure 3.14
Water relaxation processes in membranes in gel state are slower than water relaxation processes in fluid membranes. Therefore a shift in fluorescence is observed as more energy is transferred to relaxation processes in fluid membranes.

In the case of lipid bilayers, the shift in Laurdan emission is due to a change in relaxation dynamics around the lipid head group/hydrophibic chain region where the Laurdan fluorescent moiety resides. As the water dynamics are slower in the gel phase, Laurdan emission is at about 440nm. In the fluid phase the water relaxation dynamics at the head group/chain interface region are higher and therefore Laurdan emission is shifted to about 490nm. Because of the homogeneous distribution of Laurdan in a lipid bilayer it is possible to use the shift in the emission spectrum to assign the phase state of a membrane on the basis of fluorescent pictures using the proper set of emission filters.
The emission spectral changes can be quantified by the generalized polarization (GP) function that was defined in analogy to the fluorescence polarization function [92, 96]:

$$GP = \frac{I_B - I_G}{I_B + I_G}. \tag{3.6}$$

I_B and I_R correspond to the intensities at the blue and the green edge of the emission spectrum, respectively, at a given excitation wavelength. The obtained GP value is characteristic for the phase state of a given membrane and therefore allows the determination of phases [96]. To calculate GP values two microscopy pictures are needed, one of the channel for the green emission and one of the channel for the red emission.
The GP images are calculated with the SimFCS package of the Globals for Images software developed at the Laboratory for Fluorescence Dynamics at Irvine University of California. The fluid phase displays low GP values around -0.1 to 0.2 whereas the gel phase displays high GP values around 0.5 [96].

3.3.7 Differential Scanning Calorimetry

The calorimetric method used to perform the experiments for this thesis is Differential Scanning Calorimetry (DSC). DSC is a powerful method to investigate the phase behavior of lipid

membranes. The thermodynamic properties obtained with this method are the melting point T_m, the change in specific heat Δc_p and the enthalpy change ΔH during a melting transition.

The melting point and the enthalpy change can then be used to calculate the change in entropy, ΔS, during the melting transition as the free energy $\Delta G = \Delta H - T_m \Delta S$ equals zero in the melting transition. This gives a change $\Delta S = \frac{\Delta H}{T_m}$ in entropy.

The main part of the calorimeter are two metal compartments that are shielded with an adiabatic jacket (see figure 3.15). One cell is filled with the sample solution in buffer and the reference cell is filled with buffer only. The two metal cells are temperature controllable with peltier devices and the instrument is programmed to keep the temperature difference between both cells zero. During an experiment the temperature in both compartments is raised or lowered with a defined scan rate. If melting processes in the sample take place, the energy provided to the sample cell is different from the energy provided to the reference cell, in order to keep the temperature difference between both cells zero. From this difference in power supplied, the specific heat Δc_p can be obtained:

$$\Delta Q = \int_{\tilde{t}}^{\tilde{t}+\Delta t} \Delta P dt \cong \Delta P \Delta t \tag{3.7}$$

$$\Delta c_p = \left(\frac{\partial Q}{\partial T}\right)_p \cong \frac{\Delta Q}{\Delta T} \cong \frac{\Delta P \Delta t}{\Delta T}. \tag{3.8}$$

ΔQ is the warmth put into the chambers by applying a power difference ΔP in a time interval $\tilde{t} + \Delta t$ while keeping the temperature difference between both cells zero and changing temperature with ΔT.

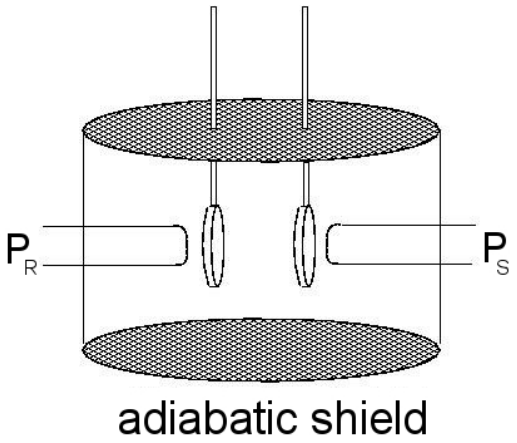

Figure 3.15
The basic parts of a calorimeter — two temperature controllable cells surrounded by an adiabatic shield.

3.3.8 FTIR

In comparison to conventional IR spectroscopy where monochromatic light is used, Fourier Transform Infrared (FTIR) spectroscopy uses a continuous IR light source. This means that

the intensity I reaching the detector of the instrument is a superposition of all intensities $I(\nu)$ of the bandwidth B supplied by the light source for a given mirror displacement x. This intensity will change when a sample is placed in the beam path, as infra red light will be absorbed by different vibrational modes of the sample.
The intensity reaching the detector can be written as

$$I(x) = \int_B I(\nu) \cos(2\pi\nu x)\, d\nu. \tag{3.9}$$

The integral over the bandwidth B can be rewritten to an integral over an infinite range of wavenumbers and a windowing function $D(\nu)$ that has the value one within the bandwidth and zero for wavenumbers that lie outside the bandwidth:

$$I(x) = \int_{-\infty}^{\infty} I(\nu)\, D(\nu) \cos(2\pi\nu x)\, d\nu. \tag{3.10}$$

This equation corresponds to the Fourier Cosine Transformation and for even functions the inverse Fourier Cosine Transformation matches the Fourier Cosine Transformation and is defined as

$$I(\nu) = \int_{-\infty}^{\infty} I(x)\, D(\nu) \cos(2\pi\nu x)\, dx. \tag{3.11}$$

Since for even functions the Fourier Cosine Transformation matches the complex Fourier Transformation equation 3.11 can be rewritten as

$$I(\nu) = \int_{-\infty}^{\infty} I(x)\, D(\nu) \exp(2\pi i\nu x)\, dx. \tag{3.12}$$

With this equation the spectrum $I(\nu)$ can be calculated from the interferogram $I(x)$. This spectrum also contains the detector sensitivity, the energy distribution of the light source and the transmission function of the spectrometer. Therefore a background spectrum has to be subtracted from this spectrum to get the sample spectrum.

The advantages of FTIR over conventional IR spectroscopy are

- with FTIR all wavelengths are scanned at once which makes the technique faster than conventional spectroscopy, where the bandwidth is scanned continuously.
- The mirror position of the Michelson interferometer is controlled with a laser and gives a very high accuracy.
- The intensities are higher than in IR spectroscopy. This results in a better signal to noise ratio.

To follow the lipid melting in the FTIR experiments two approaches were applied. The first approach is similar to a method that was already reported by Leidy et al. [97]: A polynomial baseline was fitted to the water absorption signal underlying CH_2 symmetric stretch and CD_2 asymmetric stretch vibrational absorption peaks and subtracted from the sample spectrum. Then a 3^{rd} order polynomial was fitted to the peak and the peak position was assigned by the derivative. This was done for all temperatures in the interesting temperature range. The melting could then be followed on a wavenumber versus temperature plot. In this case the peak positions of the CH_2 symmetric stretch and CD_2 asymmetric were plotted to follow the lipid

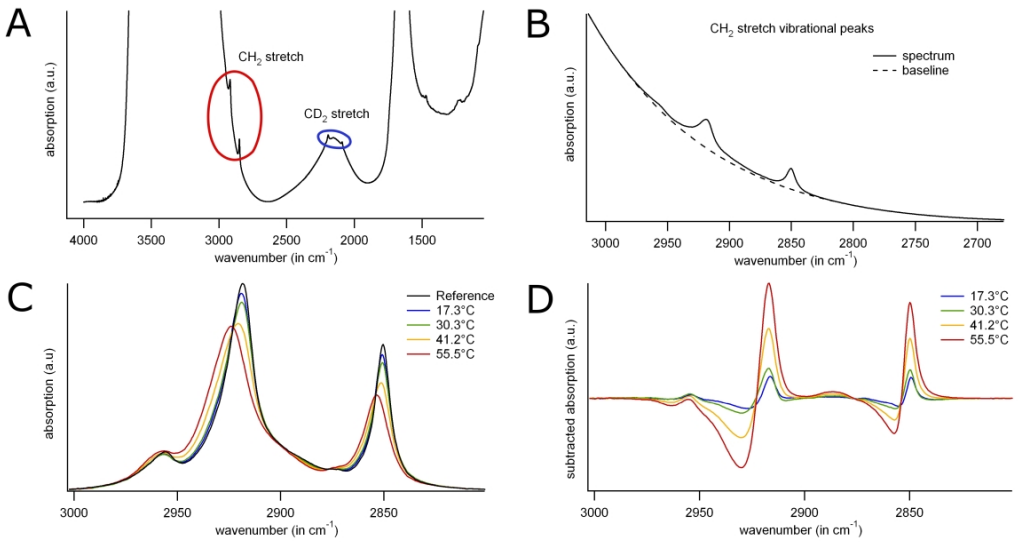

Figure 3.16
The Steps of the FTIR data evaluation procedure. (*A*) The sample spectrum is subtracted from the reference spectrum. The regions of the spectrum where the peaks of the CH_2 and CD_2 stretch vibrations are located are indicated by red and blue ellipses, respectively. (*B*) A polynomial baseline is fitted to the water absorption peak in the region of the CH_2 stretch vibrational peaks. (*C*) The peak areas are normalized to 1cm$^-$1 for all spectra. (*D*) The spectra for all temperatures are subtracted from the reference.

melting.

In the second approach, the difference spectra method (see figure 3.16), the underlying water absorption was fitted in the region of the CH_2 and CD_2 stretch vibrations, respectively, with a polynomial. The water absorption was subtracted from the measured spectra. One of the peaks of the asymmetric or the symmetric stretch vibrational absorption peaks or both peaks were chosen and the peak area normalized to $1cm^{-1}$. The first temperature scan spectrum was chosen as reference and all other subsequent were subtracted from the reference. The resulting spectra were integrated only in the positive range of the axis of ordinates and the results were plotted as area change versus temperature.

In both methods applied, there was no difference between taking one of the two peaks or both together into account for data evaluation.

3.3.9 Black Lipid Membranes

As one cannot see the membrane formed on the teflon septum by visual inspection, its formation has to be proven with another approach. This can be done by applying a triangular voltage signal and monitoring the system reaction during membrane formation. The lipid membrane acts as a capacitor and its capacity is given as

$$C = \epsilon_0 \epsilon_r \frac{A}{d}. \tag{3.13}$$

A is the membrane area that covers the hole in the teflon film, d is the diameter of the membrane, ϵ_0 is the permittivity constant and ϵ_r is the relative permittivity. The hole diameter in the BLM experiments is usually about 60-150µm and the thickness of a bilayer is approximately 5nm. With the relative permittivity of a lipid bilayer (≈ 2), its capacitance should be about 100pF. This value is not reached in experiments because of fringe effects. The effective membrane area is usually lower, but actually difficult to measure.
In BLM experiments the capacitance of the bilayer is measured by applying a symmetric triangle signal to the lipid bilayer (see figure 3.17). The instantaneous current I is

$$I = \frac{\mathrm{d}Q}{\mathrm{d}t} = \frac{\mathrm{d}U}{\mathrm{d}t} \cdot C, \tag{3.14}$$

in which Q is the charge, U is the applied voltage and t is time. Here you can see that the capacitance is proportional to the current measured on the patch clamp setup. If a triangular voltage with a slope of ± 1 is applied, the bilayer capacitance can be easily read from the output signal. In the experiments performed for this thesis the software was calibrated to the gain settings and the output scaling factors of the patch clamp amplifier. In this case the capacitance could be directly read out from the measured maximum current amplitude by multiplying this value by a factor of 0.5, as $\frac{dU}{dt}$ was set to two (see figure 3.17).

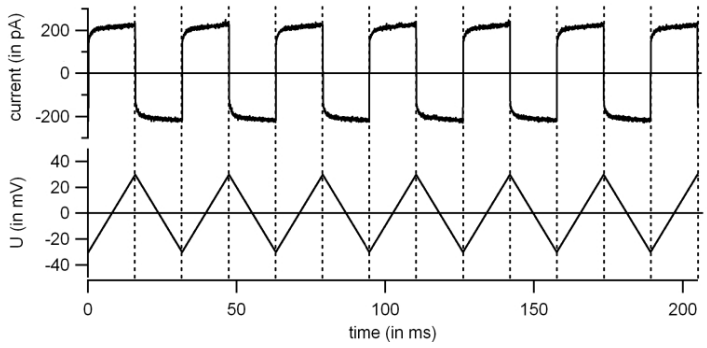

Figure 3.17
A triangular voltage applied to a lipid membrane (lower trace). The measured capacitive response is displayed in the upper trace. The capacitance is proportional to the measured maximum current.

The capacitance test can be used to follow the formation of a lipid bilayer. When the water level in the sample compartment is below the level of the hole in the teflon film, a water film leads to short circuit. Therefore an infinite current amplitude will be measured. If the water level raises, a membrane forms and a finite maximum current amplitude can be measured. In some cases air bubbles or dirt can block the hole and also give rise to a capacitive response. The capacitance value of this blocking is usually a bit lower than the capacitance of a lipid bilayer.
An air bubble usually forms if the hole in the teflon film is not prepainted, so this is an easy way to obtain a capacitance value for blocked hole. It is helpful to measure it for a teflon septum once and to keep it in mind during the execution of experiments.

3.3.10 Atomic Force Microscopy

A comparable new development that established fast in surface science is the Atomic Force Microscope. It has a very good lateral and vertical resolution of about 1nm and 0.1nm, respectively. It can be operated in several modes which have advantages on different kinds of samples, as will be explained in the following. The basic setup of an Atomic Force microscope is displayed in figure 3.18.

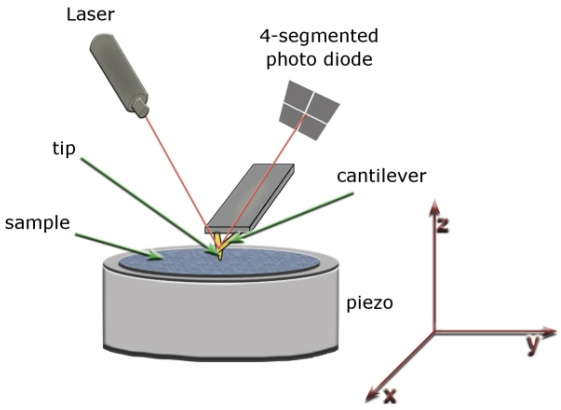

Figure 3.18
The basic setup of an Atomic Force Microscope.

The sample is placed on piece of mica that is in turn placed on a XYZ-piezo. A laser beam is directed on a 4-segmented diode via a cantilever. The cantilever has a very sharp tip. The tip of the cantilever is driven in the rejecting regime of the van der Waals potential of the atoms on the sample surface. The piezo is driven in such a way that the sample moves below the tip. If the height of the sample changes, the cantilever is deflected in vertical direction. Due to this the laser beam is deflected and falls onto another area on the photodiode. In the beginning of the experiment the diode was calibrated in such a way that the laser beams hits the middle of the diode. When the laser beam is deflected, a different intensity in the single segments of the diode occurs.
In the *contact mode*, a feedback mechanism determines the difference signals of the single segments of the photo diode and produces a signal that changes the vertical position of the cantilever, in order to keep the force between sample and cantilever tip constant. The software produces a height profile out of the cantilever deflection and the change of its vertical direction. Together with the height profile calculated from the change in vertical cantilever position, the cantilever deflection picture gives valuable information about the sample. The deflection image has a better contrast usually. The constant force mode works well with solid samples.
On soft samples, like lipid membranes for example, the so called *tapping mode* is advantageous. In this mode, the cantilever is stimulated to oscillate with a frequency of about 220kHz and the sample is scanned in a more gentle way. The electronics of the AFM can calculate the shift of the driving frequency in respect to the oscillation frequency of the cantilever. The shift is depending on the softness sample and results in a phase shift. This shift delivers additional information about the elasticity of the surface. For example, the fluid phase domains are softer than the gel phase domains. Therefore, besides the height difference between gel and fluid areas, the phase of a domain can be derived from the phase shift. The phase shift is stronger the softer the sample.

Part II

Results

Chapter 4

Lateral organization in ceramide containing membranes

Ceramides constitute the hydrophobic backbones of the sphingolipids. Examples of sphingolipids are sphingomyelin, cerebrosides and gangliosides. The molecular structure of a ceramide is shown in figure 4.1: The carboxyl group of a fatty acid is linked to the amino group of a sphingosine or another related long chain base by an amide bond [98].

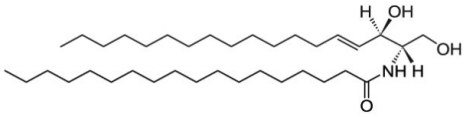

Figure 4.1
Molecular structure of a ceramide molecule

Ceramides have a very small headgroup and therefore the molecule shape is cone-like and induces stress on planar membranes. This has been investigated by Carrer and Maggio [99] in Ganglioside GM1/ceramide monolayers. Natural ceramides are among the more hydrophobic lipids [98] having very high gel to fluid phase transition temperatures. Ceramides are also able to form networks through hydrogen bonds [100] and these properties might give rise to the very low permeability of skin tissue [101, 102], as ceramides are abundant in the Stratum Corneum, the outermost layer of the skin [103]. The very special structure of the skin shields the body from the environment and prevents evaporation of water through the skin [46, 103–105]. Ceramides are also involved in signaling cascades, such as cell differentiation and apoptosis [106]. Many publications state that ceramides are needed to generate apoptosis but the pathway is not known. Recently Siskind et al. [107, 108] reported that in some cases ceramides seem to act as second messenger molecules by ceramide channel formation in the outer mitochondrial cell wall [108] so that cytochrome c can be released [106] from the mitochondria to induce the first step in the intrinsic pathway of apoptosis. To sum up, the biological relevance of ceramides cannot be overlooked but how ceramides act in detail is not precisely known yet. A sticking point in investigating biological membranes is that the diversity of lipids and proteins in these membranes is overwhelming and the influence of a single lipid species on another species might be masked by the influence of all the other molecules present. Therefore model membranes consisting only of a few different lipid species can be a good approach to understanding ceramide action in more detail.

Ceramides containing model membranes have already been studied in the past and observed fea-

tures of these membranes are lateral organization [109–114], ceramide channel formation [107] and vesicle budding [115]. In the case of POPC/ceramide mixtures the results concerning domain formation are controversial. Massey reports that no ceramide rich domains were detected in the System POPC/ceramides by Laurdan GP measurements in cuvette and DPH anisotropy measurements [112], but Hsueh et al. in contrast found evidence for domain formation in POPC/ceramide membranes with deuterium NMR techniques [113]. Domain formation in lipid systems by microscopy means has been observed for other lipid mixtures [28, 29] on Giant Unilamellar Vesicles, but had to our knowledge not been studied on POPC/Ceramide containing lipid vesicles before.

This chapter focusses on the investigation of POPC membranes containing Ceramides at different ratios and it will also refer to the influence of cholesterol on this system. Confocal fluorescence laser scanning microscopy (CFLSM) and two photon microscopy are used to investigate whether or not POPC/ceramide GUVs display phase separation observable in the micrometer scale to solve the discrepancy in the reports by Massey [112] and Hsueh et al. [113]. These experiments were combined with Atomic Force Microscopy (AFM) to investigate nano scale domain formation and calorimetry to give insight into additional thermodynamic parameters, such as changes in specific heat and enthalpy. FTIR was used to investigate the melting of the individual lipid species[1].

4.1 POPC/ceramide mixtures

4.1.1 Confocal and Two Photon Microscopy

Dil-C_{18} was used to investigate the lateral organization of POPC/ceramide GUVs. Two different regions can already be observed with 5 mol % ceramides (upper row in figure 4.4A). One region does not show Dil-C_{18} fluorescence whereas the other phase shows strong Dil-C_{18} fluorescence. The area of the dark domains increases with increasing amount of ceramides and this indicates that the dark areas might be ceramide rich gel domains. To get more insight into the lateral pattern observed on the POPC/ceramide GUVs and to be sure in which phase Dil-C_{18} accumulates, two photon microscopy with laurdan was performed. The Laurdan intensity pictures in the middle row of figure 4.4A show that the amount of fluid phase decreases with increasing amount of ceramides and the Laurdan GP pictures in the lower row of figure 4.4A show high GP values in the gel phase and low GP values in the fluid phase. Additionally, the photoselection effect is observed in the gel phase. The Laurdan GP value for the POPC rich fluid phase slowly increases with increasing amount of ceramides and indicates a slight increase in lateral packing of the lipids. The Laurdan GP value for the gel phase does not change with increasing ceramide molar fraction.
In addition to the change in POPC/ceramide composition the temperature dependence of the Laurdan GP values was investigated on GUVs composed of a POPC/ceramide 5:1 mixture, the results are displayed in figure 4.2B.
The two rows show snapshots of a vesicle at different temperatures during a heating cycle starting at a temperature above the liquidus temperature in figure 4.2*a*. At temperatures

[1] The study on the POPC/ceramide/cholesterol lipid system had already started when I joined the MEMPHYS group in September 2004. It is a study where many different techniques were applied by several experimentalists [81]. I contributed with the calorimetric experiments and I was involved in the writing process of the publication.

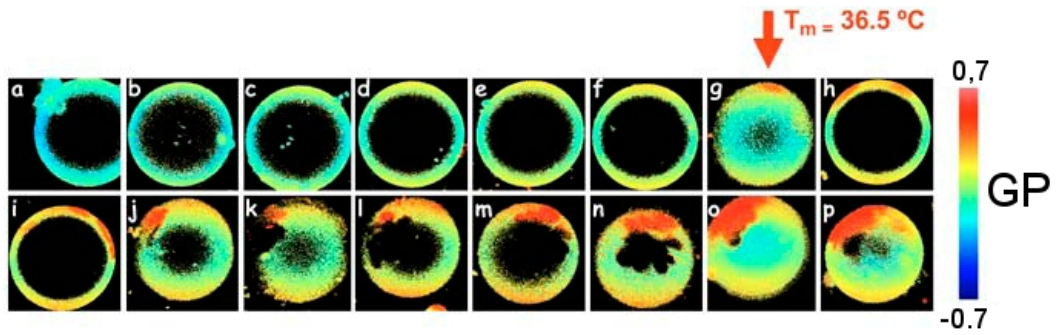

Figure 4.2
GP values for a GUV obtained at different temperatures. The temperature was highest in picture (a) and decreases bit by bit until picture (p). Domains become visible in picture (g), corresponding to a temperature of 36.5°C.

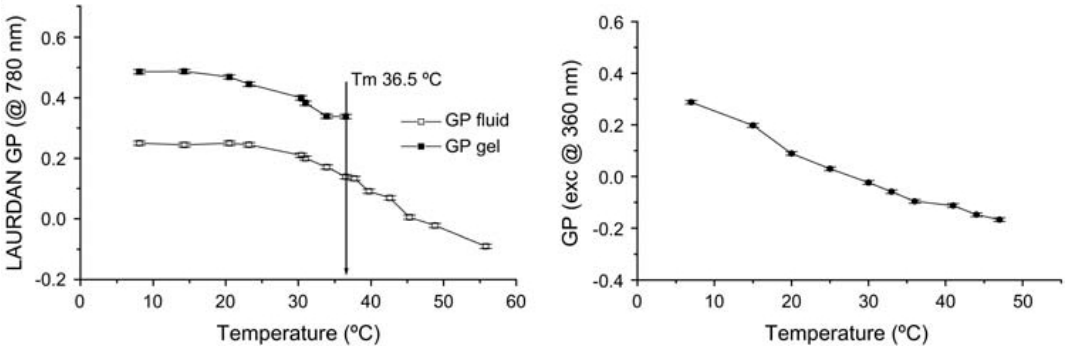

Figure 4.3
(*left*) LAURDAN GP measurements on domains of POPC/ceramide GUVs. (*right*) GP values obtained from bulk measurements of POPC/ceramide multilamellar vesicles in cuvette.

above 35.6°C the pictures taken on the equatorial region of the vesicle show a low GP value (see scale on the right side of figure 4.2), corresponding to fluid-like phase. In picture 4.2*g* a gel-like domain emerges at a temperature of 36.5°C and grows in size as temperature is decreased.

The GP values measured at different temperatures in the gel and the fluid phase regions are displayed in the left hand graph of figure 4.3. At low temperatures (10°C) the GP value of the gel phase is about 0.5 and the GP value in the fluid phase is about 0.25 (see also figure 4.2*p*). The GP values stay constant up to a temperature of about 20°C and then drop to a value of about 0.35 in the gel phase and 0.15 in the fluid phase at a temperature at 36.6°C. From the Two Photon Microscopy pictures we obtain a melting point of 36.5°C. At higher

temperatures only one fluid phase is observed and the GP value drops from 0.15 at 36.5°C to -0.05 at 55°C. Laurdan GP values obtained for bulk measurements in cuvette do not show discontinuities that would indicate phase separation (figure 4.3 right). This shows that the water dipolar relaxation processes decrease with decreasing temperature, in accordance with the overall trend for Laurdan GP measurements on single vesicles.

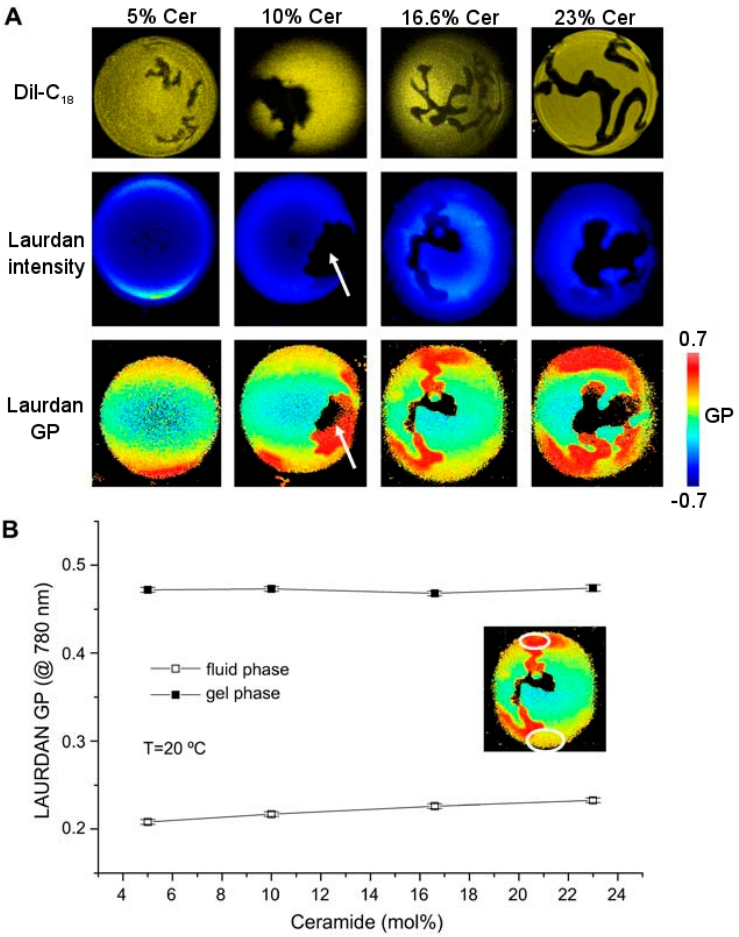

Figure 4.4
Confocal and Two Photon Microscopy pictures of vesicles made of POPC with different amounts of ceramides (*A*) show that Dil-C_{18} participates into fluid phase domains and that the gel phase domain area increases with increasing amounts of ceramide membrane content. The GP values displayed in the lower graph (*B*) show that the GP value of the fluid phase increases with increasing ceramide membrane content. This means that the water relaxation processes in the fluid phase decrease and that the fluid domains get more stiff.

4.1.2 Atomic Force Microscopy

Phase coexistence was also observed for planar supported membranes consisting of POPC/ceramide mixtures. The setup used for the experiments is an AFM combined with an fluorescence microscope. From the fluorescence microscopy experiments on planar supported membranes, separation of Dil-C_{18} into two regions, one showing strong fluorescence, the other no fluorescence (see figure 4.5A) was observed. Comparison of these pictures with AFM topography pictures verifies the observation from the GUV experiments that Dil-C_{18} segregates into the fluid phase because the strongly fluorescent areas are the fluid domains, as they have a lower height in the AFM images than the gel domains (see figure 4.5B). The height difference between gel and fluid domains is about 1.2 ± 0.1nm, in agreement with previous published data on other lipid mixtures displaying gel/fluid phase coexistence [8, 116, 117]. The AFM

picture taken in tapping mode also indicates that the strongly high fluorescent areas are the fluid domains because they show a higher phase shift that is due to the higher softness of the fluid phase (see figure 4.5D). The domain size in the supported lipid bilayers matches the domain size observed in GUVs.

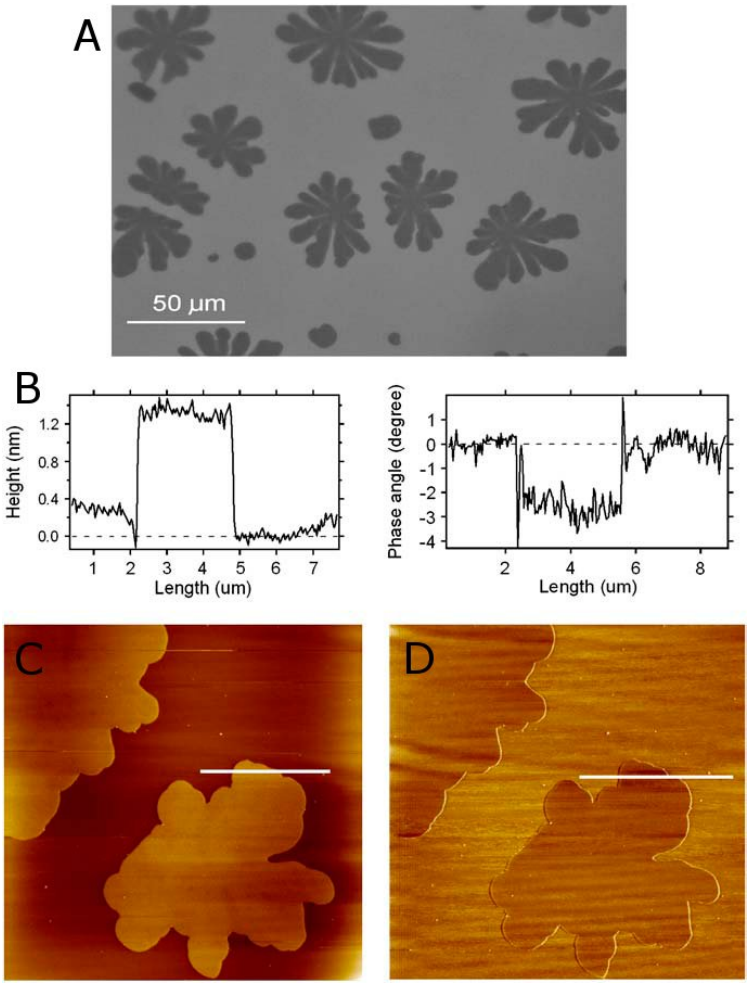

Figure 4.5
(*A*) Fluorescence image of a POPC/ceramide (5:1 molar ratio) membrane labeled with DiI-C_{18}. (*B*)Height information extracted from AFM pictures showing a height difference of 1.2± 0.1nm between gel and fluid phase domains. (*C*) Height topography image from AFM. (*D*) Phase contrast image from AFM.

4.1.3 Calorimetry

The thermograms of POPC/ceramide vesicle preparations with different POPC/ceramide mixing ratio are displayed in figure 4.6.
For pure POPC a melting transition is observed at -2.6°C in accordance with previously published data [118]. Pure ceramides show a phase transition at 80°C. Addition of up to 30% molar fraction of ceramide leads to a broadening of the peak at low temperatures corresponding to the melting of the POPC rich phase. The enthalpy of this transition decreases from 21.3 to 3.8kJ/mol (see table 4.1). With addition of ceramides a second peak at higher temperatures is observed in comparison to the pure POPC DSC trace. This peak is situated at about 24°C for 5% ceramide membrane content and shifts to approximately 45°C at 30% ceramide fraction. In

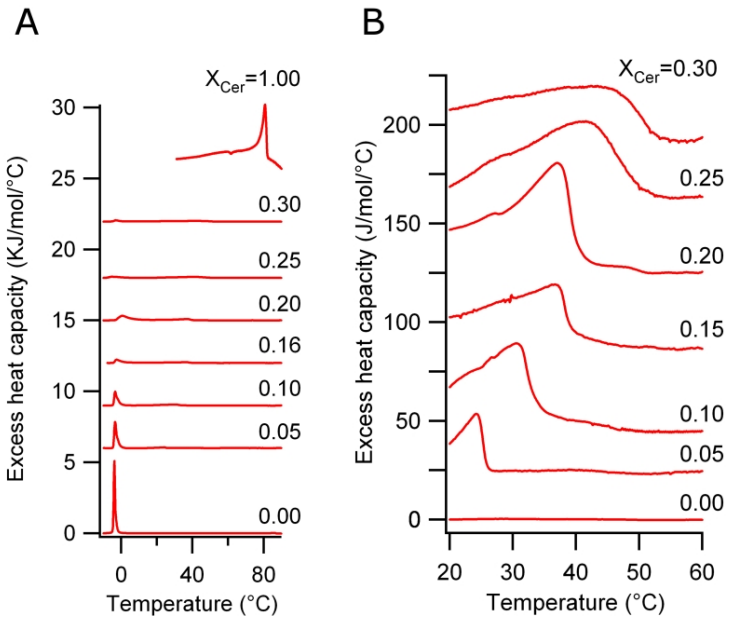

Figure 4.6
Calorimetric scan results for POPC/ceramide vesicles at different mixing ratios. (A) Complete scan from -7 to 90°C. (B) temperature range where high temperature melting peak is located, the data has been multiplied by a factor 10 in comparison to A.

Table 4.1
Melting temperatures and enthalpies of the POPC and ceramide-rich phases extracted from the peaks in calorimetry compared to the melting temperature observed in GUV experiments.

mol % ceramides	DSC T_{low} [°C]	DSC T_{high} [°C]	GUV T_{high} [°C]	DSC ΔH_{low} [kJ/mol]	DSC ΔH_{high} [kJ/mol]
0	-3.7	—	—	21.3	—
5	-3.4	24.7	24.0	15.9	—
10	-3.4	30.3	31.0	6.7	3.5
15	-2.7	37.0	36.2	14.7	3.6
20	-0.7	37.3	38.0	14.7	9.1
25	-5.1	41.1	42.0	3.8	16.0
30	-3.1	43.5	—	—	—

addition, this high temperature peak, corresponding to the ceramide rich phase, broadens with increasing amounts of ceramides in the membrane. The enthalpy of this transition increases from 3.5kJ/mol with 10% ceramides to 7.5kJ/mol at 30 mol % ceramides (see table 4.1). The calorimetric data shows that POPC/ceramide mixtures display a broad phase coexistence regime and the temperature where Phase coexistence is indicated by DSC matches the temperature where domains are observed in microscopy. The DSC and GUV experiment results are compared in table 4.1.

4.1.4 FTIR spectroscopy

Temperature dependent FTIR scans were performed on a dPOPC-d31/ceramides 5:1 mixture and the result is shown in figure 4.7.

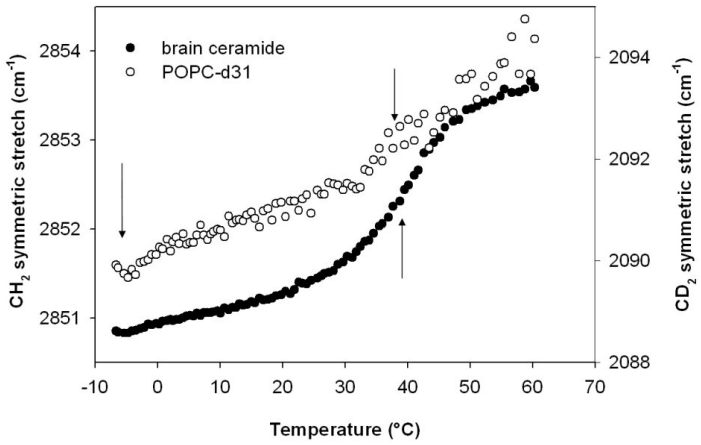

Figure 4.7
Temperature ramp FTIR scan of a POPC/ceramides 5:1 lipid mixture. A deuterated POPC component is used so that the shift in wavenumber can be monitored independently for POPC and ceramides.

For the FTIR experiments deuterated POPC (dPOPC-d31) has been used so that the melting of deuterated POPC can be monitored independently from the ceramides as the symmetric and the asymmetric vibrational peaks of the deuterated POPC shifts to lower wavenumbers because of the higher mass of the deuterium atoms. It has to be noted that only one chain of dPOPC-d31 is deuterated so that ceramide melting cannot be monitored independently from the dPOPC-d31 because the undeuterated chain of dPOPC-d31 will give a signal at the same wavenumber as ceramides. However, the graph in figure 4.7 shows that dPOPC-d31 shows melting events at about -5°C, as the change in wavenumber for the CD_2 symmetric stretch vibrations is increased. This melting corresponds to the melting events in the POPC rich phase. The melting is observed at lower temperatures as for the undeuterated POPC sample because deuterated lipids melt at a lower temperature compared to the corresponding undeuterated lipids [119, 120]. Additionally at about 37°C an increased change in wavenumber for the dPOPC-d31 fraction is observed, where the ceramide rich phase melts. From this result it becomes very clear that a minor fraction of dPOPC-d31 is also present in the ceramide rich gel phase and these dPOPC-d31 molecules melt together with the ceramide molecules at a temperature of approximately 37°C for a dPOPC-d31/ceramide 5:1 lipid mixture.
Ceramides will also be present in the POPC rich fluid phase, but their melting cannot be investigated independently from the dPOPCd31 molecules. Most of the signal from the CD_2 symmetric stretch vibrational absorption will come from the POPC in the case of the melting events observed at about -5°C. However, most of the ceramide rich phase melts at about 40°C, as can be seen from figure 4.7. In the case of the ceramide rich phase the dPOPC-d31 signal overlay will be minimal.

4.2 POPC/ceramide mixtures containing cholesterol

4.2.1 Confocal and Two Photon Microscopy

POPC/ceramide 5:1 lipid mixtures containing different amounts of cholesterol were investigated and the microscopy pictures as well as the extracted GP values are shown in figure 4.8.

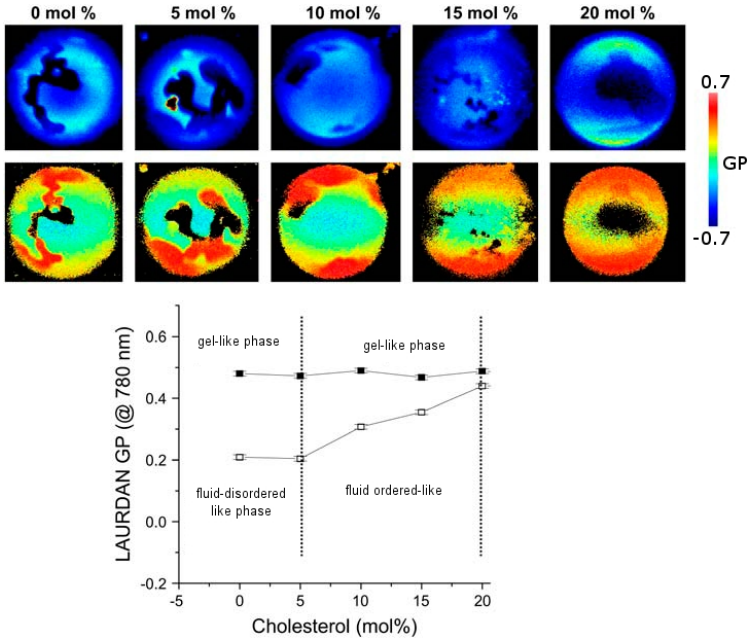

Figure 4.8
Two photon excitation (top, upper row) pictures and the corresponding GP values (top, lower row) for a POPC/ceramides 5:1 lipid mixture with different amounts of cholesterol. The change in GP values is displayed in the bottom graph.

The GP values for the POPC rich phase do not change from 0% to 5% cholesterol membrane content but stay at a low level of 0.2 corresponding to fluid disordered phase. Increase of cholesterol membrane content from 5% to 20% augments the GP value continuously to a GP value of 0.42 at 20 mol % cholesterol membrane content. The GP value obtained for the ceramide rich phase stays at a constant value of about 0.48. This value has been found for gel-like phases before [29, 92].
The regions observed on the GUVs change dramatically above 22 mol % cholesterol membrane content, as shown in figure 4.9
At 22 mol % cholesterol three different regions are observable on POPC/ceramides 5:1 GUVs using Dil-C_{18}. There is a non fluorescent region (NFR) and that NFR is usually surrounded by a line shape region (LSR). Dil-C_{18} is not partitioning into the NFR but is to some extent partitioning into the FR and most strongly into the LSR. The NFR is facetted and resembles a crystal like structure. Using Laurdan we observed high GP values in the LSR and the FR, corresponding to a very low extent of water dipolar relaxation processes in the membrane (0.43 and 0.44 respectively). This last fact suggests a high lateral packing in these domains in the GUVs. Surprisingly, Laurdan emission is also observed in the polar region in the LSR of the GUVs where it is usually not observed, due to the photoselection effect (see section 3.3.5). This indicates some special orientation of the Laurdan probe in the LSR as Laurdan emission is usually not expected in high GP value domains in the polar regions of the vesicles [92, 121]. The formation of the three regions observed above 22 mol % and up to 30 mol % of cholesterol in POPC/ceramides 5:1 membranes is reversible with respect to changes in temperature. The fact

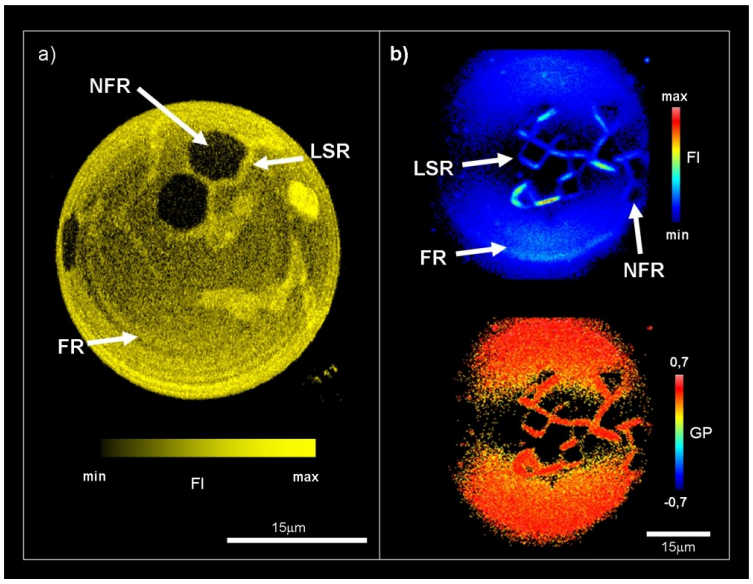

Figure 4.9
Confocal (*left*) and two photon microscopy (*right*) images of a POPC/ceramide 5:1 lipid mixture with 26 mol % cholesterol at room temperature. Three regions, a non fluorescent region (NFR), a line shape region (LSR) and a fluorescent region (FR) are observed in the membrane.

mol % ceramides	DSC T_{low} [°C]	DSC T_{high} [°C]	GUV T_{high} [°C]
0	-3.7	—	—
5	-3.4	24.7	24.0
10	-3.4	30.3	31.0
15	-2.7	37.0	36.2
20	-0.7	37.3	38.0
25	-5.1	41.1	42.0
30	-3.1	43.5	—

Table 4.2
Melting temperatures of a POPC/ceramide 5:1 mixture containing different amounts of cholesterol extracted from the peaks in calorimetry compared to the melting temperature observed by GUV experiments.

that the formation of the three different regions is independent of the direction of temperature change, indicates that there is no thermal hysteresis in this process. Additionally, it can be observed that the temperatures at which these structures occur match the temperatures where phase separation is seen in DSC (see table 4.2).

4.2.2 Calorimetry

The calorimetric results for the POPC/ceramide mixture 5:1 with different amounts of cholesterol are shown in figure 4.10.

With increasing amount of cholesterol in the membrane the POPC rich phase endotherm at lower temperature broadens, but does not change its position. The broadening indicates a decrease in cooperativity as the liquid ordered POPC rich phase is formed. The high temperature endotherm, corresponding to the ceramide rich phase, is shifted to lower temperatures with increasing cholesterol concentration from 0 to 30 mol % in the membrane. The observed peak position for the ceramide rich phase well matches the melting temperatures observed in the GUV experiments, as can be seen from table 4.2.

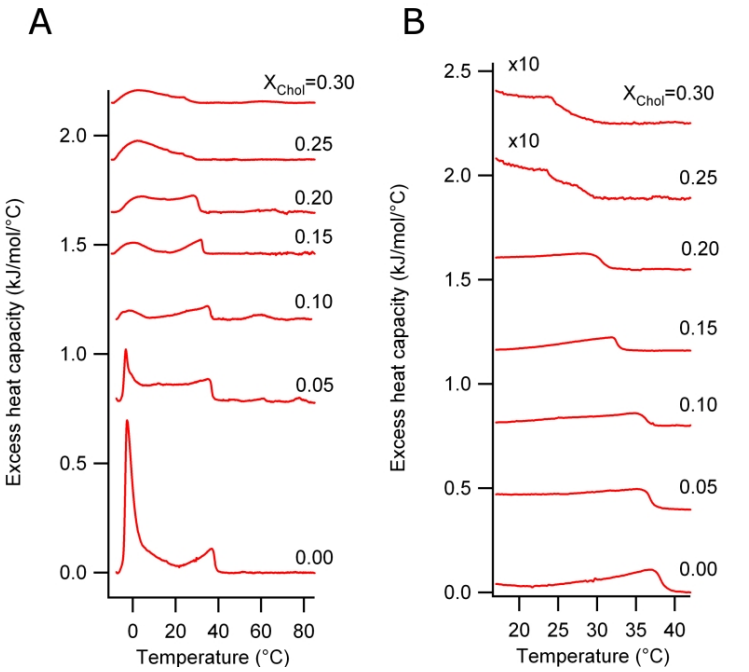

Figure 4.10
DSC thermograms of MLV composed of POPC/ceramides (5:1 mol) and different amounts of cholesterol (from 0 to 30 mol %). (A) complete scan from -10 to 90°C; (B) temperature range of the ceramide rich phase melting events at high temperatures. The high temperature endotherm shifts to lower temperatures as cholesterol molar fraction is increased.

4.2.3 FTIR spectroscopy

A dPOPC-d31/ceramide 5:1 lipid mixture containing 26 mol % cholesterol was investigated with FTIR and the results are shown in figure 4.11. The CH_2 symmetric stretch shows a pronounced change in wavenumber at about 22°C, indicating increased melting events in this temperature region. This temperature matches the high temperature peak found with DSC for the same lipid mixture very well (see figure 4.10). However, the asymmetric CD_2 stretch vibrations do not show a significant change in wavenumber in this high temperature region as will the same lipid mixture without cholesterol. Actually, the wavenumber for the deuterated component does not show an intensified increase in wavenumber over the whole temperature range. This matches the calorimetric finding that the low temperature peak is abolished with higher cholesterol membrane content (see section 4.2.2).

4.2.4 Atomic Force Microscopy

Atomic Force Microscopy was applied to investigate the influence of 15 mol % cholesterol and 22 mol % cholesterol (see figure 4.12) on POPC/ceramides 5:1 mixtures.
Membranes with 15 mol % cholesterol displayed uniform domains with a height difference of 0.7±0.1nm between POPC rich and ceramide rich domains (see figure 4.12A), in contrast to approximately 12nm for POPC/ceramides without cholesterol (see figure 4.5B). At 26 mol % cholesterol two different domain types with different height characteristics were observed, one showing a height difference of 1.2±0.2nm and the other one showing a height difference of 0.6±0.2nm between POPC rich and ceramide rich domains respectively (see figure 4.12B and 4.12C). Interestingly, exposure of the membrane containing 26 mol % cholesterol to methyl-β-cyclodextrin that removes cholesterol from the membranes restores the system to a configuration observed in POPC/ceramide membranes without cholesterol (see figure 4.12D).

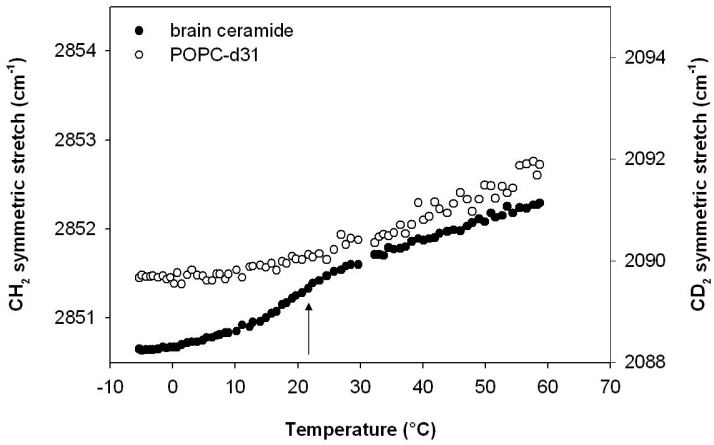

Figure 4.11
change in wavenumber of the asymmetric CD_2 and symmetric CH_2 stretch of a POPC/ceramides 5:1 mixture with 26 mol % cholesterol.

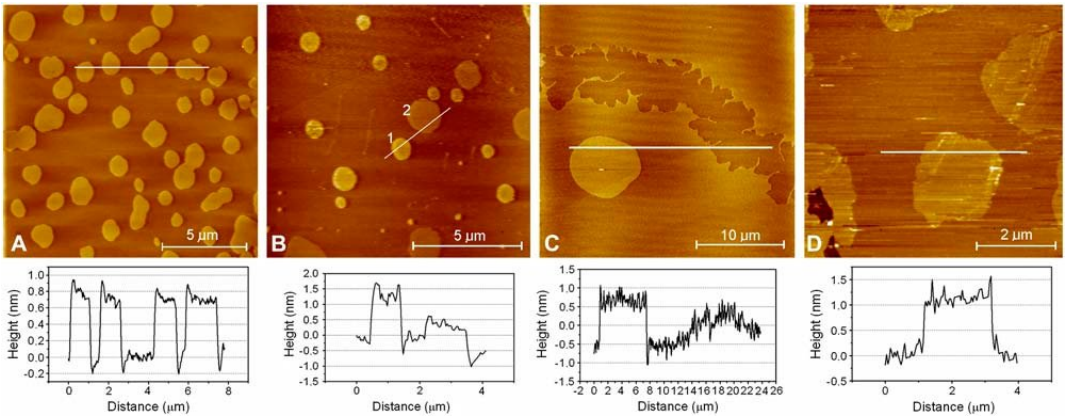

Figure 4.12
AFM pictures of POPC/ceramides 5:1 (mol) with (A) 15 % cholesterol; (B and C) 26% cholesterol and (D) after removal of cholesterol with methyl-β-cyclodextrin from membranes containing 26 mol % cholesterol (10mg/ml, 10 min).

4.3 Discussion

4.3.1 POPC/ceramide mixture

The experiments clearly show that POPC/ceramide mixtures display gel/fluid phase coexistence over a broad temperature range in the investigated composition range up to 30 mol % ceramide membrane content. Microscopy shows striped/flower-like domain shapes and partial miscibility can be concluded from the GP values on GUVs, DSC and FTIR experiments. This is in contrast to the result reported by Massey [112] where no phase separation was reported from GP measurements in cuvette. The results presented here show that ceramide affects the lateral organization in POPC membranes even at a very low ceramide concentration. Our results are in agreement with the observations reported by Hsueh et al. [113] for a POPC/palmitoyl

ceramide mixture. Even though we used porcine brain ceramides, which is a complex mixture of ceramides, the phase diagram deduced by Hsueh et al. matches very well with the lateral features of POPC/porcine brain ceramide model membranes in the temperature range explored in our work. This is interesting because it shows that it is possible to reduce a very complex system to a simpler binary mixture and the observed features do not alter much so that the information obtained for the simple system can also be used for interpretation of the more complex system. Hsueh et al. [113] claim the existence of a metastable solid ceramide phase above 20 mol % of ceramide, but this was neither seen in any our of experiments by visual inspection of GUVs or planar membranes in AFM nor by GP value nor in the DSC experiments. DSC measurements were performed up to 90°C and pure ceramide crystal formation would be reflected by an endotherm at about 80°C, but this was not the case. But this discrepancy could of course be related to the fact that we used a complex porcine brain ceramide mixture in contrast to the binary POPC/palmitoyl ceramide mixture used by Hsueh et al.

What makes this work very interesting is the merger of several different techniques that include bulk measurements, such as IR spectroscopy, DSC and FTIR as well as measurements on single GUVs or planar membranes, such GP value calculation on domains and AFM experiments. This gives far more insight into the system and shows that misinterpretations could be drawn if only bulk experiments are performed. The misinterpretation Massey concluded from bulk experiments in spectroscopy on a POPC/ceramide system with 0 to 10 mol % ceramides [112] probably stems from some peculiarities of the lipid system.

Furthermore we observed no discontinuities in our bulk Laurdan GP temperature profile at the temperature where nucleation is expected, as it can be seen from microscopy, DSC, FTIR and AFM. This discrepancy can be explained by considering the additive property of the anisotropy function [122] that was based on the early observations of Gregorio Weber on the additive properties of the polarization function [123]. The additive property is also valid for the GP function and can be expressed as

$$GP_{av} = X_g GP_g + X_f GP_f, \tag{4.1}$$

where X_g and X_f represent the fractional contribution of the gel and the fluid phase domains respectively and GP_g and GP_f are the GP values obtained from the gel and the fluid phase domains respectively. X is not depending on the molar fraction but is depending on the concentration of the probe in the different domains of a sample and also on the total area fraction of gel and fluid phase. Laurdan distributes homogeneous in a lipid membrane showing phase separation and therefore in the case of Laurdan X is only depending on the total area fraction of gel and fluid phase in the membrane. However, the area of a lipid molecule in gel state is about one-third of the area of a lipid molecule in fluid state and therefore the molar fraction of lipids in gel and fluid phase does not correlate directly with the total area fraction. That means if, for example, total immiscibility of the two lipid species of a binary mixture is assumed, the contribution to the GP value of a fixed amount of lipids in a gel phase domain will always be lower than the contribution of the corresponding lipids in a fluid phase domain. Taking into account this effect we can speculate that a high amount of gel phase area is needed to see a discontinuity in the bulk GP temperature profile. In the case of ceramides, we were not able to form GUVs with more than 30 mol % ceramide membrane content and we therefore constricted all experiments to this upper ceramide concentration boundary. POPC/ceramide mixtures show low melting cooperativity in the DSC experiments and an increase in water relaxation processes

with increasing temperature (see figure 4.3, left panel) will mask the discontinuity in the bulk GP measurements even more. The above conclusion drawn for bulk GP measurements in cuvette can also be drawn for Massey's bulk DPH anisotropy measurements in cuvette [112]. DPH distributes homogenously in membranes showing gel/fluid phase coexistence as Laurdan does and therefore no discontinuity in DPH anisotropy can be measured for POPC/ceramide membranes with low ceramide membrane content.

However, Massey might have drawn a different conclusion from his results on POPC/ceramide bulk cuvette experiments published in [112], if he had had the possibility to measure his samples at lower temperatures, preferably starting at about -5°C. As he only included up to 10% of ceramides, POPC is the major component and therefore most of the melting events are expected to happen at -2°C when the major POPC fraction is melting, as can be seen from DSC (see figure 4.6).

The hypothesis that similar acyl chain length between POPC and natural occurring ceramide precludes phase separation in mixtures of both species [112] can no longer be sustained. Our experiments show phase separation on GUVs and planar supported membranes in AFM consisting of POPC/ceramide mixtures and these observations fit very well with the evidence for phase separation obtained in bulk experiments in DSC and FTIR. The fact that ceramides segregate laterally into ceramide rich domains might be due to the fact that ceramides have a very small headgroup [113, 124] with a low tendency for hydration and that ceramides have a strong tendency to interact via hydrogen bonding [100].

4.3.2 POPC/ceramide/cholesterol mixture

The results on the POPC/ceramide mixture containing different amounts of cholesterol can be divided into two regions, one ranging from 0 mol % to 20 mol % cholesterol membrane content. Probably, the most striking result obtained for membranes consisting of POPC/ceramide/chol lipid mixtures with up to 20 mol % cholesterol, is the occurrence of liquid ordered/solid ordered phase coexistence, which is in contrast to the liquid disordered/liquid ordered phase coexistence observed in other lipid mixtures containing ceramide-based lipid molecules [125]. The Laurdan GP value in the POPC-rich fluid phase shows a gradual increase from 0.2 to 0.42 as cholesterol membrane content increases (see figure 4.8). This points to a gradual ordering effect of cholesterol on the POPC-rich fluid phase as cholesterol partitions into the fluid phase which can be seen from the broadening of the low temperature peak of the DSC thermogram (see figure 4.10). The GP value of 0.42 matches the GP value obtained for liquid ordered phases in the work of Dietrich et al. [125] at nearly the same temperature.

The GUV experiments show that cholesterol does not affect the water relaxation processes in the ceramide rich domains of the membrane as the GP value does not change (see figure 4.8). From the shape of the domains differing from roundish, as it is observed for liquid disordered/liquid ordered phase coexistence, and the GP values of 0.42 in the POPC rich phase and 0.5 in the ceramide rich phase, we conclude liquid ordered/solid ordered phase coexistence for POPC/ceramides/cholesterol lipid membranes in the phase coexistence regime. An effect of cholesterol is also observed in AFM experiments, where the height difference between the domains decreases upon addition of cholesterol (see section 4.2.4). This has also been reported by other groups [126–128]. Saslowsky et al. [127] also state that addition of cholesterol presumably increases the height of the DOPC-rich phase. This is also the case in our experiments, which

means that cholesterol incorporated into POPC/ceramide membranes increases the thickness of the POPC-rich fluid phase. This would be expected when the fluid phase becomes more ordered-like, as it is seen in the GUV GP experiments. The height difference between gel and fluid phase decreases, as we observe in our AFM experiments. It is interesting to note that the ceramide-rich phase melting peak at high temperatures in the DSC thermogram shifts to lower temperatures upon addition of cholesterol (see section 4.2.2), but no change in the Laurdan GP values taken from GUVs is observed (see section 4.2.1). This means that addition of cholesterol seems to change the melting temperature of the ceramide rich phase, probably by a changed composition of that phase, but the hydration properties and therefore the lateral packing is not altered. Additionally, POPC/ceramide/cholesterol GUVs show a different lateral pattern than lipid mixtures displaying liquid disordered/liquid ordered phase coexistence. In those experiments with POPC/Sphingomyelin/cholesterol or DOPC/SM/chol, DOPC/DPPC/chol, pulmonary surfactant and brush border membrane lipid extracts, for example, circular domains are observed [13, 14, 125]. Fluid circular domains will emerge when liquid ordered phase is coexisting with liquid disordered phase because both phases are isotropic and line tension will be reduced by an optimal area/perimeter ratio. In the case of POPC/ceramides/chol elongated gel domains are observed because the crystal like properties will induce anisotropy. The liquid ordered/solid ordered phase coexistence in POPC/ceramide/chol membranes might be the reason for ceramide occurrence in several biological relevant processes, such as apoptosis [106].

A very complex lateral pattern is observed in POPC/ceramide mixtures with more than 22 mol % cholesterol. Based on the information from the fluorescent probe DiI-C_{18} three distinct regions occur. Non-fluorescent regions (NFR), fluorescent regions (FR) and line shape regions (LR)(see figure 4.9) coexist in the membrane plane. Especially the information provided by the Laurdan photoselection effect is very interesting. Usually Laurdan shows emission in fluid phase domains and no emission in gel phase domains in the top region of GUVs (see section 3.3.5). However, in the case of POPC/ceramide 5:1 lipid mixtures with more than 22 mol % cholesterol strong Laurdan emission is detectable in the polar region of GUVs in the LSR. The Laurdan GP value in these areas is also high and corresponds to highly ordered phases that should not show Laurdan emission in gel phase in the top region of GUVs. The FR shows a high GP value and the fact that the photoselection effect is present in the case of the FR regions leads to the conclusion that the FR regions are liquid ordered like. This means that the only difference between the FR and the LSR is the orientation of the Laurdan probe that can be related with the lipid orientation in the membrane. The hexagonal shape of the NFR suggests crystalline packing for these regions. These crystals could be composed of pure lipid species, either ceramide or cholesterol, but this idea is not supported by the other experiments, only the fact that Laurdan is expelled from these regions. This is unexpected, as Laurdan usually distributes homogeneously in membranes showing phase coexistence [92, 121]. Speaking against this hypothesis is the fact that no melting transition is observed in DSC, for example, which should be the case if pure ceramide phase were present.
Also the results obtained with AFM change when cholesterol membrane content gets higher than 22 mol %. At these high concentrations domains with different shapes and varied height differences are observed in the supported bilayers. This effect can be reversed by extraction of cholesterol with methyl-β-cyclodextrin from the membranes. In this case the domain pattern returns to the pattern observed for POPC/ceramide membranes without cholesterol (see figure 4.12). Of course, as the ceramides used for the experiments described in this thesis are heterogeneous, it is conceivable that ceramide molecules with different chainlength might segregate into different domains under the impact of cholesterol. So far we are not able to

present a model on what happens in the POPC/ceramide/cholesterol mixture with more than 22 mol % cholesterol. If Laurdan is still aligned parallel to the lipid chains then the lipids have to be aligned perpendicular to the membrane normal if Laurdan emission is detected in gel-like phases in the top region of a vesicle. This could be the case if ceramide channels form like Siskind et al. reported for membranes containing C_2 and C_{16} ceramides and cholesterol [107, 108, 129]. Probably those channels are formed because of ceramides ability to form networks via intermolecular hydrogen bonding [100, 130].

4.4 Outlook

This chapter has shown that ceramide induces a very peculiar phase behavior that differs from the phase behavior of other sphingosine based lipids.
As ceramides are reported to participate in cell death, future experiments should try to reveal whether the observed line shape regions carry ceramide pores or not. As a critical concentration of ceramides is needed to form ceramide channels in membranes [107, 129], phase separation can induce a locally increased ceramide concentration in gel domains. The local increase of concentration of specific lipid species above a threshold level has been shown for Phospholipase PLA_2 activation by Leidy et al. [131] and might also play a role in ceramide channel formation — the ceramide concentration in the ceramide rich phase will be higher compared to the ceramide concentration of a homogeneous membrane.
In order to get experimental evidence for ceramide channels in the line shape regions confocal microscopy experiments in ion containing buffer could be performed. If a dye is used that is sensitive to ion concentrations it should also give emission in the pore containing domains, but not in the membrane itself. One explanation, if this approach fails, could be the fact that the membrane thickness is only 5nm.
Additionally there is a recent publication about a combined AFM and conductance measurement setup on nanopores. The technique is not completely established yet, but it is planned to use this method to combine AFM height measurements with electrical conductance measurements [132]. This technique would be suited perfectly to measure if ceramide channels are formed in the gel domains.

Chapter 5

Lateral organization of cerebroside containing membranes

Cerebrosides are ceramide based lipids that can be found in various tissue, for example skin, kidney, epithelial cells of the small intestine and colon as well as in the myelin sheath of nerve tissue [133–137]. Chemically, cerebrosides are composed of a galactose and a ceramide moiety. There is a wide variety of cerebrosides species and they are divided into the class of galactosylceramides, glucosylceramides and zwitterionic glycosphingolipids. For the experiments performed within the framework of this thesis galactosylceramides (GalCer) extracted from porcine brain were used. The cerebroside extracts are a mixture of cerebrosides with different chain length and degrees of saturation (see table 5.1). A representative structure is displayed in figure 5.1.

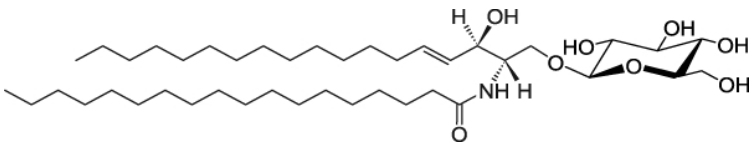

Figure 5.1
Representative structure of a galactosylceramide extracted from porcine brain. *Figure taken from www.avantilipids.com.*

Galactosylceramides are found in all nervous tissue but to a higher degree in white matter compared to grey matter [138, 139]. The most predominant constituent of white matter is the myelin sheath of the axons, which constitutes about 50% of white matter [140]. Myelin has

chainlength	% of total	
16:0	6	saturated chains
18:0	7	
20:0	3	
22:0	11	
24:0	22	
20:4	2	unsaturated chains
24:1	9	
other	40	

Table 5.1
Chainlength and saturation distribution of the cerebrosides extracted from porcine brain used for the experiments described in this chapter of this thesis. *Data taken from www.avantilipids.com.*

an atypical low amount of proteins (approx. 20%) and its main lipid constituents are glycolipids, primarily Cerebrosides [118]. Myelination seems to be very important for nerve impulse propagation, as the velocity of nerve conduction in unmyelinated axons decreases drastically. Bosio et al. have shown that mice deficient in GalCer in the myelin sheaf suffer from whole body tremor and a loss of motor activity [141, 142]. Remarkably, the conduction velocity of the sciatic nerve of the GalCer deficient mice dropped to that of unmyelinated axons [141]. The lack of GalCer leads to an increased fluidity, permeability, and a reduced packing of the myelin lipid bilayer [143]. The mice in [141, 142] lacked the enzyme UDP-galactose:ceramide galactosyltransferase (CGT) that is responsible for GalCer biosynthesis from ceramides. Instead of GalCer, Glucosylceramides (GluCer) are present to a high percentage in the myelin membranes of these knockout mice [141, 142]. Demyelination also occurs in globoid cell leukodystrophy (Krabbe's disease), a hereditary disease that is fatal. However, in the case of Krabbe's disease the reason is paradoxically a deficiency of the enzyme galactosylceramidase that hydrolyses galactosylceramides and galactosphingosine (psychosine). The undegraded GalCers and psychosines accumulate in globoid cells and this finally results in the death of the oligodendroglial cells, the cells that myelinate axons [144–147]. GalCer is also known to be overexpressed on the cellular surface of a variety of cancers. This is explained with the transcriptional repression of the galactocerebrosidase gene that is responsible for degradation of GalCer to ceramides [148]. As ceramides are reported to be apoptosis activators and cerebrosides are reported to be apoptosis inhibitors, an accumulation of GalCer could be responsible for exuberant cell growth observed in cancer tissue [148]. Additionally, GalCer have been reported to be an alternative receptor for a HIV glycoprotein [149].

Galactosylceramides show high melting transition temperatures and have been studied in different model membrane systems [5, 118, 150–152]. The fact that they are in gel phase at physiological temperature suggests that they induce order in membranes [153]. Maggio et al. studied bovine brain GalCer/DPPC lipid mixture membranes with DSC and reported lipid immiscibility from 0 to 46% GalCer percentage [151]. Experiments with synthetic palmitoyl cerebroside mixed with DPPC showed complete miscibility of lipids up to 23% palmitoyl cerebrosides membrane content, at higher content a cerebroside rich phase was observed [154]. The phase diagram of POPC/cerebroside membranes for bovine brain GalCer was explored by Curatolo [118] and shows phase separation over a broad composition and temperature range. Blanchette et al. observed lateral phase separation on DLPC/GalCer giant unilamellar vesicles and planar lipid membranes with fluorescence microscopy and atomic force microscopy [149], respectively. They described that in membranes with 75% DLPC content phase separation is abolished at 12.5% cholesterol incorporation and in membranes with 50% DLPC content phase separation is no longer observed at a cholesterol concentration of 30%. In a recent publication Lin et al. investigated the lateral phase separation pattern for PC lipids/GalCer/chol model membranes with varying degree of saturation of the PC lipids. They found that with increasing degree of saturation phase separation was observable up to a higher cholesterol concentration in the membrane [155]. Cerebroside membranes are accounted to have strong inter-bilayer interactions and may interact also laterally by hydrogen bonding [153, 156]. Depending on the chainlength of the cerebrosides, vesicular and tubular membrane morphologies were observed [153].

In this chapter, the lateral phase behavior of porcine brain cerebroside containing lipid membranes is discussed. POPC, a natural occurring lipid was mixed with cerebrosides in different ratios, as well as with cholesterol. The phase behavior was studied using confocal laser scanning microscopy, two photon laser scanning microscopy, differential scanning calorimetry and Fourier Transform Infrared Spectroscopy. Special emphasis was put on the comparison with the results

on POPC/ceramide/chol mixtures, that were described in the previous chapter (see chapter 4). The aim of this study is to contribute to a detailed knowledge of the lateral phase separation of ceramide and cerebroside containing membranes. This study attempts to broaden the knowledge on the impact of products of the sphingolipid metabolism on lateral phase behavior and is the basis for ongoing studies on lipid species of the sphingolipid metabolism.

5.1 Labeling of POPC/cerebrosides GUVs

The phase state of POPC/GalCer GUVs can be studied by means of fluorescence microscopy using Laurdan. Laurdan shows a shift in emission in the gel phase with respect to the fluid phase (see chapter 3.3.6). In combination with polarized laser light the photoselection effect is observed in gel phase domains located in the top regions of GUVs (see section 3.3.5). These two effects serve the possibility to discriminate gel from fluid domains. Representative GUV pictures for POPC/GalCer vesicles with different mixing ratios are displayed in figures 5.2, 5.3 and 5.4. The red areas in the top row pictures of figure 5.4 stem from fluorescence signal that corresponds to Laurdan relaxation processes in the gel phase, which is also confirmed by the photoselection effect.
The GP values displayed in the lower row of figure 5.4 verify this interpretation. High GP values (red) are detected in the gel phase and low GP values (blue) are found in the fluid phase. Experiments with Dil-C_{18} show that Dil-C_{18} partitions into the fluid phase (see figure 5.2) to a high extend.

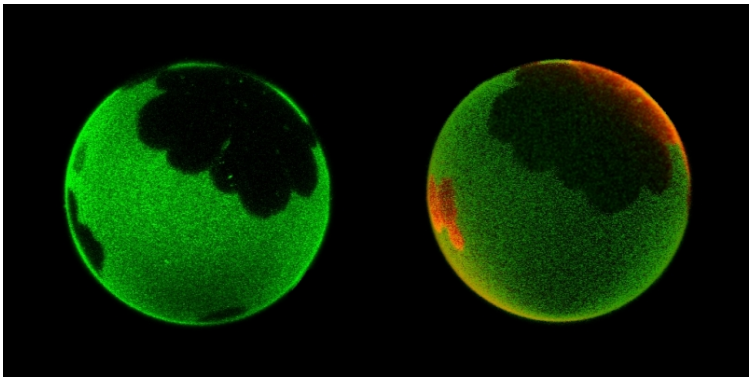

Figure 5.2
Comparison of Dil-C_{18} and Laurdan fluorescence pictures of a POPC/cerebroside 80:20 vesicle. *(left)* Dil-C_{18} partitions in the fluid phase, as can be concluded by comparing with Laurdan fluorescence. *(right)* Laurdan shows emission in the green spectral region corresponding to fluid phase for the areas bright in Dil-C_{18} fluorescence and emission in the blue spectral region for gel phase domains that appear dark in Dil-C_{18} fluorescence (false color interpretation, green is fluid phase, red is gel phase). The vesicle diameter is approximately 30µm.

We noticed that the gel phase in POPC/cerebroside GUVs can also be labeled by adding a small fraction of G_{M1} (0.5 mol %) and a fluorescent labeled cholera toxin B subunit (8µg on 500µl vesicle solution). This is shown in figure 5.3.
Cholera toxin B subunit (CTB) is reported to bind to about five G_{M1} molecules [157]. In order to investigate if this substructure affects the lateral pattern determined on POPC/Cerebrosides

GUVs, an additional fluorescence microscopy experiment was performed. It can be seen that CTB does not affect the lateral domain pattern displayed in POPC/cerebroside GUVs (see figure 5.3).
An additional experiment was conducted to verify whether CTB can bind to GalCer alone, without any G_{M1} present in the membrane. The result was positive. An example is shown in figure 5.3. CTB is labeling the domains depleted of Dil-C_{18}. It seems as if CTB binds specifically to the galactose of G_{M1} and as the headgroup of GalCer consists of a single galactose, CTB binds specifically to GalCer in POPC/GalCer membranes. However, Mertz et al. stated that G_{M1} binding conveys a stabilizing effect to the cholera toxin subunit B, the binding to galactose alone is weaker [158]. From the experiments one can see that G_{M1} was always found in the gel phase and not in the fluid phase of POPC/GalCer GUVs.

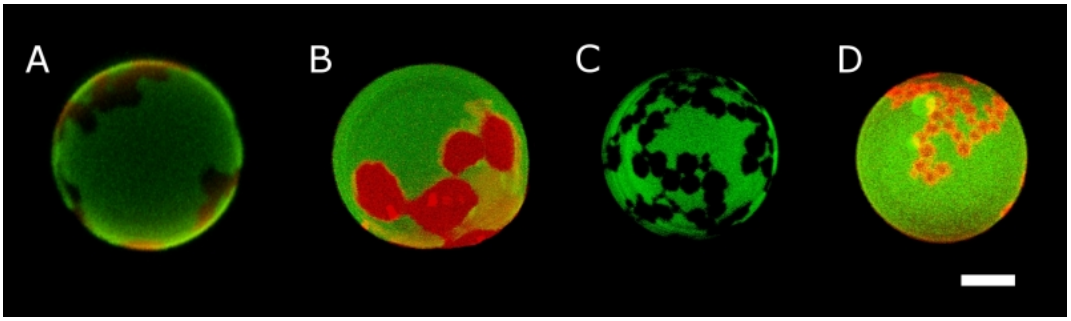

Figure 5.3
G_{M1} in POPC/cerebroside GUVs partitions into gel phase domains preferably and can be labeled with cholera toxin subunit B (CTB). *(A)* Laurdan fluorescence emission showing fluid/gel phase separation in a POPC/cerebroside 80:20 GUV. The fluid phase is indicated in green and the gel phase in red color. *(B)* POPC/cerebroside 70:30 vesicle without G_{M1} but with CTB. CTB binds to the Galactose headgroup of the cerebroside molecules and therefore labels the gel phase. *(C)* POPC/cerebroside 70:30 GUV with G_{M1} incorporated. No CTB is present and the domain shape resembles the domain shape of the vesicle shown in picture B. This indicates that G_{M1} does not affect the lateral pattern in POPC/cerebroside GUVs. *(D)* Vesicle with G_{M1} included and CTB added for labeling. The gel domains depleted in Dil-C_{18} are labeled. The bar corresponds to 10µm.

5.2 POPC/cerebroside mixtures

5.2.1 Confocal and Two Photon Microscopy

The lateral phase separation pattern of POPC membranes with different cerebroside content was investigated with confocal microscopy and two photon microscopy at 20°C, sample pictures are displayed in figure 5.4.
Lateral phase separation into gel (solid ordered) and fluid (fluid disordered) phases in POPC membranes is observed in the whole composition range from 10% GalCer to 90% GalCer.
The area of gel phase increases with growing cerebroside ratio, as can be seen from the top row in figure 5.4. The Laurdan GP values were calculated for each POPC/cerebrosides composition and the results are displayed in figure 5.5. The GP value in the gel phase shows an overall

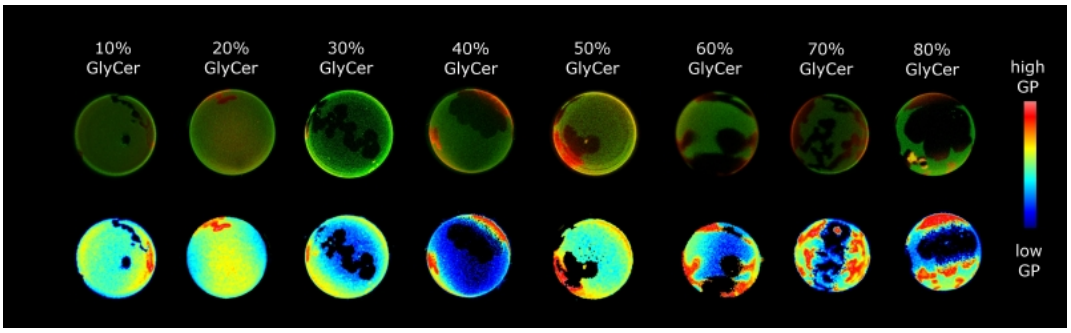

Figure 5.4
Lateral phase separation patterns of POPC membranes with different amounts of cerebrosides at 20°C. *(top row)* Intensity images from Laurdan fluorescence. Green color corresponds to fluid phase domains, red color corresponds to gel phase domains. The photoselection effect is observed in the gel phase. *(bottom row)* The GP values corresponding to the vesicles displayed in the top row. The vesicle diameter is about 20 to 30µm.

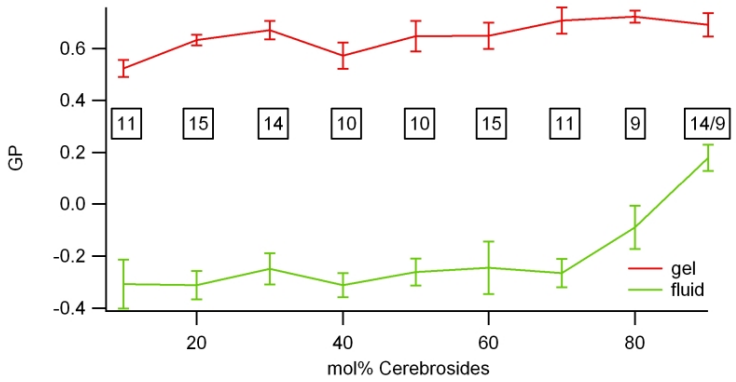

Figure 5.5
Laurdan GP values for POPC/cerebroside vesicles. The GP value in the gel phase (red) shows a small increase with growing amount of cerebrosides, the GP value in the fluid phase (green) stays nearly constant up to 70% cerebroside membrane content and increases at 80% cerebrosides. The numbers in the boxes indicate how many vesicles were averaged to calculate the GP values.

increase from 0.5 to 0.6 as cerebroside membrane content rises. The GP value in the fluid phase stays within error constant to a cerebroside content of up to 70%. At higher cerebroside fractions the GP value grows notably from -0.3 to 0.2. This indicates that the water relaxation processes in the membrane change drastically with more than 80% cerebroside fraction and that the fluid phase obtains a more ordered character.

5.2.2 Calorimetry and FTIR

When a lipid membrane melts, energy has to be supplied in order to increase the rotational degrees of freedom of the carbon chains and to break the lattice structure of the ordered phase.

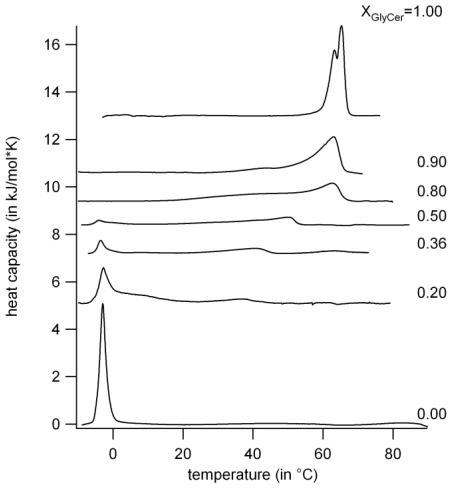

Figure 5.6
Calorimetric scans of POPC/cerebroside mixtures at different mixing ratios as indicated in the figures. By increasing the amount of cerebrosides the low temperature peak corresponding to the POPC rich fluid phase broadens. Above 70 mol % cerebroside content the low temperature peak moves to higher temperatures. The high temperature endotherm of the cerebrosides rich gel phase moves to higher temperatures.

Calorimetry measures this energy in dependence of temperature and thereby provides information about the change in heat capacity and the enthalpy with temperature.
Results from calorimetric scans on membranes composed of POPC/cerebroside mixtures with different mixing ratios are shown in figure 5.6. Pure POPC shows a melting transition from gel to fluid phase at -2.6°C, which is in agreement with previous data [118, 159–161]. With addition of cerebroside a second peak becomes visible in the DSC trace. This second endotherm corresponds to melting events in the cerebroside rich gel phase. The transition enthalpy of the low temperature peak decreases (see table 5.2). However, the peak position does not change in temperature within experimental error up to a cerebroside concentration of 50 mol %. Above 50 mol % cerebroside the peak of the endotherm corresponding to the POPC rich phase shifts dramatically to higher temperatures and its transition enthalpy increases. The peak for the cerebroside rich gel phase moves to higher temperatures and sharpens with a growing amount of cerebroside ratio.
For pure cerebrosides two close peaks are observed in the DSC thermogram, the more pronounced at about 66°C. For the discussion of the results we decided to focus on the more intense peak only. Cerebrosides extracted from bovine brain showed the same melting transition temperature but displayed only one peak [118].
The broadening of the endotherm corresponding to the melting into the POPC rich fluid phase, that is noticed with rising cerebroside concentration, is due to a decrease in cooperativity of POPC molecules in the POPC rich fluid phase. It results from cerebrosides partitioning into that phase, disturbing the ideal interactions of the POPC lipids.
A growing amount of overall cerebroside membrane fraction will increase the fraction of cerebroside molecules in the cerebroside rich phase. This leads to an intensified cooperativity and a sharpening of the peak for the cerebroside rich phase.

The POPC/GalCer phase diagram could be drawn from the calorimetric data. In order to deduce the phase diagram, the peaks of the heat capacity profiles were plotted versus composition. The phase diagram was drawn in this way, as in some cases it was difficult to plot

mol % GalCer	DSC T_{low} [°C]	DSC T_{high} [°C]	DSC ΔH_{low} [kJ/mol]	DSC ΔH_{high} [kJ/mol]
0	-2.6	—	13.4	—
20	-2.7	37.0	3.9	1.4
36	-2.6	38.1	1.9	2.6
50	-3.9	60.5	1.8	0.2
80	34.6	62.8	1.0	4.5
90	42.5	62.5	0.2	10.3
100		65.3	—	15.6

Table 5.2
Transition temperatures and enthalpies of transition of gel and fluid phases of POPC/Cerebroside mixtures calculated from calorimetric experiments.

the exact onset and offset temperatures of phase separation. This is related to the fact that the melting transition regime is very broad. Therefore, an uncertainty in plotting a proper baseline occurs. Fourier Transform Infra Red (FTIR) spectroscopy can also be used to set up the POPC/cerebroside phase diagram. When lipids melt, a change in the area of the CH_2 symmetric and asymmetric stretch vibrational absorption peaks is observed. By plotting the temperatures of highest change in area, the melting temperatures for the solidus and liquidus point can be found. The phase diagram drawn from FTIR experiments is compared to the phase diagram set up from the calorimetric experiments in figure 5.7. The two phase diagrams agree well and also match the phase diagram for POPC and bovine brain cerebroside mixtures published by Curatolo [118]. This may suggest that the general phase behavior of cerebrosides extracted from different species seems to be similar.

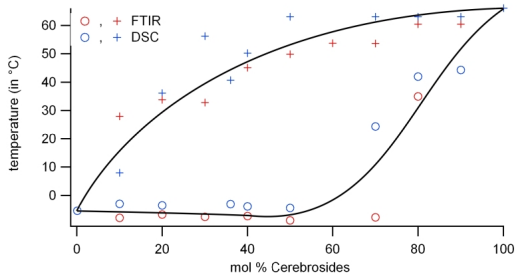

Figure 5.7
The POPC/cerebrosides phase diagram constructed by means of DSC and FTIR. POPC/cerebrosides show phase separation over a broad composition and temperature range.

The melting of the single POPC and cerebroside species in a POPC/cerebroside 80:20 mixture was followed with FTIR spectroscopy by means of a deuterated POPC species (see figure 5.8). The melting of the dPOPC-d31 shows a peak at -4°C in the derivative of the CD_2 asymmetric stretch vibrational peak area change (see section 3.3.8). A shoulder of that peak ranging up to 35°C is observed (lower left graph in figure 5.8). The melting peak of the dPOPC rich areas is observed at a lower temperature compared to the undeuterated POPC lipids because the melting transition of deuterated lipids is lowered in comparison to undeuterated lipids [119, 120]. The shoulder in the derivative of the change in peak area suggests that POPC is also partitioning into the gel phase to a minor fraction and that these POPC molecules melt together with

the cerebrosides moiety.
The change in peak area for the undeuterated lipid chains, the CH_2 symmetric stretch vibrations, displays a small change in wavenumber at about -4°C (upper right graph in figure 5.8), better seen in the peak of the derivative in the lower right graph in figure 5.8. At about 34°C a pronounced melting takes place, also indicated in a broad peak in the derivative of the wavenumber change. The FTIR data is in agreement with the DSC data.

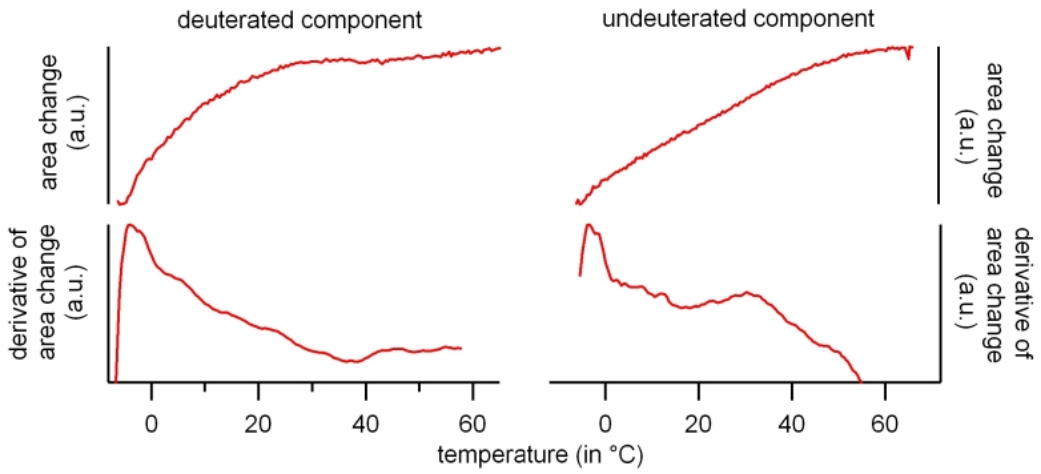

Figure 5.8
Temperature dependence of the melting of dPOPC-d31/cerebrosides 80:20 MLV deduced from the area change of the FTIR spectrum peak at 2920cm^{-1} for the undeuterated lipid chains and at 2195cm^{-1} for the deuterated lipid chains as described in section 3.3.8 and their corresponding derivatives. *(left)* The melting of the deuterated lipid chains of dPOPC-d31. *(right)* The melting of the undeuterated lipid chains.

5.3 POPC/cerebroside mixtures containing cholesterol

5.3.1 Confocal and Two Photon Microscopy

Giant unilamellar vesicles consisting of a POPC/cerebroside 80:20 mixture containing different amounts of cholesterol were investigated with confocal fluorescence laser scanning microscopy (CFLSM) and two photon microscopy (TPM) at 20°C, the results are plotted in figure 5.9.

Phase separation phenomena were observed in a range from 0 to 30 mol % cholesterol (top row in figure 5.9). At 40 mol % the vesicles display one uniform phase only. The domain shape corresponds to that reported for gel/fluid phase coexistence up to a cholesterol concentration of 20 mol % [13].
At 30 mol % cholesterol two fractions of vesicles occurred — one fraction showing the lateral domain pattern comparable to that monitored with lower cholesterol concentrations, the other fraction exhibiting circular domains like those observed in GUVs displaying liquid disordered/liquid ordered phase coexistence [13]. However, in the case of POPC/GalCer/chol membranes no liquid disordered/solid ordered phase coexistence is present at 30 mol % choles-

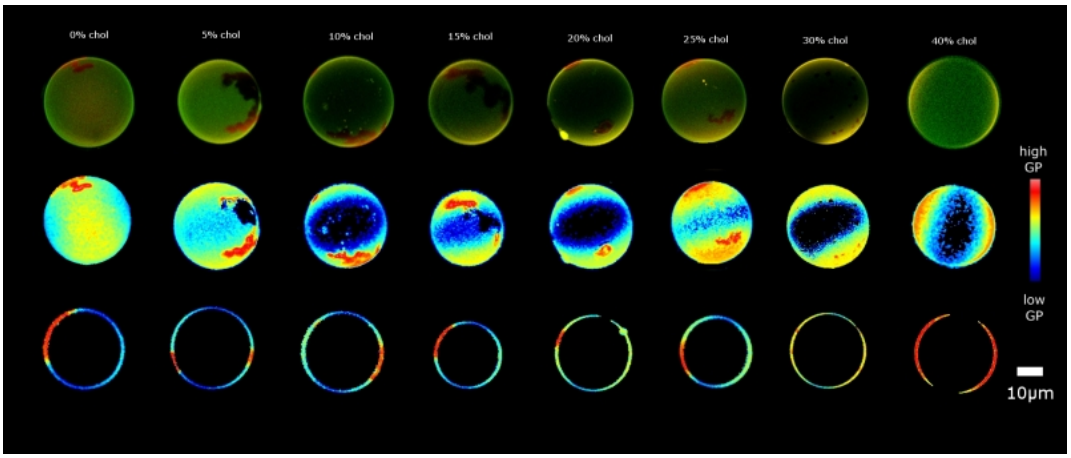

Figure 5.9
GUVs composed of a POPC/cerebroside 80:20 mixture with 0 to 40 mol % cholesterol were investigated with CFLSM and TPM. *(top row)* Laurdan fluorescence from the gel phase (red) and the fluid phase (green). The photoselection effect is observed in the gel phase domains. *(middle row)* Laurdan GP values calculated from the vesicles displayed in the top row. *(bottom row)* Calculated GP values at the cross sections through the equatorial region of the vesicles in the upper rows. An increase of the GP value in the fluid phase is found.

terol fraction. The interpretation of the GP values indicates that the coexistence of two liquid ordered phases is more likely to be present (see below and discussion of this chapter). The Laurdan GP values calculated at the equatorial regions of the vesicles are shown in figure 5.10 and can be visually observed on sample vesicles in the bottom row of figure 5.9.
Up to a cholesterol concentration of 25% the Laurdan GP values for the gel phase stayed at a constant level of about 0.6, corresponding to GP values observed in gel domains of GUVs of other lipid mixtures before [92, 125]. Above 25% cholesterol the GP values drop to 0.45 at 30% and 0.25 at 40 % cholesterol, respectively. This drop in GP values for the gel phase is remarkable, as it indicates an increase in water relaxation processes, comparable to those values corresponding to fluid ordered-like domains.
The GP values in the fluid phase increased from a value of -0.1 with no cholesterol present to 0.2 at 40 mol % cholesterol. A GP value of -0.1 has been reported for fluid phases before [92, 125]. A GP value of 0.2 corresponds to liquid ordered-like phase[1]. The transition from liquid disordered to liquid ordered phase can also be observed by the occurrence of the photoselection effect in the fluid phase. This is displayed in the top row of figure 5.9.

From the Laurdan GP values and the lateral domain pattern deviating from circular shape, we draw the conclusion that POPC/cerebroside 80:20 GUVs with up to 10% cholesterol show fluid/gel phase coexistence. In the regime from 10 to 25 mol % gel/fluid ordered phase

[1] The GP value for the fluid phase is lower than the GP value stated for fluid phases in other publications [92, 125]. This might stem from different filter settings on the microscope, as a control measurement on POPC/ceramide GUVs resulted in the same GP values for gel and fluid phase reported here. They deviate from the GP values obtained in chapter 4, which were produced with another microscope. Different filter settings will result in varying GP values, because the collected intensities deviate (see the definition of the GP function in chapter 3.3.6).

coexistence is present.
As the Laurdan GP value for the solid ordered phase drops to 0.45 at 30 mol % cholesterol, we suggest that two liquid ordered phases with different composition and properties coexist in this regime. This interpretation is also supported by the observed change in the lateral domain pattern to a circular domain shape at 30% cholesterol. With circular domains the boundary length and therefore the free energy is reduced rapidly at high line tensions [13]. The domains of the solid ordered phase are not circular shaped because the lipids display a hexagonal lattice structure.
At 40 mol % cholesterol complete lipid miscibility is reached and one liquid ordered-like phase is present. Of course lateral phase separation could still be present, but if the domain size gets too small, they cannot be resolved due to the resolution limit of the microscope.

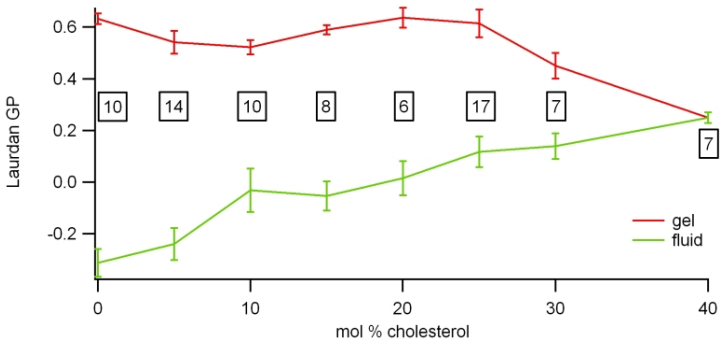

Figure 5.10
GP values calculated at the equatorial regions of GUVs of a POPC/cerebroside 80:20 mixture containing 0 to 40 mol % cholesterol. The numbers in the boxes indicate the number of vesicles averaged for each cholesterol fraction.

5.3.2 Calorimetry and FTIR

The POPC/GalCer 80:20 mixture with different amounts of cholesterol was also studied with DSC. The results are mapped in figure 5.11.
The POPC/ceramide 80:20 mixture without cholesterol shows two main melting events at about -2°C and 30°C. The peak at -2°C belongs to the melting of lipids into the POPC rich fluid phase and the peak at about 30°C belongs to the melting of the cerebroside rich gel phase.
By addition of cholesterol the peak at lower temperatures broadens and shifts to higher temperatures above 10% cholesterol. The peak for the cerebroside rich phase moves to lower temperatures under the influence of cholesterol.
It was not possible to deduce the changes in enthalpy in our experiments. The heat capacity values became too low, so that it was difficult to assign a proper baseline to the experimental data. Small changes in the baseline resulted in pronounced changes in the enthalpy values. Therefore we decided that this data could only be used to extract the melting transition peak positions, but not the changes in enthalpy.

In order to compare the influence of cholesterol to POPC/GalCer mixtures to its influence on the POPC/ceramides mixture that was investigated in chapter 4, FTIR experiments were performed on the POPC/GalCer/chol system. The influence of 26% cholesterol on the melting of the

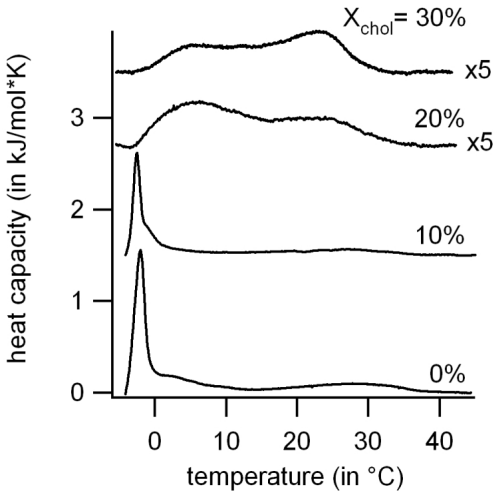

Figure 5.11
Calorimetric scans of a POPC/cerebroside 80:20 mixture with different cholesterol concentrations. The two uppermost traces were multiplied by a factor of five for clarity.

single lipid species in a POPC/cerebroside 80:20 mixture was investigated with a deuterated POPC lipid component in FTIR and compared to a POPC/cerebroside 80:20 mixture without cholesterol (see figure 5.12).

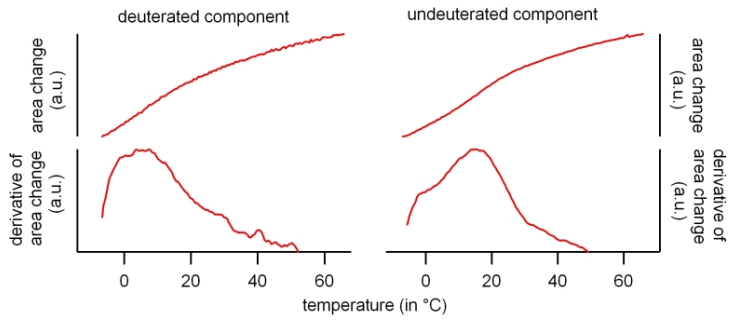

Figure 5.12
FTIR scan on a POPC/cerebroside 80:20 mixture containing 26% cholesterol. *(left)* Change in area of the FTIR spectrum peak at 2195cm^{-1}, corresponding to the deuterated lipid chains of dPOPC-d31. *(right)* Change in area of the FTIR spectrum peak at 2920cm^{-1}, corresponding to the undeuterated lipid chains.

The change in wavenumber for the POPC-d31 component is pronounced at about 5°C but extends up to 30°C, as can be observed in the derivative of the wavenumber change in the left lower graph of figure 5.12. The alteration in wavenumber for the undeuterated lipid chains also takes place over a broad temperature regime from 0°C to about 30°C with an increased change at about 16°C. This is better seen in the derivative of the change in wavenumber in the lower graph on the right hand side of figure 5.12. The peaks observed in the derivatives of the CH_2 antisymmetric and the CD_2 antisymmetric stretch vibrations match with the peaks determined from calorimetry well. The FTIR results demonstrate that POPC and cerebrosides are present in both phases of the cholesterol containing membrane and both lipids melt over a broad temperature regime.

5.4 Discussion

5.4.1 POPC/cerebrosides mixture

All techniques applied within this thesis to investigate the POPC/cerebrosides system show phase separation over a broad temperature regime, as the melting points of the single lipid species are about 60°C away from each other. In many other binary lipid systems such a high separation in melting temperatures of the single lipid species indicates gel phase immiscibility [118, 159, 162] and is reflected by a horizontal solidus line, as seen in figure 5.7 for the POPC/cerebroside mixture. Curatolo [118] also proposed non-ideality in the fluid phase of POPC/cerebroside membranes that might lead to cerebroside clustering in the fluid phase. However, additional micron sized domains besides those reported in the sections before were not observed in our GUV experiments or experiments with a better lateral resolution, such as AFM performed by Blanchette et al. [149].

The onset of the increase in Laurdan GP values with growing cerebrosides molar fraction at 70 mol % GalCer coincides with the onset of a change in melting temperature for the POPC rich phase, as can be seen from comparison of figure 5.5 and the solidus line in figure 5.7. At this point miscibility of POPC and cerebrosides in the POPC rich fluid phase increases and the water dipolar relaxation properties of the fluid phase change, as is evident in the Laurdan GP results in figure 5.5.
The FTIR measurements suggest that POPC molecules are also solved in the cerebroside rich gel phase and that cerebroside molecules reside in the POPC rich fluid phase. This conclusion can be drawn from the broadening of the corresponding melting profiles, too (see figure 5.6). The DSC measurements support this interpretation. DSC shows that the melting peaks corresponding to gel and fluid phase broaden with decreasing amount of their major components.

The heat capacity profile of pure cerebrosides displays two close peaks (see figure 5.6). A second peak was not observed by Curatolo [118] for bovine brain cerebrosides. This might be due to the fact that Curatolo used cerebrosides extracted from bovine brain unlike the porcine brain cerebrosides used for the experiments presented here. This indicates that there are differences in the lipid compositions that make it difficult to compare samples of different origin. Interestingly, the phase diagram constructed from the calorimetric data matches the phase diagram depicted by Curatolo for the bovine brain cerebrosides well, even though porcine brain cerebrosides were used in the framework of this thesis. This demonstrates that the general phase behavior might be similar, but there are slight differences in the molecular details when samples of different origins are compared.

5.4.2 POPC/cerebroside/cholesterol mixture

The discussion of this chapter is also related to the experimental results on POPC/ceramide/chol membranes discussed in the preceding chapter.

POPC/ceramides 83.4:16.6 GUVs display gel- and fluid ordered-like phase coexistence when 10 to 20 mol % cholesterol are solved in the membranes. The same kind of phase coexistence was observed in POPC/cerebrosides 80:20 GUVs with 10 to 25 mol % cholesterol incorporated. With more than 20 mol % cholesterol POPC/ceramide 83.4:16.6 GUVs showed a very peculiar three region pattern (see figure 4.9) with very high GP values present. A three region pattern

does not occur with POPC/GalCer 80:20 GUVs with more than 20 % cholesterol. However, with more than 25 mol % the vesicles composed of this mixture displayed coexistence of two fluid ordered phases (see figure 5.10). This phase coexistence was present up to 40 mol % cholesterol (see figure 5.9). However, it could still be present in domains smaller in size than the microscopes resolution with even higher cholesterol concentrations. At a certain cholesterol concentration complete miscibility is reached and for POPC/GalCer 80:20 GUVs this point seems to be at 40 % or above.

The difference in the lateral patterns observed for POPC/ceramides/cholesterol and POPC/GalCer/cholesterol GUVs might originate from their different headgroup structure, as the experimental conditions were the same. Several publications report that ceramides displace cholesterol from ordered bilayers [114, 163]. Ali et al. [163] state that ceramides have a higher affinity to ordered bilayers than cholesterol and that both molecules have very small polar headgroups compared to their nonpolar bodies. To prevent the exposure of the hydrophobic bodies to the surrounding water, Ceramides and cholesterol try to cover their small headgroups by the headgroups of the neighboring lipids, which is explained by the umbrella model [16].
The umbrella model might explain our observation of gel / liquid ordered phase coexistence for POPC/ceramide/chol GUVs. Ceramides and cholesterol have a strong ordering effect on lipid bilayers. However, cholesterol is displaced from the gel phase by ceramides [114, 163]. The cholesterol accumulating in the fluid phase might induce a liquid ordered-like phase then, and the gel phase is preserved.
In contrast, cerebrosides have a galactose headgroup that is bulky compared to the ceramide headgroup. The high melting temperature of cerebrosides is reported to stem from the strong hydrogen bonding capability of the amid backbone region and the galactose ring of the headgroup [164], that stabilize the membrane through hydrogen bonding networks. In the case of cerebrosides cholesterol can use the GalCer headgroups to shield its nonpolar body from water [16]. There is no competition as with ceramides. However, cholesterol is present in both phases and has an ordering effect on the fluid phase, which is also reported by Ali et al. [165]. Up to 25 mol % cholesterol membrane content the gel phase is not affected, but at higher cholesterol concentration a decrease in GP value is observed, indicating a disordering effect of increasing cholesterol fraction. This might be due to defects in the cerebroside hydrogen network induced by the presence of cholesterol.

The impact of saturation of the hydrocarbon chains of PC lipids on the lateral domain pattern in POPC/GalCer/chol system has been investigated by Lin [155] et al. recently. In their experiments phase separation was only observed up to 17.5 % cholesterol content. However, there are two issues that can explain the discrepancy between the results reported by Lin and within this thesis:

1. The lipids used by Lin et al. were purchased at a different company and usually lipids from different companies differ in phase behavior, which can be seen in DSC experiments for example (personal communication with Thomas Heimburg and Luis Bagatolli). The reason for this effect might be different sample purities.

2. The miscibility of the fluorescent probe NBD-PC used by Lin et al. might be changed by the cholesterol effect on the membranes, so that it distributed equally in the membrane, even though liquid ordered/liquid ordered phase separation was present. Probably NBD-PC is not sensitive to this case. A similar observation was done by the application of the fluorescent probe DiI-C_{18}. In POPC/GalCer membranes with no cholesterol

incorporated, the partitioning of the probe into the fluid phase domains was very clear, but with a growing amount of cholesterol the partition of Dil-C_{18} into the GalCer rich phase increased and it was difficult to observe phase separation at 20 mol % cholesterol or higher. However, pictures with Laurdan GP values and cholera toxin B subunit that binds to G_{M1} molecules present in the gel phase still show phase separation (see figure 5.13).

In their publication Lin et al. [155] also stated that they could not resolve liquid ordered domains with AFM in POPC/GalCer mixtures with more than 17.5 % cholesterol, because the liquid ordered domains were getting too soft. However, it is also possible that the height difference between the two liquid ordered phases became too small to be followed with AFM. When the solid ordered phase gets fluid ordered-like its thickness might decrease and the thickness of the liquid disordered phase increases as it becomes more liquid ordered-like. Therefore the height difference between both phases will decrease and will not be detectable at a certain point.

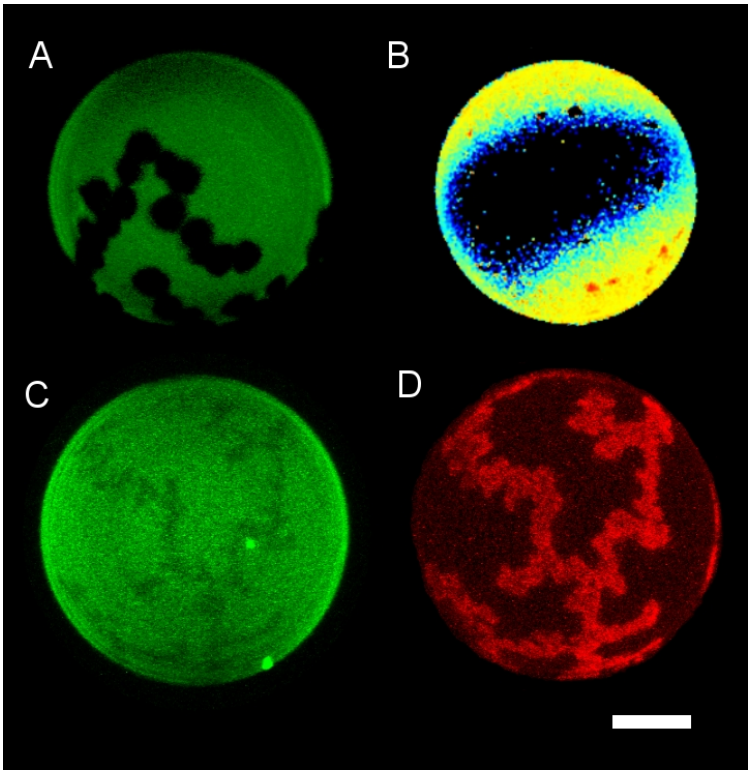

Figure 5.13
Comparison of fluorescence signal. *(A)* Dil-C_{18} in a POPC/GalCer 70:30 GUV; *(B)* Laurdan GP values of a POPC/GalCer 80:20 + 30% chol GUV, *(C)* Dil-C_{18} in a POPC/GalCer 80:20 + 30% chol GUV; *(D)* Cholera toxin B subunit labeled G_{M1} in the same vesicle as C. The bar corresponds to 10µm.

All in all, we conclude that in the region from 25 mol % to 40 mol % cholesterol concentration a transition regime from gel to liquid ordered phase is present for the cerebroside rich phase. Under the impact of cholesterol, the GP value for the gel phase decreases and the GP value for the fluid phase increases until a homogeneous lipid mixture is present at 40 mol % cholesterol, displaying a unique Laurdan GP value. The presence of cholesterol decreases the unfavorable interactions of POPC and cerebrosides molecules until complete lipid miscibility is reached.

5.5 Outlook

Within the last two chapters new insights into the lateral structure of Ceramide and Cerebroside containing membranes were presented. These two lipid species used determine only the beginning of a series of studies on sphingolipid containing membranes. In the future we plan to examine Gangliosides that are reported to have a positive effect in neural regeneration and are assumed to have great potential in treatment of Alzheimer's disease and Parkinson's disease, for example [166, 167].

Another very interesting study would be on membrane models using synthesized ceramides, cerebrosides and sphingomyelin. Avanti Polar Lipids recently introduced synthesized C_{12}-cerebrosides. Synthetic C_{12}-ceramides and C_{12}-sphingomyelin has been available for a while and so it would be interesting to study these in POPC/cholesterol model systems, because then changes in lateral structure and phase behavior should be due to the different headgroups, as the rest of the systems is equal.
An interesting fact is that for the POPC/cerebroside 80:20 system the transition from gel/fluid ordered phase coexistence to fluid ordered/fluid ordered phase coexistence is at about 25 mol % cholesterol fraction, which is close to cholesterol concentrations found in many natural tissues. By changing the cholesterol concentration in the membrane, it would be possible to trigger this phase transition and therewith presumably some membrane function. This idea is probably far-fetched, but should be considered in future experiments.
Phase coexistence has recently been reported from natural lipids extracted from human stratum corneum [168]. It would be interesting to investigate the lateral domain pattern in terms of GP experiments to see whether it resembles the phase coexistence behavior observed for the POPC/ceramides/chol mixture.

Chapter 6

Melting of single lipid components in binary lipid mixtures

The two preceding chapters concentrated on the lateral patterns observed in model membranes composed of synthetic POPC lipids and extracted ceramides and cerebrosides from porcine brain with and without cholesterol. In these cases lateral phase separation into domains was observed over a broad temperature and composition range. The lipid mixtures used were not real binary or ternary lipid mixtures as the extracted ceramides and cerebrosides display a variety in chain length and saturation. Even for the more complex bacterial membranes, consisting of up to 500 different lipid species or more, all of them having different chemical and physical properties, phase coexistence was detected by means of calorimetry [18, 19, 23].
The reason for the big variety in lipid species has not been answered until now. It has been shown for many different bacteria that the lipid synthesis depends on outer parameters, such as growth temperature for example [169–172].
The membrane composition of bacteria of the same species that grow at higher temperatures contains more saturated lipids and lipids with longer chains [172]. This adaption has an influence on the physical behavior of a biological membrane, such as phase separation. In single component lipid membranes a higher degree of saturation or longer fatty acid chains result in higher melting temperatures [6].
In the past, a hypothesis for the adaption of lipid synthesis in respect with growth temperature was that it ensures a necessary "fluidity" of the membrane [172]. The term "fluidity" is related to an ease of movement in this case. However, arguments against a role of fluidity were presented [173]. A second possibility is to ensure a control of the heterogeneity of the lateral membrane structure [174]. This idea has obtained much attention following the discussion about lipid "rafts" [175].

Artificial systems consisting of one, two or three lipid components are suitable systems to study the general physical behavior of lipid phase transitions in more complex lipid systems. In the phase coexistence regime, domains with a size ranging from a few nanometers to several micrometers, form in model systems and can be observed by a large variety of experimental techniques, for example Fluorescence Resonance Transfer, Atomic Force Microscopy and Confocal Fluorescence microscopy [28, 29, 54].

Already in the early 1970s the idea that domain formation processes display a role in protein

activity and function was formulated [174, 176, 177]. In several publications domains formation has been shown to provide a mechanism to control biochemical reaction cascades [49–51, 178]. Consequently, lipid phase transitions are not to be underestimated: Lichtenberg et al. [31] showed that Phospholipase A_2 activation is fastest in the phase transition regime and that lipid hydrolysis is highest at short activation times. The activity of the phospholipase A_2 type IIA has been shown to be related to an enrichment of anionic lipids into fluid domains [131]. Changes of the opening times and probabilities of calcium channels reconstituted into POPE/POPC membranes have been interpreted as being due to gel/fluid phase coexistence [179]. In some of the above cited publications the concentration of a single lipid species within one phase seems to be important, as a threshold concentration value has to be exceeded to induce enzyme activity [131].
A further example is the protein kinase C (PKC) which modifies proteins by chemically adding phosphate groups. It has been discussed that lateral heterogeneities of the lipid membrane controls the activation of this enzyme [180, 181]. In the latter study it has also been pointed out that domains enriched in dioleoylglycerol lipids play a crucial role, but also a linear relationship between PKC activity and phosphatidylserine content has been found [182]. Further communications can be found where a connection between enzyme activity and the presence of special lipids and structure are made. This is e.g. the case for the calcium ATPase [183].
The publications cited above are only a small fraction of many in that respect, but they already show that it is interesting not only to study domain formation, but also to investigate the fraction of the single lipid species in lipid membranes showing lateral inhomogeneity due to phase separation. The single lipid species will occur in different amounts in the different domains that form in phase transition regime [52]. The work presented here concentrates on this for the case of a binary lipid mixture composed of DMPC and DSPC.

Monte Carlo simulations analyzing simple models of lipid chain melting describe lipid membrane properties in the vicinity of lipid phase transitions well, such as changes in membrane permeability , fluctuations in enthalpy and diffusion processes. In this chapter the amount of the single lipid species in the different domains of binary DMPC and DSPC mixtures is explored by means of Monte Carlo simulations and the results are compared to experimental results obtained by FTIR[1]. It is shown that in FTIR spectroscopy the melting of the single lipid species of binary lipid mixtures cannot be investigated precisely by following the shift in wavenumber for the CH_2 vibrational bands, as has been done by Leidy et al. before [97]. A new method for data evaluation will be introduced that shows that the results obtained with Monte Carlo simulations match the FTIR experiments well.
Among other techniques FTIR is well suited to investigate the melting behavior of lipid membranes. In these studies the temperature dependence of various vibrational bands due to structural changes of the lipids provide a versatile tool in following phase transitions [184–187]. Articles have been published on work in which FTIR was used to measure nanoscale domain size [188] and chain order parameters [189].
Here, for the FTIR spectroscopy experiments a deuterated DMPC lipid dDMPC-d54 was used. In dDMPC-d54 the hydrogen atoms of the lipid chains are replaced by deuterium atoms and therefore the change in the symmetric and antisymmetric stretch vibrational bands with temperature of DMPC and DSPC can be investigated independently. The frequency of the vibrational bands of the dDMPC-d54 lipids shifts in respect to the vibrational bands of the undeuterated DSPC lipids.

[1] The Monte Carlo simulations for this study were performed by H. Seeger.

$T_{m,1}$	= 19.7 °C	ω_{11}^{od}	= 1267 J/mol
$T_{m,2}$	= 54.8 °C	ω_{22}^{od}	= 1474 J/mol
ΔH_1	= 14500 J/mol	ω_{12}^{oo}	= 607 J/mol
ΔS_1	= 49.5 J/(mol·°C)	ω_{12}^{dd}	= 251 J/mol
ΔH_2	= 25370 J/mol	ω_{12}^{od}	= 1548 J/mol
ΔS_2	= 77.4 J/(mol·°C)	ω_{12}^{do}	= 1716 J/mol

Table 6.1
Parameter values used in the Monte Carlo simulations. They were assigned from calorimetric heat capacity profiles [67]. All numbers are given per lipid chain. The indices *o* and *d* stand for *ordered* and *disordered*, respectively and *1* and *2* for *dDMPC-d54* and *DSPC*, correspondingly.

6.1 FTIR spectroscopy and MC simulation results

As described in section 2.2.2, ten parameters have to be determined for the simulations of binary lipid mixtures by means of Monte Carlo simulations. The DMPC/DSPC system with two undeuterated lipid species was investigated before [67, 68] and seven of the ten parameters were adopted from this study, based on the assumption that the unlike nearest neighbor interaction parameters do not alter by switching to a deuterated lipid species.

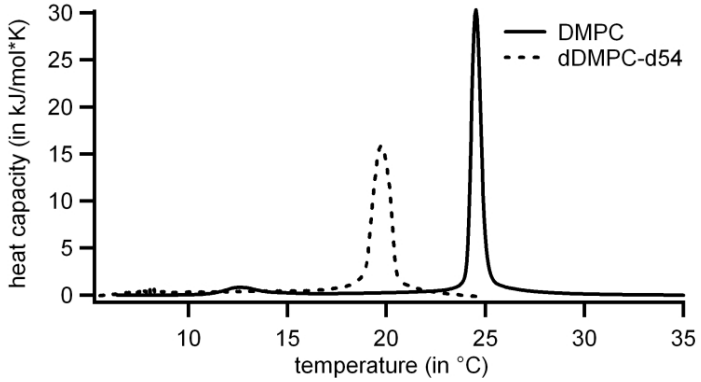

Figure 6.1
Calorimetric scans on MLV composed of dDMPC-d54 and DMPC. The melting transition for dDMPC-d54 is broadened and shifted for about 5°C to lower temperatures compared to DMPC.

Only three parameters had to be reestablished for this study, namely the enthalpy and entropy change ΔS and ΔH during the transition and the gel-fluid interaction parameter $\omega_{dDMPC-d54}^{od}$ of the dDMPC-d54. These values were obtained from a calorimetric scan on pure dDMPC-d54 MLVs and matching the corresponding Monte Carlo simulation to the experimental heat capacity profile by changing the value of the interaction parameter $\omega_{dDMPC-d54}^{od}$. The melting transition of pure dDMPC-d54 is shifted to lower temperatures by about 3.9°C and broadened in comparison to undeuterated DMPC [119, 120](see also figure 6.1). The simulated results obtained with the reestablished parameters match the calorimetric data well, as can be seen from figure 6.2. The parameters used for the simulation can be found in table 6.1.
After the parameters for the MC simulations were set, dDMPC-d54/DSPC lipid mixtures with different mixing rations were simulated. The results are displayed in figure 6.3

6.1.1 MC Simulations and FTIR experiments: Analysis of the absorption maxima

In FTIR spectroscopy the absorption of infrared light due to rotational degrees of freedom in the sample is studied. In lipid suspensions different vibrational modes contribute to the absorption

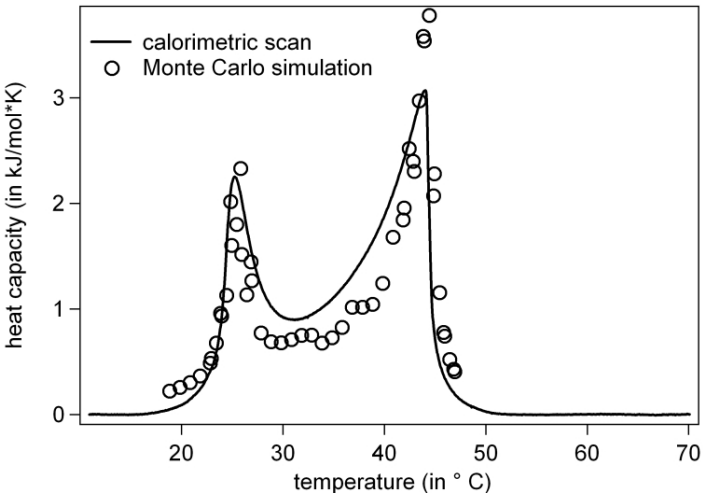

Figure 6.2
Comparison of a measured and a simulated heat capacity profile of a dDMPC-d54/DSPC 50:50 lipid mixture. The curves agree well and justify the assumption that the unlike nearest neighbor interaction parameters for a deuterated and an undeuterated DMPC/DSPC lipid system do not change.

spectra [185, 187]. In this study we focus on the CH_2 symmetric (at 2850cm^{-1}) and asymmetric stretch (at 2920cm^{-1}) absorption peaks of DMPC/DSPC lipid mixtures. The peak positions of these vibrational modes change to higher wavenumbers with increasing temperature. By application of a DMPC lipid species with perdeuterated alkyl chains the lipid melting of both lipid species could be monitored independently [97]. Due to the heavier deuterium atoms the CH_2 vibrational modes were shifted to lower wavenumbers (2090cm^{-1} for the CH_2 symmetric and 2190cm^{-1} for the CD_2 asymmetric stretch modes, respectively).
Representative results showing the shift of the peak position with temperature for dDMPC-d54/DSPC 70:30 and dDMPC-d54/DSPC 30:70 mixtures are displayed in figure 6.3 A and B, respectively. In the same figure, the results are compared to the simulated fractions of ordered and disordered lipids of the same lipid mixtures.
The left panel in figure 6.3 shows the melting events for the dDMPC-d54 lipid species. The solid lines display the change of wavenumber versus temperature and the open circles represent the calculated fraction of disordered dDMPC-d45 lipids versus temperature. The experimental and simulated results match well. The most pronounced change in wavenumber and in disordered chain ratio was observed at about 24°C for dDMPC-d54/DSPC 70:30 and at about 31°C for the dDMPC-d54/DSPC 30:70 mixture.
The right panel in figure 6.3 depicts the melting events for the DSPC lipid species. The dashed lines give the change of wavenumber versus temperature and the open squares show the calculated fraction of disordered DSPC lipids versus temperature. Obviously, the experimental results and the simulations deviate strongly, more distinct in the case of dDMPC-d45/DSPC 70:30. Whereas the simulations display an increase in disordered chain ratio starting at 20°C, with a maximum increase at about 38°C, the wavenumbers start to drop from about 20°C, reaching a minimum at 28°C and then increase to match the simulated results at higher temperatures.
The discrepancy becomes clearer by calculating the derivations of the profiles (see figure 6.4). The derivatives for the deuterated lipid species match the derivative of the disordered chain ratio of DMPC from the monte carlo simulations well, both displaying a maximum at about 24°C. In contrast, the derivative of the change in wavenumber obtained from FTIR experiments for the undeuterated component shows a drop with a local minimum at 24°C, whereas the derivative of the MC simulation results shows a local maximum at this temperature. The maximum indicates an enhanced melting of the DSPC lipids, whereas the minimum in the derivative of

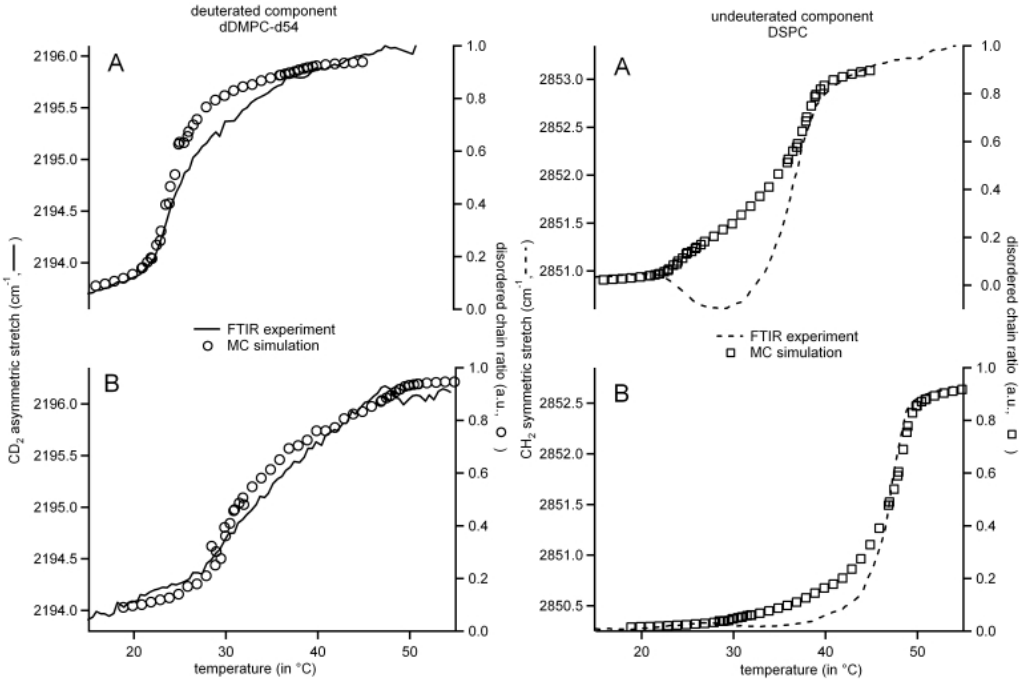

Figure 6.3
Comparison of single component melting of dDMPC-d54/DSPC lipid mixtures followed by FTIR and simulated by MC simulations. The FTIR data were obtained by following the shift in wavenumber with temperature as explained in section 3.3.8. (*A*) dDMPC-d54/DSPC 30:70, (*B*) dDMPC-d54/DSPC 70:30. The left panel shows the melting of the deuterated component (experiment —, simulation(○)), the right panel shows the melting of the undeuterated component (experiment (- - -), simulation (□)).

the change in wavenumber was interpreted as a condensing of the DSPC lipids, induced by the melting of the DMPC lipids by Leidy et al. [97]. The two results contradict each other.
Leidy et al. [97] explained this drop in wavenumber by a higher packing of the DSPC lipids, induced by the melting of the dDMPC-d54 lipids. However, another possible explanation is an overlap of close-by peaks, as explained in section 3.3.8. To investigate this possibility, the FTIR data evaluation method was changed to follow the change in peak area of the CH_2 and CD_2 stretch vibrations (see section 3.3.8 for details).

6.1.2 Difference spectra method

In an investigation of structural changes in cytochrome c, Heimburg and Marsh evaluated the temperature dependent changes of difference spectra [190]. This was motivated by the idea that the corresponding amide I band contains a variety of different bands and the absorption of the single bands change differently with temperature. This results in a change of the shape of the whole band. This section investigates if this effect also occurs for the absorption bands of the CH_2 and CD_2 stretch vibrations. If the spectrum consists of a convolution of several peaks for ordered and disordered lipids, a change in temperature will affect the ratio between

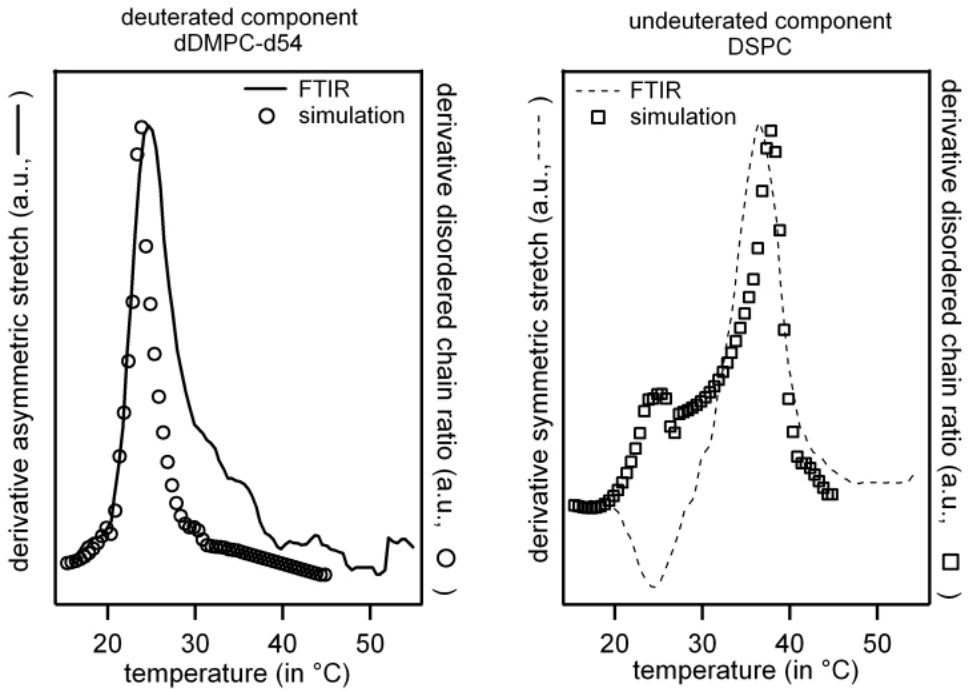

Figure 6.4
Derivation of the traces in figure 6.3 A from a dDMPC-d54/DSPC 70:30 sample. The left hand panel shows the results for the deuterated lipid species (change in wavenumber (—), change in peak area (○)). The right hand panel shows the results for the undeuterated lipid species (change in wavenumber (—), change in peak area (□)). The results for the undeuterated lipid species differ clearly.

the single bands and a shift in the position of the convoluted peak might be observed that does not necessarily correlate with a condensation of a lipid species as interpreted by Leidy et al [97]. With the difference spectra method the change in peak area of the CH_2 and CD_2 symmetric and the asymmetric vibrational bands was followed with temperature. Difference spectra for several temperatures are shown in figure 6.5.

The result obtained with the difference spectra method can be seen for a representative data set of a dDMPC-d54/DSPC 70:30 sample in figure 6.6.

The left hand panel shows the comparison of data sets obtained from the difference spectra method and by monitoring the shift of the peak position of the CH_2 symmetric and the CD_2 asymmetric absorption bands for the deuterated component. Both curves match well. On the right hand panel the undeuterated species were evaluated with both methods. The two curves show opposite behavior at about 24°C: While the curve obtained by following the peak position of the CD_2 asymmetric stretch vibration resulted in a decrease in wavenumber, the curve obtained by the difference spectra method increases in the same temperature regime. Interestingly, the position of the minimum in the case of the wavenumber change agrees with the local maximum in the data obtained with the difference spectra method. At higher tem-

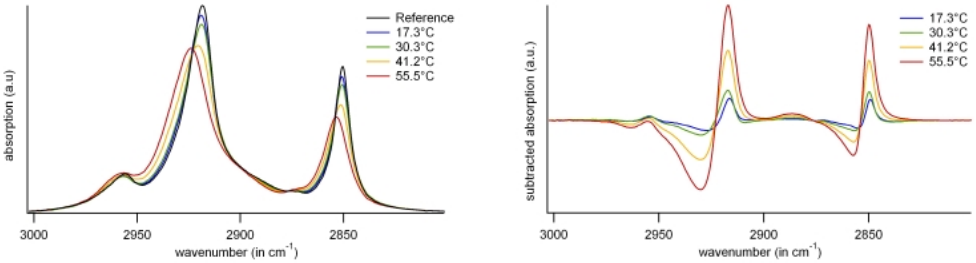

Figure 6.5
The left hand panel shows the spectra of the CH_2 symmetric (at 2850cm^{-1}) and asymmetric (at 2920cm^{-1}) vibrational bands at different temperatures. The left hand panel shows the corresponding difference spectra.

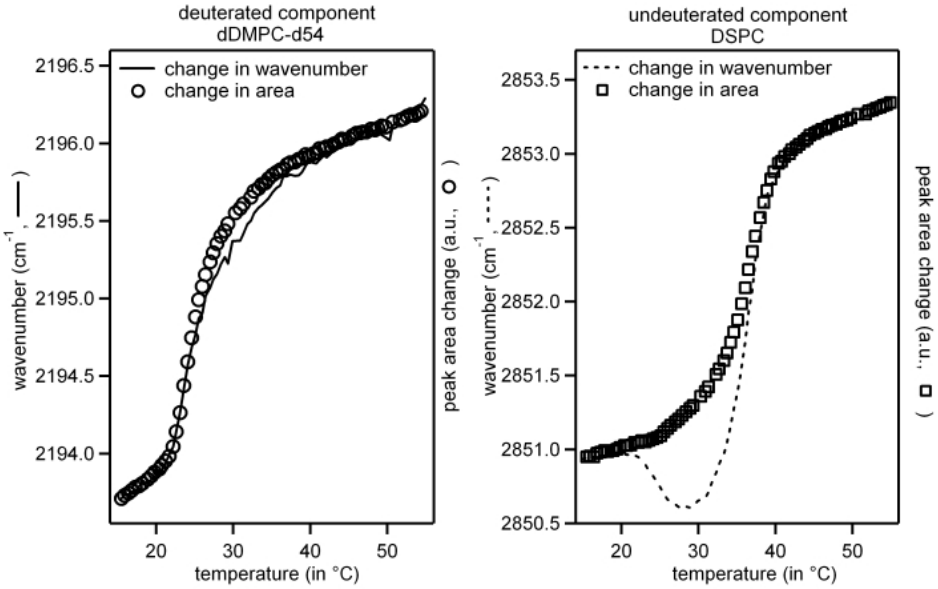

Figure 6.6
Comparison of results obtained with two different FTIR data analysis procedures. The data displayed was obtained from a dDMPC-d54/DSPC 70:30 sample. The left hand panel shows the results for the deuterated lipid species (change in wavenumber (—), change in peak area (○)). The right hand panel shows the results for the undeuterated lipid species (change in wavenumber (—), change in peak area (□)). The results for the undeuterated lipid species differ clearly.

peratures both curves meet and show the same progression with increasing temperature.

The course of the data acquired from the difference spectra method agrees with the development of the simulated ordered and disordered chain ratios from figure 6.3. Figure 6.7 compares both methods directly for different lipid mixing ratios. All data sets match well.
The melting of the deuterated lipid component is plotted in the left hand panel of figure 6.7.

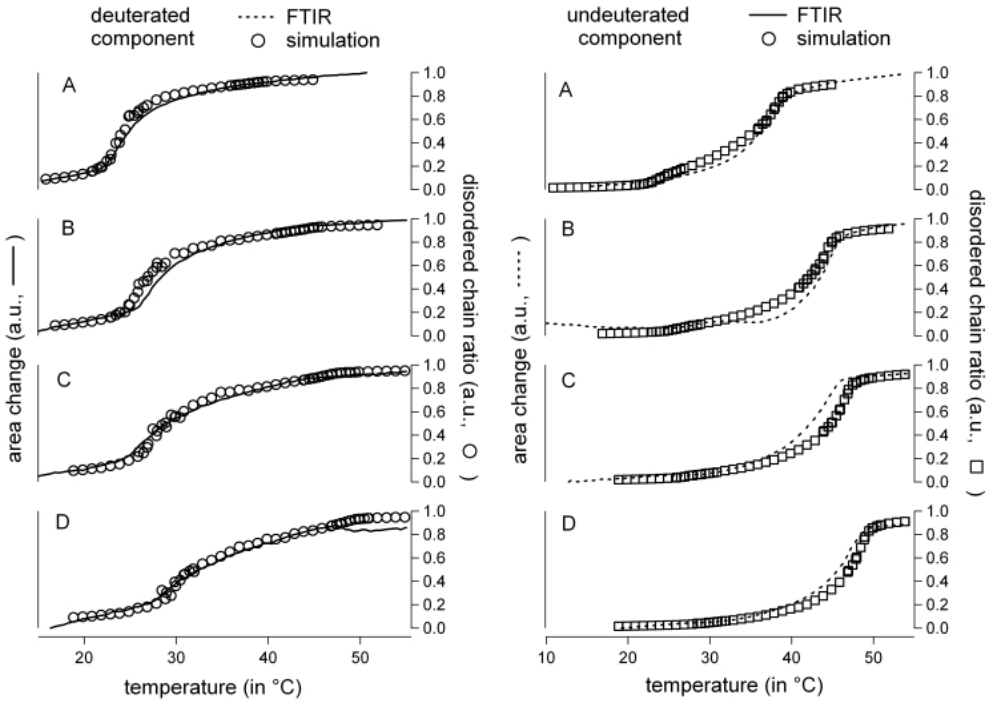

Figure 6.7
Comparison of experimental results obtained from FTIR data by analyzing the change in peak area of the CH_2 and CD_2 vibrational stretch vibrations with Monte Carlo simulation results. The data displayed were obtained from dDMPC-d54/DSPC mixing ratios of (*A*) 70:30 (*B*) 50:50 (*C*) 40:60 (*D*) 30:70. The left hand panel shows the results for the deuterated lipid species (change in peak area (—), change in disordered chain ratio (∘)). The right hand panel shows the results for the undeuterated lipid species (change in peak area (- - -), change in disordered chain ratio (□)). The results match well.

The melting of the undeuterated lipid component is shown in the right hand panel of figure 6.7. To highlight the details of the melting curves, the derivatives for the two lipid mixing fractions dDMPC/DSPC 70:30 and 40:60 were calculated and are displayed in figure 6.8 A and B respectively.

In the left hand panel of figure 6.8 the derivatives are plotted for dDMPC-d54. The greatest change in the difference spectra and in the simulated chain melting takes place at 24°C for 70 mol % dDMPC-54 and at 27°C for 40 mol % dDMPC-d54. The peak positions of the experimental and the simulated data match well. From both graphs it can be seen that the dDMPC-d54 lipids display melting events up to 40°C and 50°C, respectively, demonstrating that the dDMPC-d54 lipids are also present in the DSPC rich solid ordered phase and melt together with the DSPC lipids.
The melting of the undeuterated DSPC lipids is printed in the right hand panel of figure 6.8. All curves show the same qualitative behavior, except for a shift of the peak of the DSPC melting for about 2°C to higher temperatures for the simulated traces compared to the experimental traces. In addition to the peak at about 38°C, the melting profile for the DSPC lipids in the

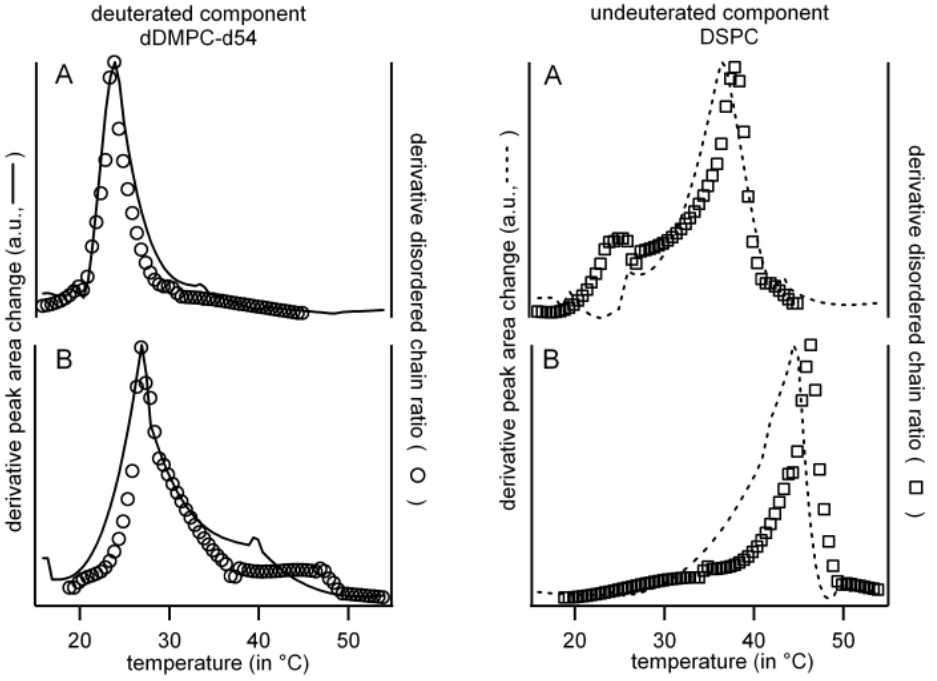

Figure 6.8
Comparison of experimental results obtained from FTIR data by analyzing the derivatives of the change in peak area of the CH_2 and CD_2 vibrational stretch vibrations with Monte Carlo simulation results. The data displayed was obtained from dDMPC-d54/DSPC mixing ratios of (*A*) 70:30 and (*B*) 40:60. The left hand panel shows the results for the deuterated lipid species (change in peak area (—), change in disordered chain ratio (○)). The right hand panel shows the results for the undeuterated lipid species (change in peak area (- - -), change in disordered chain ratio (□)). The results match well.

dDMPC-d54/DSPC 70:30 lipid mixture displays a local maximum at 24°C. This is exactly the temperature at which the dDMPC-d54 lipids have their maximum in melting. This means that a minor fraction of DSPC lipids melts together with the major fraction of the dDMPC-d54 lipids into the dDMPC-d54-rich liquid disordered phase. This local maximum is not observed with all lipid mixing ratios but with all mixtures having more than 30 mol % DSPC.
With increasing dDMPC-d54 fraction from figure 6.7A to D the maximum in change of the difference spectra shifts to higher temperatures, from about 24°C in figure 6.7 to about 28°C in figure 6.7 D.

6.1.3 The phase diagram

Phase diagrams are generally constructed to easily assess the phase separation behavior of lipid mixtures [52]. In our case, a phase diagram was constructed with dependence on composition and temperature (figure 6.9). A phenomenological method to construct phase diagrams is in aligning tangent on the lower and upper slopes of the temperature limits of a heat capacity

profile. The data from the lower temperature limits gives the solidus line, whereas the data from the upper temperature limits defines the liquidus line. In the case of ideal lipid mixtures that do not show phase separation into two solid phases, the lipid membrane is in the solid ordered phase below the solidus line and in the liquid disordered phase above the liquidus line. In the region between solidus and liquidus line liquid disordered / solid ordered phase coexistence is present. If the lipid composition is known, the physical state of the membrane can be derived easily from the phase diagram.

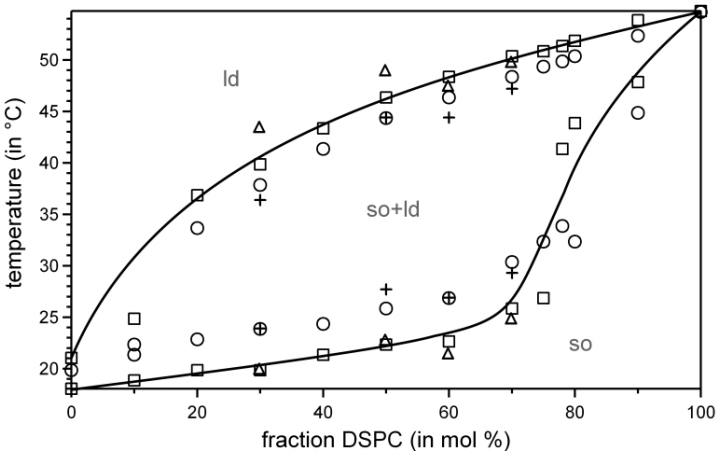

Figure 6.9
dDMPC-d54/DSPC Phase diagram obtained from plotting the initiation and completion temperatures from MC simulations (□) and FTIR (△). The peak positions obtained from the derivative of the change in disordered chain ratio from Monte Carlo simulations (o) and the peak positions of the derivatives of the area change of the FTIR spectra (+) are also included.

In figure 6.9 the boundaries of the phase diagram were drawn to match the solidus and liquidus temperatures assigned from Monte Carlo simulations in order to guide the eyes. The phase boundaries derived from Monte Carlo simulations match those obtained by calorimetry and FTIR well [67]. However, at 30 and 50 mol % DSPC the solidus points line are slightly shifted to higher temperature. This might be due to the temperature calibration, as is explained in the discussion section of this chapter. The peak positions of the melting profiles of the disordered chain rations from Monte Carlo simulations are also drawn in figure 6.9. The peak positions appointed from the derivative of the difference spectra peak area change match these peaks well.

6.2 Discussion

In this chapter a combined FTIR and MC simulations study was presented. FTIR absorption spectra were analyzed with two methods: One method followed the temperature dependence of the absorption maximum of the CH_2 and CD_2 stretch vibrational bands and the other method followed the temperature dependent changes of the area of the difference spectra. The first method shows a drop in wavenumber for the DSPC lipids when the dDMPC-d54 display pronounced melting, with the other method an enhanced melting is obtained when the dDMPC-d54 lipid melting is maximal (see figure 6.6). The decrease in wavenumber was interpreted as a condensing of the DSPC lipids, induced by the melting of the dDMPC-d54 lipids by Leidy et al. [97]. To our knowledge, no other experimental evidence to support this idea has so far been published. On the contrary, Mendelsohn et al. investigated the binary mixture PS/dDPPC-d62 30:70 and did not observe any decrease in wavenumber [191, 192]. Additionally, if the data is

analyzed with the other approach, namely the difference spectra method, an enhanced melting of the DSPC lipids was observed in this temperature range (see figure 6.8). This enhanced melting was also found in Monte Carlo simulations (see figure 6.4). These have proven to model the phase behavior of binary lipid mixtures adequately and there is no reason why they should fail in this case. Of course, one might argue that sterical interactions and van der Waals interactions are not included in Monte Carlo simulations and therefore Monte Carlo simulations might not show the condensing of the DSPC lipids here. Additionally, the model used here is based on a hexagonal lattice for both phases, but this is actually only true for the solid ordered phase. To rule out these arguments completely more sophisticated simulation techniques have to be applied to the system, for example Molecular Dynamics (MD) simulations or off-lattice simulations. However, the timescale of MD simulations is still too short to date to make this investigation possible.
In our opinion the identity of the difference spectra method and the Monte Carlo simulations makes us confident that investigation of the change in wavenumber is not sufficient to follow single component melting in lipid mixtures and that the difference spectra method has to be applied instead.
It seems that in the case of a pure single lipid system the change in wavenumber can be followed to investigate melting processes in lipid membranes, but if the lipid system is expanded to lipid mixtures this method might fail. The CH_2 and CD_2 absorption regions in the FTIR spectrum consist of a convolution of several bands and the intensities of these bands change differently with temperature. This might lead to the apparent decrease in the wavenumbers of the CH_2 and CD_2 absorption peaks, even though the lipids show enhanced melting in reality.

Our assumption that by exchanging DMPC with dDMPC-d54 only the MC simulation parameters to match the pure dDMPC-d54 melting profile had to be adjusted turned out to be true within error, as the match with the calorimetric profile is good (see figure 6.2). In the case of the FTIR experiments, a discrepancy concerning agreement of the DSPC high temperature melting maxima and the maxima of the derivative in disordered chain ratio was observed (see e.g. figure 6.8, right panel). This deviation seems to stem from difficulties in temperature calibration. In our experimental setup we were not able to place a thermocouple within the sample chamber during the measurements, so we first had to run a calibration. We think that due to this temperature calibration an error of 2°C in temperature can easily occur.

The phase diagram displayed in figure 6.9 makes it clear, that the FTIR experiments and the Monte Carlo simulations match well. Bearing in mind that the Monte Carlo simulations fit calorimetric experiments, as the interaction parameters for the simulations are adjusted from the heat capacity profiles, it becomes clear that all methods complement one another very well. While by means of calorimetry only the bulk behavior can be investigated, leading to entropy, heat capacity and enthalpy changes, FTIR can resolve the melting of single lipid species in lipid mixtures. However, entropy, specific heat and enthalpy changes cannot be obtained from FTIR as it is not a quantitative method like DSC. Monte Carlo simulations can then be used to investigate fluctuations and domain formation processes in the membrane, but also single component melting in lipid mixtures.

6.3 Outlook

The FTIR spectrometer was delivered to the Niels Bohr Institute (NBI) in Copenhagen at the end of 2005. During my PhD. thesis I was the first person to work with the instrument and to make it easily usable by the students. A lot of work had to be put into the experimental setup design itself, but also the software. The software had to be programmed for temperature depending experiments and no suitable software was delivered to make the data evaluation.
Today the NBI does not only have a good working FTIR spectrometer that is specialized for the temperature dependent investigation of lipid samples, but also a new evaluation protocol for binary lipid mixtures that outplays the approach used before.
In the future, this setup can be used for continuative studies on binary lipid systems, for example studies on protein adsorption or the effect of anesthesia on lipid phase behavior.
Concerning anesthesia, Heimburg and Jackson applied a thermodynamic model and proposed that anesthetics will accumulate in the fluid phase of lipid membranes [193]. FTIR is a suitable method to elaborate this model from the experimental point of view and it can also give precise information on how the single lipid components are affected.

Chapter 7

Pore formation in lipid membranes

The commonly accepted picture of a biomembrane that is taught to the students nowadays is a membrane that is built up from lipids and proteins. Its function is to separate the sensitive cell interior from the hostile environment, but at the same time allow a controlled flow of molecules to ensure the cells metabolism. In this picture the lipids only have the function of building up a lipid matrix in which the proteins are embedded. Molecule transport and reactions are performed by proteins only and by no means influenced by the presence of lipid molecules. This is the way the Fluid Mosaic Model of Singer and Nicolson describes the cell membrane [17].

Already some years after the Fluid Mosaic Model was proposed, experiments showed that the lipid bilayer itself has a conductance also and that this conductance increases with increasing applied membrane potential [194]. Furthermore, the conductance steps observed resembled those observed in bilayers containing channel proteins or pore forming peptides [195–199].

In 1979 Abiror et al.[200] studied the electrical breakdown of lipid bilayer membranes and proposed that structural defects of the type of throughgoing pores are responsible for the nature of the background conductivity of membranes. Glaser et al. [201] proposed that two processes are underlying the reversible electrical breakdown of lipid bilayers. In the beginning hydrophobic pores are formed within the bilayer and at a pore radius of 0.3 to 0.5nm a reorientation of lipid molecules to hydrophilic pores takes place. Barnett and Weaver [202] developed a quantitative theory of electroporation of lipid bilayers that described the increase in electrical conductance, mechanical rupture and reversible electrical breakdown of membranes exposed to a charge pulse. Their simulations predicted that the fate of the membrane in any particular experiment is determined by the properties of the membrane and the duration and amplitude of the charging pulse. Freeman et al. [79] extended this theory and were able to calculate pore diameters and pore-pore separation distances. In the following years more and more evidence emerged, indicating that pores could form in bilayers that do not contain macromolecules such as protein ion channels or pore forming peptides. Gögelein and Koepsell observed channels in bilayers composed of commercially available lipids. However, they observed channels in membranes composed of lipids originating from biological sources only, but not in membranes from synthetic lipids [203]. Woodbury induced current steps by addition of SUVs close the bilayer [204]. Several groups reported spontaneous current fluctuations at the melting transition of lipid bilayers made from synthetic lipids [205, 206]. Boheim et al. observed a pronounced change in capacitance at the lipid melting temperature [206]. Antonov induced a lipid phase transition by addition of

Ca^{2+} that led to strong fluctuations in currents across the membrane [78].
Evidence for pore formation in lipid bilayers without incorporated channel proteins was not only observed by conductance measurements. Already in 1973 Papahadjopoulos et al. observed that the permeability of $^{22}Na^{+}$ ions out of DPPG vesicles is highest in the phase transition [9]. Nagle and Scott explained this fact with density fluctuations that might open cavities in the headgroup region so that ions could enter the membrane region [76]. Simulations performed by Cruzeiro-Hansson and Mouritsen in 1988 showed that the permeability will be highest in the phase transition regime due to a maximum in gel/fluid domain interface area, under the assumption that ion permeation is high at the domain interface area [73]. Heimburg showed that area and volume compressibility relate linearly to the heat capacity [11]. As the heat capacity is highest in the melting transition regime of lipid membranes, the above mentioned facts lead to the conclusion that molecule flux through membranes is highest in the melting transition regime, because pore formation in the membrane is enhanced due to enhanced fluctuations in area and volume. Pore formation in the phase transition of membranes composed of single lipid species has been described before [77, 78, 194, 203] and in this chapter we want to investigate pore formation in binary lipid mixtures and we present preliminary results on the fact that the permeability of lipid membranes at different temperatures seems to scale with the corresponding heat capacity. Pore formation in membranes composed of binary lipid mixtures has, to our knowledge, not been published before.

7.1 Pores in DOPC/DPPC membranes

As the BLM method has never been used in our group before, I was sent to the laboratory of Professor Mathias Winterhalter at the Jacobs University of Bremen (the former International University of Bremen) to learn the method. BLM is an acronym for **B**lack **L**ipid **M**embrane and it stems from the observation that the place on the teflon film where the membrane forms looks black if monitored with a microscope in reflected light mode. However, if the membrane is investigated with transmitted light, it appears bright. This can be seen in figure 3.4 in section 3.2.4.
The first lipid system investigated was a binary lipid mixture of DOPC/DPPC with a mixing ratio of 75:25. This mixture was chosen because one of the two peaks in the heat capacity profile of this mixture lies at 17°C [207], close to room temperature and is therefore easy to access experimentally. Additionally, for lipid mixtures showing phase coexistence at higher temperatures, water evaporation could complicate the experiments. Another factor for the choice of this lipid system was the fact that unsaturated lipids usually produce more stable bilayers for BLM experiments than saturated lipids do. Longer chainlength also stabilize the membranes (personal discussion with M. Winterhalter). Therefore DOPC was introduced as an unsatu-

Figure 7.1 (following page)
Pore formation in DOPC/DPPC 75:25 membranes. (*A*) Heat capacity profile of a DOPC/DPPC 75:25 binary lipid mixture. The higher temperature melting peak for the DPPC rich phase is located at 17°C. (*B*) and (*C*) No currents are observed in the fluid phase at 30°C, as can be seen from the current trace and the histogram, respectively. (*D*), (*E*) and (*F*) At 17°C fluctuations are observed at 40mV membrane potential and the inspection of the corresponding histogram for the whole current trace shows a shoulder (see inset in (*F*). (*G*) and (*H*)) show subsets of a trace recorded at 17°C, showing that regions with different amplitudes seem to occur (35 and 15pA respectively).

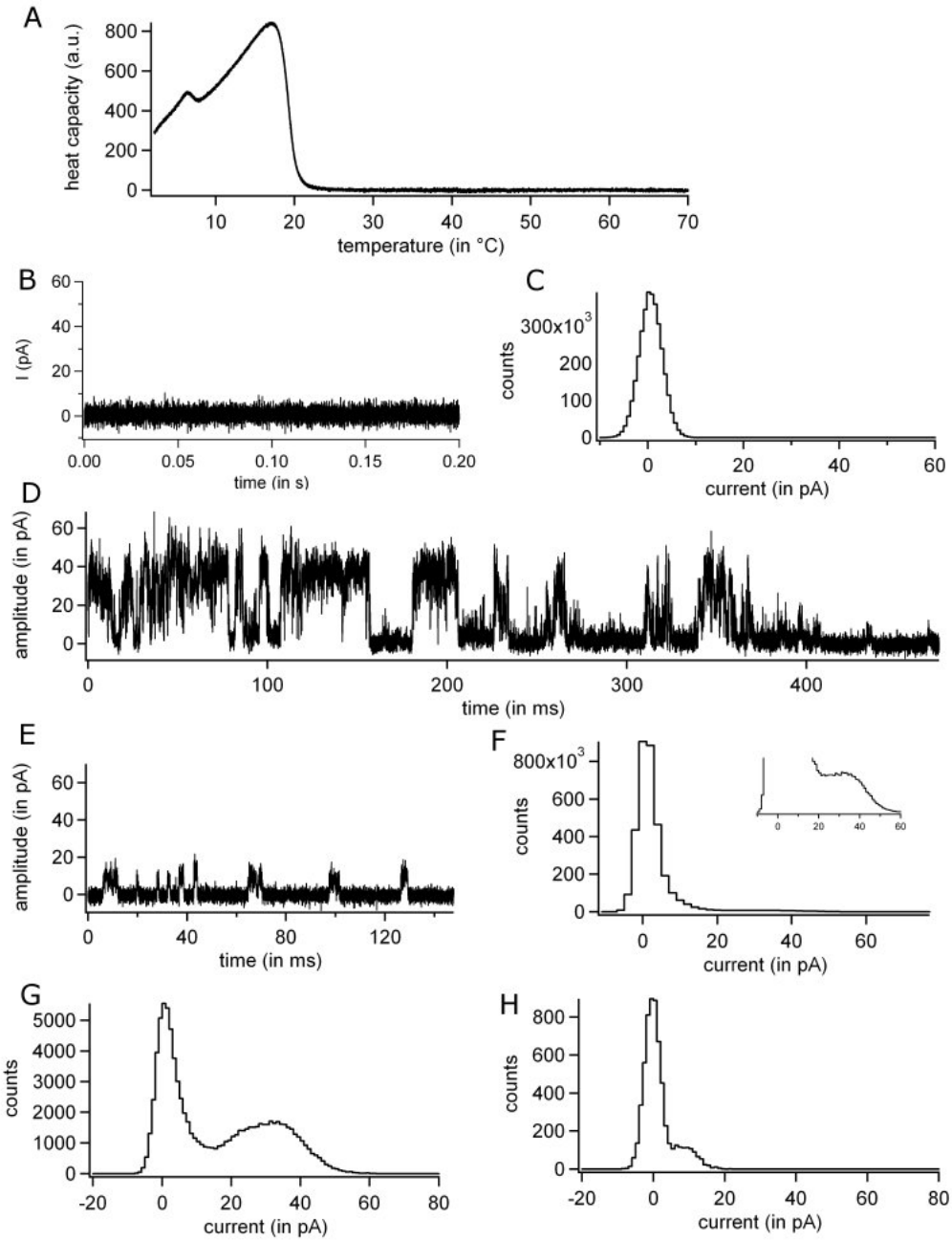
A
heat capacity (a.u.)
800
600
400
200
0
10
20
30
40
50
60
70
temperature (in °C)
B
I (pA)
60
40
20
0
0.00
0.05
0.10
0.15
0.20
time (in s)
C
counts
300x10^3
200
100
0
0
20
40
60
current (in pA)
D
amplitude (in pA)
60
40
20
0
0
100
200
300
400
time (in ms)
E
amplitude (in pA)
60
40
20
0
0
40
80
120
time (in ms)
F
counts
800x10^3
600
400
200
0
0
20
40
60
current (in pA)
G
counts
5000
4000
3000
2000
1000
0
-20
0
20
40
60
80
current (in pA)
H
counts
800
600
400
200
0
-20
0
20
40
60
80
current (in pA)

rated lipid component and DPPC with sixteen carbons was used because its chainlength is close to eighteen carbons and could probably give stable membranes in a mixture with unsaturated lipids.
The heat capacity profile of a DOPC/DPPC 75:25 lipid mixture is displayed in figure 7.1A. The DSC experiment was performed from 0°C upwards only, because measuring the heat capacity profile or pore formation below 0°C was not necessary as this range is not accessible experimentally without addition of anti-freeze that would influence the lipid phase behavior. The heat capacity profile shows a peak located at 17.1°C. Below 17.1°C gel fluid phase coexistence and above 17.1°C a homogeneous fluid phase is expected.
To observe pore formation a voltage clamp experiment was performed on a BLM composed of the same binary lipid mixture. Example sections of the current versus time experiments are displayed in figure 7.1B, D and E. Figure 7.1B shows an example trace at 30°C, a temperature well above the phase coexistence regime where the whole membrane is expected to be fluid. No current steps are observed at this temperature in the whole applied voltage range from 50mV to 200mV. As a consequence, the corresponding histogram shows a single Peak, the maximum is located at 0pA (see figure 7.1C). The picture changes in the phase coexistence regime at 17°C. In this case current steps that often seem to be discrete are observed in the voltage clamp experiment with 40mV potential applied, see figure 7.1D and E. A detailed investigation of the current traces in form of a histogram shows a shoulder ranging to about 50pA (see inset in figure 7.1F). Depending on the region of the current trace, two different current amplitude regions are observed, one in which current steps with an amplitude of about 9pA dominate and one in which current steps with an amplitude of about 30mV dominate, which can be seen from the histograms in figure 7.1G and H.

7.2 Interlude

The research trip to the Jacobs University of Bremen ended after three month and the results shown in the last section were presented to the scientific community and discussed vividly.
A few questions came up concerning the solvent content of the membranes, stemming from the bilayer preparation, and also the electrical fields applied to the membranes were criticized. The question also arose as to whether pore formation is induced by the applied electrical field or whether they form because of the fluctuations. In order to invalidate these concerns another research trip to the Jacobs University of Bremen was scheduled, in order to try to form BLMs with the *gentle pore formation* method that was recently published by Antonov et al. [77].
With the reported method the pores are formed by cooling the system into the phase transition. No strong voltage is applied to the membrane in order to induce pore formation.
For the upcoming experiments the lipid system DMPC/DSPC 50:50 was chosen because in this case the whole phase coexistence regime was accessible. Additionally, the low temperature explored in the DOPC/DPPC 75:25 system (17°C) might be disadvantageous in combination with the hexadecane used as solvent, as hexadecane freezes at 17°C (personal communication with C. Chimerel). The freezing might also induce pore formation.
The experiments with the DMPC/DSPC systems turned out to be far more difficult than expected as the membranes broke quite easily. These problems led to the decision to switch to the DPPC system to reproduce the experiments of Antonov et al. and thereby gain a feeling for a system with saturated chains. In many cases it is advisable to reproduce some experiments first and gain a feeling for the system, because a change in lipid components can easily change the behavior of the complete system.

7.3 DPPC membranes

The heat capacity profile of DPPC multilamellar vesicles, representative current versus time traces, together with the corresponding histograms and the mean currents measured[1], are shown in figure 7.2. The heat capacity profile shows a sharp peak at about 41.5°C, corresponding to the DPPC main transition, and a broad, less pronounced peak at about 34°C, corresponding to the pre-transition of the ripple phase [11, 208]. The lipid pre-transition is due to a melting of a fraction of the lipids and a lipid reordering to form line defects. These line defects are observed in multilayer systems only and not in single bilayers that are the object of interest in this study. At temperatures below the main transition the membrane is in the gel phase, at temperatures above the main transition the membrane is in the fluid phase. The current traces at 30°C and at 41°C (figure 7.2C do not show any steps in conductance that could stem from pore formation events. This can also be seen from the corresponding histograms displayed in figure 7.2D and E. At these two temperatures no current steps are observed in the whole applied potential range from 0mV to 75mV. At 43.5°C and 75mV membrane potential strong fluctuations are observed in the current versus time trace of figure 7.2C. The corresponding histogram shown in figure 7.2F shows two peaks, one at about 5pA and another at about 35pA for 75mV applied voltage. Below 75mV the histogram displays only one peak and the current trace does not show fluctuations. This data suggests that at 75mV a threshold is passed and pore formation events occur in the membrane. At a temperature of 50°C the histogram only shows a single peak up to 50mV membrane potential applied. At 75mV membrane potential a broad shoulder is observed in the histogram, extending to about 100pA. The mean currents measured at 75mV membrane potential for the current traces from figure 7.2C are displayed in figure 7.2B. At 30°C and 41°C no currents are measured. At 43°C the mean current drops from 10 pA in the beginning of the measurement to about 5pA and then increases quickly to 20pA after 20 seconds. After 20 seconds only a slight increase to 25pA is observed. In the following the mean current levels does not change significantly. The mean current recorded at 50°C starts at a level off 4pA and stays constant for about 20 seconds. After 20 seconds the mean current increases sharply and levels off at about 27pA until the end of the measurement.

[1] The mean currents were calculated the following way: For each measurement point of the current versus time trace from the experiment, the preceding currents measured were integrated. In this way the charge flown was calculated and then divided by the corresponding time in order to get the mean current.

Figure 7.2 (following page)
Pore formation events in DPPC membranes. (*A*) The heat capacity profile of DPPC membranes.(*B*) The mean current at different temperatures. (*C*) Current steps are observed at 50°C and 43.5°C. At these temperatures the membrane is expected to be in fluid phase and in gel-fluid phase coexistence, respectively. At 41°C and 30°C, when the membrane is in the gel phase, no current steps are observed. The shown traces were recorded at 75mV membrane potential applied. (*D*) and (*E*) The histogram corresponding to the 30°C and the 41°C traces show a single peak located at 0pA, not indicating pore formation events. (*F*) The histogram for the current trace at 43.5°C displays two peaks, one located at 5pA and one located at 30pA approximately. This is indicating pore formation events in the membrane. (*G*) The main peak in the histogram of the 50°C trace shows a broad shoulder and is indicative of pore formation events.

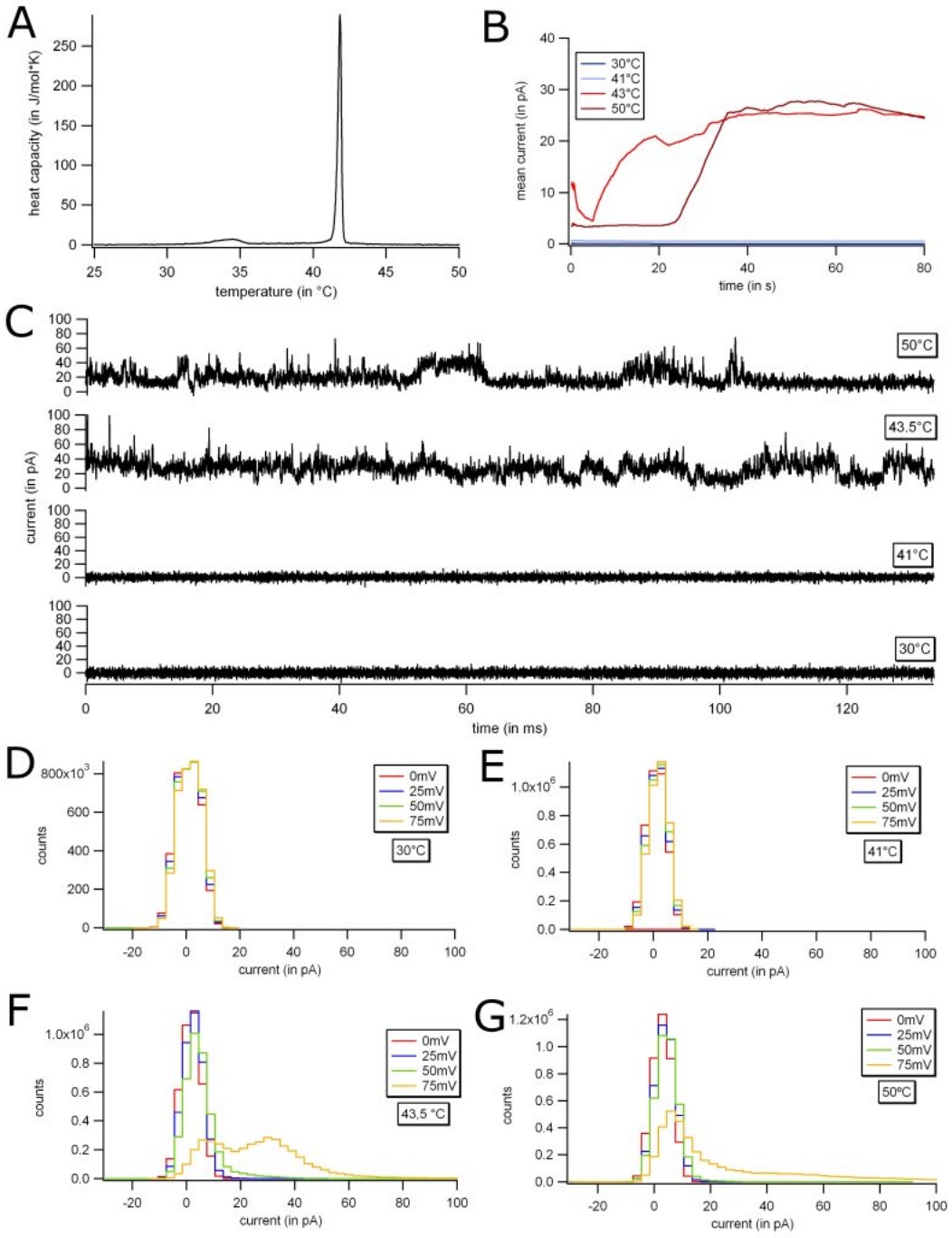
A
heat capacity (in J/mol*K)
temperature (in °C)
B
mean current (in pA)
time (in s)
30°C
41°C
43°C
50°C
C
current (in pA)
time (in ms)
50°C
43.5°C
41°C
30°C
D
counts
current (in pA)
0mV
25mV
50mV
75mV
30°C
E
counts
current (in pA)
41°C
F
counts
current (in pA)
43,5 °C
G
counts
current (in pA)
50°C

7.4 DMPC/DSPC membranes

Finally, some sets of experiments were conducted on membranes composed of DMPC/DSPC 50:50 membranes. Unfortunately, a complete set of experiments on a single membrane, covering the whole temperature range from below the melting transition regime to temperatures above the melting transition regime was never obtained, as the membranes usually broke during the experiments.

Figure 7.3A shows the heat capacity profile of a DMPC/DSPC 50:50 mixture. The data of this calorimetric scan was kindly supplied by Dr. H. Seeger. The heat capacity profile shows two peaks located at approximately 30°C and 44.5°C. During the whole melting transition regime ranging from about 28°C to about 47°C pore formation events will be expected, but they will be strongest at the temperatures corresponding to the peaks in the heat capacity profile as fluctuations are strongest in this case [11]. Figure 7.3C shows current versus time traces of a DMPC/DSPC 50:50 mixture with a potential of 75mV applied to the membranes at different temperatures. At 42.5°C, a temperature in the phase coexistence regime, fluctuations are observed in the membrane and starting at 50mV the corresponding histogram peak is shifted in comparison to the histogram peak at 0mV potential applied (see figure 7.3D). At 44°C and 75mV potential applied the fluctuations seem to be stronger compared to 42.2°C, as the histogram is ranging to more than 400pA (see histogram in figure 7.3E). The peak position of the histogram changes already at low applied potentials of 25mV. At 45.5°C, a temperature very close to the second peak in the heat capacity profile, fluctuations seem to be strongest and the corresponding histogram ranges up to 900pA, revealing three peaks at 75pA, 30pA and 600pA, respectively (see histogram in figure 7.3F). Already very low applied potentials of 25mV induce strong fluctuations and therefore a pronounced shoulder in the corresponding histogram. At 55°C, a temperature well above the phase transition regime, pore formation events are also observed and the measured currents range up to 300pA. At 75mV applied potential two peaks are observed in the histogram, located at 21pA and 78pA, respectively (see histogram in figure 7.3G). Figure 7.3B shows the mean current course for the traces displayed in figure 7.3C. At 45.5°C the highest mean current of about 300pA is measured. The mean current changes strongly in both directions indicating that periods of increased pore formation events change with periods where low fluctuations occur. The mean current recorded at 44°C stays at a nearly constant level of 100pA during the first 20 seconds and then increases slightly to 150pA. At 55°C, a temperature well about the phase transition regime an average mean current of 70pA is measured. This mean current does not change significantly. The lowest mean current is measured at 42.5°C. It stays at a constant level below 20pA during the course of the experiment.

Figure 7.3 (following page)
Pore formation events in DPPC membranes. (*A*) The heat capacity profile of DPPC membranes, the data was supplied by Dr. H. Seeger. (*B*) The mean current at different temperatures. (*C*) Current steps are observed at all investigated temperatures. The shown traces were recorded at 75mV membrane potential applied. (*D*), (*E*), (*F*) and (*G*) The histogram corresponding to the traces shown in B. All histograms are indicative of pore formation events.

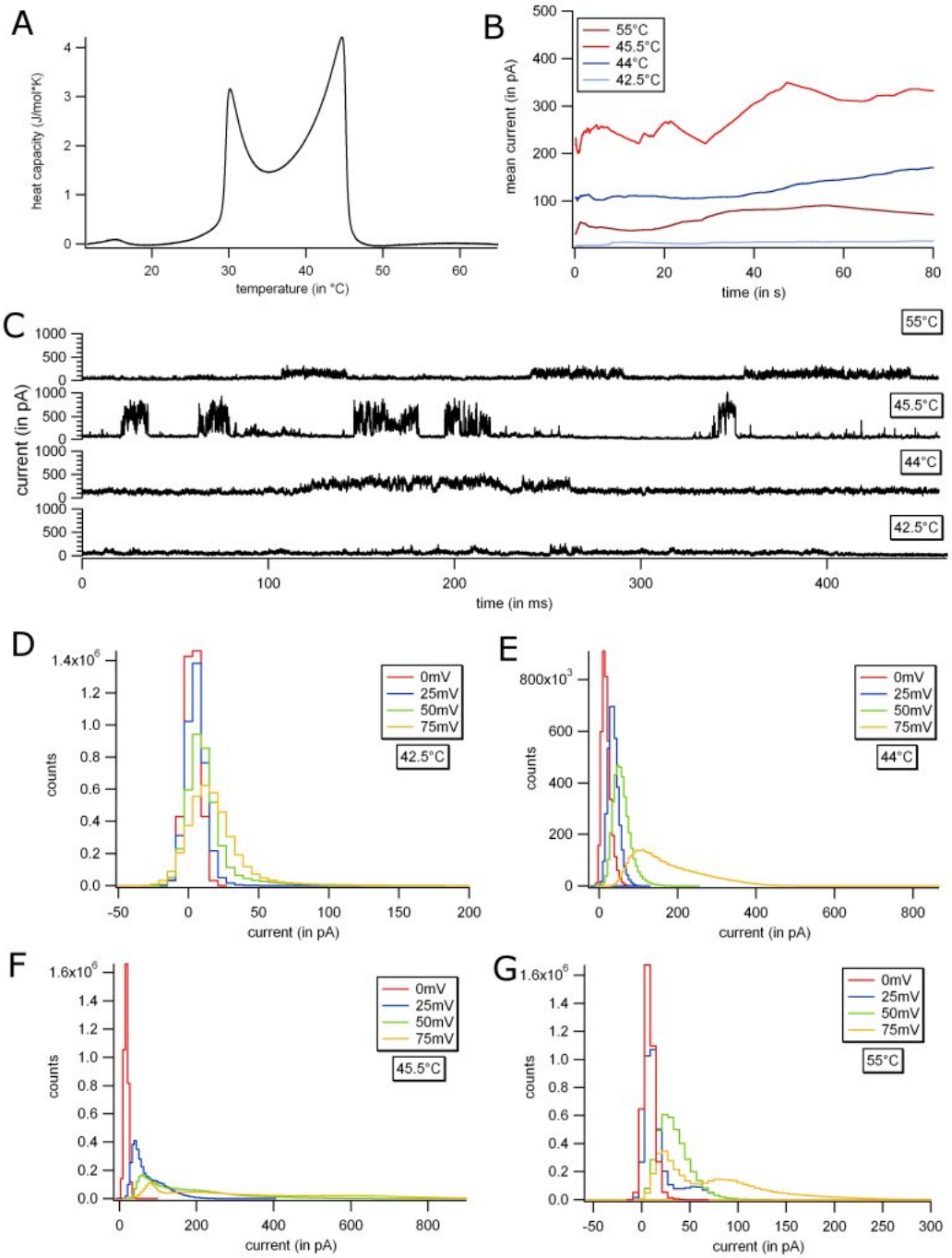
A
heat capacity (J/mol*K)
temperature (in °C)
B
55°C
45.5°C
44°C
42.5°C
mean current (in pA)
time (in s)
C
current (in pA)
time (in ms)
55°C
45.5°C
44°C
42.5°C
D
counts
current (in pA)
0mV
25mV
50mV
75mV
42.5°C
E
counts
current (in pA)
0mV
25mV
50mV
75mV
44°C
F
counts
current (in pA)
0mV
25mV
50mV
75mV
45.5°C
G
counts
current (in pA)
0mV
25mV
50mV
75mV
55°C

7.5 Discussion

In the case of the DOPC/DPPC mixture pore formation was observed in the melting transition regime, whereas no pore formation was observed at higher temperatures where the membrane is in the fluid phase (see section 7.1). It is important to note that histograms taken at different regions of a complete recorded current trace show different peak positions (see figure 7.1G and H). This shows that the fluctuations are not homogeneous in amplitude. There are time intervals where strong fluctuations dominate, leading to a higher conductance and time intervals where fluctuations are less pronounced, leading to a lower conductance.
In contrast to the DOPC/DPPC mixture, DPPC membranes showed pore formation in the melting transition and also at higher temperatures where the membrane is in the fluid phase. Pore formation events seem to start at 43.5°C, which is close to 43°C reported by Antonov et al. [77].
In contrast to the experiments reported by Antonov et al. [77] we only get amplitudes of up to 80pA, whereas Antonov et al. report currents of about 800pA for the same buffer concentration of 1M NaCl we used. Additionally Antonov et al. report ohmic behavior of the currents, without a threshold potential for the onset of pore formation. But in our experiments we saw pore formation above a threshold of 75mV. While the pores in the experiments of Antonov et al. showed opening times in the timescale of seconds, pore opening times in our experiments were in the timescale of milliseconds. In our experiments pore formation in the fluid phase was present, in contrast to Antonov et al. Pore formation in the fluid phase at 75mV seems to be less frequent than in the phase coexistence regime, but the shoulder in the histogram is extended to a broader range of currents, reaching up to 100pA approximately.
In the case of DMPC/DSPC we also got pore formation at temperatures within the phase coexistence regime and at temperatures above, as we already explored with DPPC. At 45.5°C where the temperature approximately matches the second peak in the heat capacity profile shown in figure 7.3A, the measured currents range up to about 800pA, which matches the value Antonov et al. report for 1M NaCl buffer on DPPC membranes. This could indicate that in the case of DPPC we did not hit the melting transition maximum exactly, but were close to it. At 44°C and 42.5°C, where the corresponding heat capacity value is lower than at 45.5°C, the maximum currents measured are lower, ranging up to 500pA and 100pA, respectively. This actually indicates that the higher the heat capacity value, the higher pore formation processes and therewith the currents across the membranes (see table 7.1).

temperature (in °C)	heat capacity (in J/mol*K)	max. current (in pA)
42.5	2.8	120
44	3.6	450
45.5	4.2	930

Table 7.1
The measured maximum current of DMPC/DSPC 50:50 membranes at 75mV membrane potential increases with increasing heat capacity values.

The mean currents measured for the DPPC and the DMPC/DSPC 50:50 BLM (see figure 7.2B and 7.3C, respectively) serve interesting information about the two systems. The DPPC system should be divided into the region from 0 to 20 seconds and in the region from 20s onwards for discussion. In the first regime the mean current at 43°C is higher than the mean currents measured at the other temperatures. This temperature seems to be closest to the main transition of DPPC. At 50°C, a temperature well above the main transition, where the membrane is in the fluid phase, an increased mean current is measured. However, in the first regime the mean current value at 50°C is lower than at 43°C. For the temperatures below the main transition, at 41°C and 43°C, respectively, no significant

mean currents are measured. At these temperatures the membrane is in the gel phase. In the second regime the mean currents measured at 50°C and 42°C, respectively, reach the same value of about 25pA. The observation that the mean current for the trace recorded at 50°C increases steeply after 20 seconds indicates that the membrane gets instable at this point. This was observed in many experiments and is a fact that makes the experiments difficult to perform. It often occurs that a membrane shows quite stable behavior for a while and then suddenly gets instable, showing strong fluctuations. In some cases these fluctuations stabilize again, in other cases the membrane finally ruptures. In the case of the experiment presented here the membrane stabilized after the potential was switched off in the end of the recording period. The same membrane was used for all temperature levels investigated. This experiment shows how difficult the experiments are to perform and how sensitive the membranes are. They seem to be quite stable in the gel phase, but in the phase coexistence regime and also in the fluid phase they seem to brake easily. When pores form the membrane is in a critical regime close to rupture. In many cases the membrane breaks finally. In the case of the DMPC/DSPC mixture the picture is more clear (see figure 7.3B). All four measured mean currents are separated clearly. The mean current measured at a temperature corresponding to the heat capacity maximum (43°C) is highest. Also the current measured at a slightly lower heat capacity value surmounts the mean current measured in the fluid phase (44°C and 55°C, respectively). Interestingly, the mean current measured at a low heat capacity value within the phase transition regime (42.5°C) is lower than the mean current level in the fluid phase. However, as is observed with DPPC, the mean current value measured at the maximum of the heat capacity fluctuates a lot, indicating a very instable membrane. The experiments indicate that no pore formation is observed in the gel phase, where the membrane is very stable. Highest fluctuations are observed at high heat capacity values. In the fluid phase the membrane can get unstable also. Which parameters drive the membrane in the fluid phase into critical behavior has to be explored in the future. An indication for the possibility that the melting transition was not hit exactly in the case of the DPPC experiments comes from the fact that the mean current measured at the melting transition is much lower than in the case of DMPC/DSPC. The mean current values for the DMPC/DSPC system altogether are higher than for the DPPC system. This might relate to the fact that mixed lipid systems probably have a higher permeability than pure lipid systems.

In the case of DMPC/DSPC no threshold values for the occurrence of pores are observed as is the case for our DPPC experiments, instead the currents increase with increasing applied membrane potential. As we do not observe distinct current steps as Antonov et al. do [77], we cannot redraw their conclusion that the currents display ohmic behavior. If the peak positions of the high current peak in the histograms are plotted versus applied membrane potential, a non-linear behavior is observed.
The most striking differences between the results reported by Antonov et. al and the results shown within this thesis are the different timescales of the pore opening times, a continuous distribution of observed current steps in our case, and our observation of pore formation processes in the fluid phase. The first two discrepancies might be explained by different pore sizes, possibly due to different solvent concentrations in the membrane, as it is nearly impossible to estimate the solvent concentration in the membrane. If we get smaller but a higher number of pores and these pores show cooperativity in opening and closing, shorter opening times could be expected, as smaller pores could open and close faster than bigger pores.
Pore formation processes in the fluid phase seem to be reasonable, as the membranes in the fluid phase have a higher permeability than in the gel phase, which has been shown in efflux experiments before [9].

As the BLM experiments turned out to be quite difficult and membranes broke quite often during the experiments, or in some cases even no pore formation events were observed either in the fluid phase or in the phase coexistence regime, the data presented in this chapter should be considered preliminary only. But what we can definitely conclude from our experiments is that there is no pore formation in the gel phase, but often strong pore formation in the phase coexistence regime and also pore formation within the gel phase.

Concerning the gentle pore formation technique reported by Antonov et al. [77] it seemed as if this method worked in the case of DMPC/DSPC lipid membranes, but not in the case of DPPC membranes. With DPPC membranes we had to apply about 75mV membrane potential to induce pore formation.
The accuracy of the temperature calibration for the BLM experiments is ±1°C, so we match the measured temperature level for DPPC pore formation of Antonov et al. within error. The DPPC melting temperature measured by DSC (41.5°C) differs from the temperature where pore formation is observed (43.5°C), but solvent incorporated into the membrane for the BLM experiments will shift this melting temperature, probably to higher temperatures [12, 193]. Actually, Heimburg and Jackson [193] report a melting point depression for octanol, but the impact of the decane/chloroform/methanol mixture that was used in the case of the experiments presented here should be investigated by calorimetry, to be able to make a judgement about its impact on the melting transition temperature.

7.6 Outlook

The picture of pores forming in membranes is quite interesting in so far as it might be an additional possibility for cells to control the ion gradient between outside and inside the cell. Pore formation is a fast process and might, for example, be needed in exceptional cases of lack of channel proteins, as it will be faster than the synthesis and transport of channel proteins to the place, where they are needed.

One of the strongest criticisms concerning pore formation in BLMs is the impact of the solvents that are used during membrane formation. This is motivated by the idea that the solvents might influence the membrane behavior and drive pore formation. A model to support this argument has not been proposed so far. The experimental results presented in this chapter very clearly show that the pore formation events are related to the fluctuations in the membrane, but to finally rule out this point of criticism, the method should be refined to systems where no solvents are used to form the membranes. Some approaches have been tried already, where GUVs are placed on a hole in a teflon film by solvent suction through the hole, but the experiments did not lead to results so far, as leakage was observed, probably at the vesicle/teflon interfacial region.

The work presented within this chapter was an important step to introduce the BLM method to the Membrane Biophysics Group at the Niels Bohr Institute in Copenhagen and it is the initial point and motivation for ongoing research projects.

Chapter 8

The lever rule applied to GUVs of DLPC/DPPC lipid mixtures

Lipid lateral phase separation was investigated in lipid monolayers using fluorescence microscopy in the 1980s already [26, 209]. In these experiments lipids dissolved in non-polar solvents were spread on a water surface. After the solvent evaporated, a lipid monolayer had formed. A fluorescent dye that segregated into one of the coexisting phases preferentially was added to make the domain pattern visible.
From the aspect of biological relevance bilayer systems are more suited experimental systems, because monolayers are very scarce in natural systems. The evidence for segregation of phases in bilayer systems reaches back to the early eighties (see review in [210]), but it was until 1999 that domain formation was made visible on Giant Unilamellar Vesicles (GUVs) [28, 211]. A few years later Samsonov et al. succeeded to demonstrate phase separation visually in planar bilayer membranes (BLMs) [212].
In combination with the electroformation method introduced by Angelova and Dimitrov [82], fluorescence microscopy turned out to be a well suited tool to investigate lateral phase separation in spherical bilayer systems. The electroformation method supplies a high yield in giant unilamellar vesicles [82]. In the following years GUVs were used in a variety of studies to explore binary and ternary phase diagrams of lipid mixtures with and without cholesterol [54, 125, 213, 214]. Other investigations concentrated on the diffusion behavior of fluorescent probes in different domains with Fluorescence Correlation Spectroscopy (FCS) [28, 215]. Bagatolli and Gratton investigated the domain growth or disappearance, when the liquidus line of the phase diagram was passed during a change in temperature [34, 216]. In these studies they used the Laurdan Generalized Polarization (GP) function to assign fluid and gel phases [92]. The GP function can be used to quantify the influence of cholesterol to lipid phases also, because it provides information about water relaxation processes in lipid membranes [125]. That in turn is related to the phase state.
Recently, macroscopic phase separation was also observed in more complex membranes containing lipid extracts from natural tissue, for example brain ceramide or lung surfactant [14, 81].

It is clear that the visual observation of domains was quite an important step, because from this point on it was possible to direct the experimental technique of interest to the domain. Previously the coexistence of lipid domains in bilayers were assigned using indirect methods lacking visual information.

However, most of the studies of liquid ordered/liquid disordered and gel/fluid phase coexistence investigated with fluorescence microscopy published today concentrate on the visual inspection only. For example, a change in domain shape in cholesterol containing membranes composed of an equimolar binary mixture of DOPC/DPPC with 25% cholesterol. With more than 10% cholesterol fraction the so called liquid ordered phase forms and circular domains are observed [13]. In contrast, gel phase domains are not circular shaped [28]. The round shape of the liquid ordered domains reduces the free energy of the system by minimizing the interfacial energy contribution. Publications that investigate the domain shapes and areas on GUVs quantitatively are not found yet.

In this chapter a new approach to calculate the gel/fluid domain area ratio from 3D vesicle pictures is introduced. Stacks from DLPC/DPPC GUVs were recorded with a confocal microscope and deconvoluted with the Huygens Professional Imaging software. The resulting stacks were projected on a sphere and the gel/fluid domain ratio was calculated with an IDL plugin written by Dr. S. Härtel from the department of medicine of the University of Santiago (see section 3.3.3 for details). The obtained domain area ratios are compared to the gel and fluid phase ratios expected from the lever rule (see equation 2.10 and 2.11 in section 2.1.2).
The lever rule was cited in the context of the ideal solution theory in chapter 2.1.2. However, it is also applicable to regular solutions. The theories can be used to calculate phase diagrams of binary lipid mixtures. In the case presented here, the lever rule is applied to a phase diagram drawn from calorimetric experiments on a DLPC/DPPC lipid mixture. Strong deviations from the predicted values from the lever rule might stem from domain formation on the nanometer scale. The vesicle images are taken with confocal microscopy and nanoscopic domains cannot be observed with this technique, due to the resolution limit of the setup.

8.1 Experimental results

It seems to be important to start the results section with a note. The experiments to produce the data for this chapter were performed end of July 2007, one month before this thesis had to be submitted. A lot of experimental data was obtained during a two weeks visit in Santiago, but not all the data has been evaluated since then. The computation of the vesicle stacks from microscopy takes a lot of computation time. Bearing this in mind, the data presented here has to be treated preliminary only. However, the method presented is new and the results are exciting.
The GUVs for the results presented in this chapter were prepared by electroformation on ITOs (section 3.2.1). The vesicles were labeled with Bodipy and Dil-C_{18}. In the case of DLPC/DPPC GUVs, Bodipy is known to label the fluid phase [28]. From the confocal experiments it can be seen that Dil-C_{18} partitions into the gel phase of this particular mixture preferably.
In figure 8.1 representative sphere projected[1] GUVs with different DLPC/DPPC mixing ratios are displayed. The green areas correspond to fluid domains and the red areas correspond to gel domains, respectively. The fraction of gel phase area increases with an increasing amount of DPPC. DPPC is the component with the higher melting temperature. The transition midpoint of DPPC lies at 41.3°C [6]. The transition midpoint of DLPC lies at -1.9°C[6]. The fluid phase

[1] The sphere projection is the result of the treatment of the confocal images with the image processing procedure described in chapter 3.3.3. Briefly, the areas corresponding to gel and fluid domains are projected on a sphere, in order to evaluate the domain areas and not volume information.

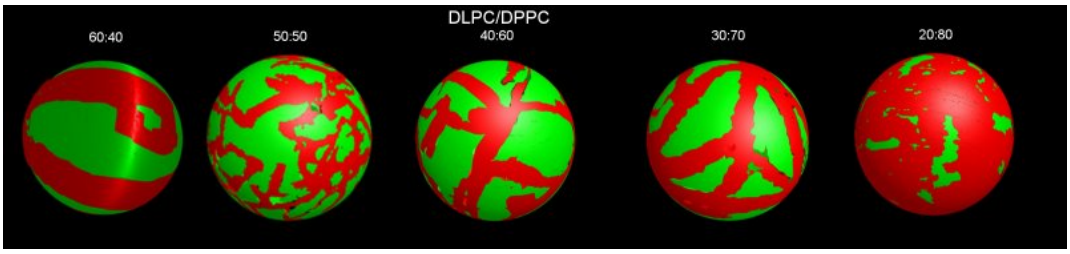

Figure 8.1
DLPC/DPPC GUVs with different lipid mixing ratios at 20°C. The pictures were obtained by projecting deconvoluted image stacks onto a sphere. Fluid phase domains are represented in green color (Bodipy fluorescence) and the gel phase domains are colored red (Dil-C_{18} fluorescence), respectively. The data extracted from the vesicle stacks indicates an overlap of green and red areas at the location of the phase boundaries. The overlap is not shown in these pictures. The red areas are projected on top of the underlying green layer. The vesicle diameter is about 30µm for all vesicles displayed.

of DLPC/DPPC vesicles displaying phase coexistence is rich in DLPC whereas the gel phase is rich in DPPC.
The phase diagram of the DLPC/DPPC mixture is shown in figure 8.2. The data to draw the phase diagram was taken from [217]. In the corresponding study the phase boundaries were drawn from heat capacity profiles [217].

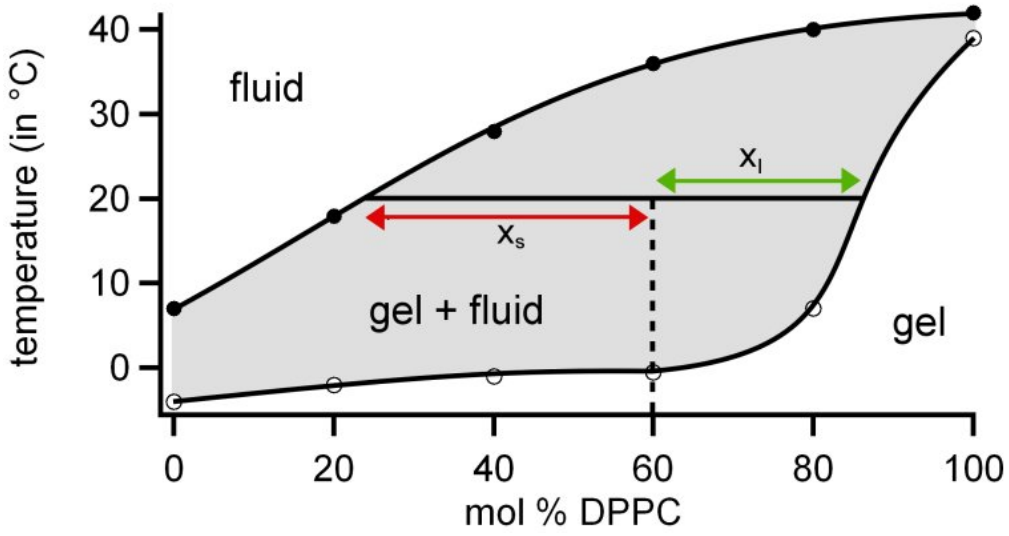

Figure 8.2
The phase diagram of the DLPC/DPPC mixture. The tie line is drawn at 20°C. At this temperature the confocal experiments were conducted. The values x_s and x_l do not correspond to the gel and fluid molar fraction, see equation 2.10 and 2.11 for details. *The data to draw the phase diagram was taken from [217].*

The phase diagram was used to calculate the fraction of lipid molecules in the gel and in the

	lever rule		experiment			
% DPPC	mol % gel	mol % fluid	mol % gel	mol % fluid	% overlap	vesicles
40	23	77	30.7±5.9	69.3±5.9	2.2±1.2	2
50	39	61	53.5±3.8	46.5±3.8	6.5±0.3	2
60	57	43	46.9±4.3	53.1±4.3	8.8±3.6	3
70	71	29	62.9±6.3	37.1±6.3	4.7±2.4	9
80	86	14	79.8±5.4	20.2±5.4	14.0±0.1	2

Table 8.1
Comparison of gel/fluid area ratios expected from the lever rule compared to gel/fluid area ratios calculated from domains observed on GUVs composed of DLPC/DPPC mixtures. The overlap of gel and fluid domains is stated, as well as the number of vesicles explored for each composition.

fluid phase, x_S and x_L, respectively (see section 2.1.2). The tie line in the phase diagram was plotted at 20°C. At this temperature the confocal experiments to produce the vesicle stacks were conducted. The expected values of the gel and fluid fractions are listed as percentage fractions in table 8.1.

A direct comparison of the domain area fractions to the values predicted from the lever rule is not possible. The lever rule considers molar fractions whereas on the GUVs area fractions are compared. The area of a fluid lipid changes for about 25% in respect to a solid lipid [218]. The change in area for DLPC is not known yet, but it can be estimated. The molecular area of DPPC lipids in the gel and the fluid phase is about 47.9Å^2 and 64Å^2, respectively [218]. The molecular area in the gel phase does not change significantly for different chain length [219]. The fluid phase area per molecule of a DMPC lipid, which chainlength is two carbons shorter in respect to DPPC, is lower than for a fluid phase DPPC lipid, namely 59.6Å^2 [218]. If one assumes a linear decrease of fluid area per molecule with decreasing chain length, a molecular area of 55.2Å^2 would be expected for DLPC. The chainlength of DLPC is 4 carbons less in comparison to DPPC. Additionally, it is reported that the change in enthalpy during a lipid transition, ΔH, is proportional to the changes in volume and area [11]. The change in enthalpy for the transition of DLPC is about one third lower than for DPPC [6]. As the change in enthalpy is proportional to the change in area, one would expect a change in area that is one third lower than for DPPC. This results in an molecular area of about 53Å^2 in the case of DLPC. For a binary mixture of DLPC/DPPC we assume this value to be a little bit higher, because DPPC lipids are also present in the fluid phase. In order to compare the molar fractions obtained from the lever rule with the domain area fractions of the GUVs, the area of the fluid phase was therefore reduced by a factor of 1.2.

The gel and fluid area fractions extracted from the GUVs are compared with the gel and fluid molar fractions calculated from the lever rule in figure 8.3 and in table 8.1. The fluid area fractions obtained from the GUVs are lower than the expected values from the lever rule at 40 and 50% DPPC lipid fraction, the gel area fractions are slightly higher at the corresponding DPPC molar fractions. At higher DPPC lipid fractions the predicted and the measured values agree within experimental error.
The strong deviation of the data point at 50 mol % DPPC is explained by the fact that the Bodipy fluorescence signal in the experiments was rather poor. Therefore the signal to noise

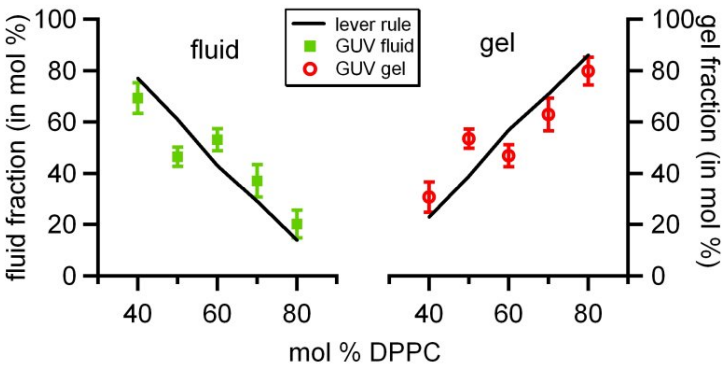

Figure 8.3
The gel and fluid fractions calculated from GUVs with different DLPC/DPPC compositions. The values are compared to the values predicted from the lever rule (section 2.1.2). The theoretical values derived from the lever rule were calculated in 10 mol % steps.

ratio in this special case was so low that most of the information got lost during the deconvolution. In order to still obtain values for the fluid and gel area fractions, all area that was not gel was supposed to be fluid. This assumption leads to an overestimation of the gel phase area that is clearly visible in figure 8.3. From this fact it becomes clear that the experiments have to be performed with one fluorophore to label each phase. The overlap of two fluorescence signals for each phase is necessary to locate the domain boundaries

In the confocal experiments an overlap of gel and fluid phases was observed. In this respect overlap means, that it was not possible to assign only one phase in some regions. This overlap seems to occur exclusively in the regions of the phase boundaries. The overlap percentage is listed in table 8.1, but it is not shown in the vesicle pictures of figure 8.1. The confocal GUV pictures were recorded with two channels, one channel for each fluorophore. In the pictures displayed in figure 8.1 the gel domains are simply projected on top of the fluid domains.
The origin of the overlap is discussed in the following section. A large overlap correlated with a poor fluorescence signal from the Bodipy fluorophore in the fluid phase usually. For the evaluation of the confocal pictures only vesicles with an overlap below 15% were investigated. A lower threshold value might be preferable, but as only a few vesicle stacks have been processed so far, 15% were the lowest value possible, in order to reveive at least some statistical significance. The overlap was treated in the following way: The area of the fluid domains was reduced by a factor of 1.2, as stated above. Both domain areas of fluid and gel domains were summed. This sum was treated as the total area to calculate the corresponding fluid and gel domain fractions. The percentage of overlap was calculated from the surface of the vesicle. The surface of the vesicle is obtained from its radius. The radius is estimated from the vesicle stacks (section 3.3.3). From the proportion of the sum of gel and fluid areas to the total vesicle surface, the overlap was calculated.

So far the DLPC/DPPC 30:70 lipid mixture has been evaluated to the highest extent. In all, thirteen vesicles have been processed from confocal image stacks for this mixture, nine of them displayed an overlap below 15%. The mean gel/fluid fraction percentage distribution is

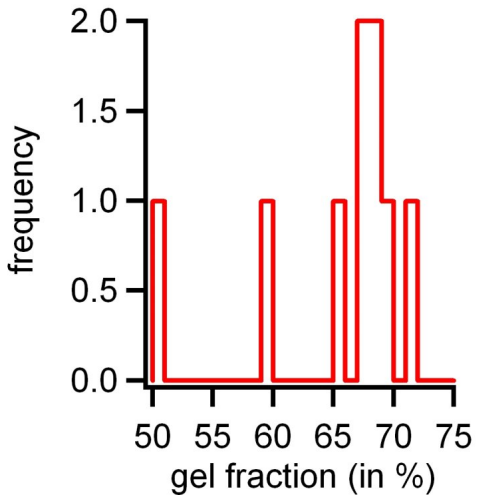

Figure 8.4
Histogram for the calculated gel fractions of several GUVs composed of a DLPC/DPPC 30:70 mixture.

65.2% gel phase fraction to 34.8% fluid phase fraction. The mean square deviation is 6.2%. The histogram for the gel phase fraction in figure 8.4 shows that besides two exceptions the calculated molar fractions of the single vesicles scatter close to the maximum at 67.5%. The expected value calculated from the lever rule is 69% (see table 8.1).

8.2 Discussion

With the exception of one data point the results in figure 8.3 follow the trend of the lever rule well. The fluid fraction decreases while the gel fraction increases with increasing amount of DPPC. However, the data point at 50 mol % DPPC does not fit the data within error. This stems from the fact that the gel phase has been overestimated, as mentioned in the results section of this chapter. The remaining data points match the lever rule values well within error. For more than 50 mol % DPPC the values are slightly higher and lower for the fluid and the gel fraction, respectively.

The overlap of gel and fluid domain areas demonstrates that it is necessary to label both phases. If one fluorescent probe is used only, the corresponding domain area will be overestimated. A small fraction of the overlap could be explained by the use of dyes to label the lipid membrane. The labels serve the possibility to make the 5nm thick membrane visible. Due to the fluorescence the membrane seems to have a thickness of about 300nm in confocal images. Therefore, if a sharp domain boundary would be assumed, the measured boundary would already extend further than it really is. However, this effect will not explain the occurrence of 50% overlap (the highest value measured, but not included in the data).
Most likely, the explanation of a high overlap lies in the partitioning behavior of the fluorophores in combination with the data treatment protocol and the fluorescence properties of the dyes. In our experiments Bodipy bleached very fast and therefore a low excitation laser power had to be applied. This led to a low fluorescence signal that in some cases was even hard to distinguish from the background signal (see figure 8.5). In addition, Bodipy was not completely excluded from the gel phase. A fraction of Bodipy was present in the gel phase also, resulting in a low fluorescence signal from gel domains (figure 8.5). This led to the problem to distinguish gel

phase from fluid phase in some instances, even though all image stacks were treated by visual inspection during the computational steps. In contrast, DiI-C_{18} has a very strong and stable fluorescence signal, but it partitions into the fluid phase to a low extend too (see figure 8.5). Therefore the same problem as stated above occurs. Another important factor that has to be taken into account is the interface between gel and fluid domains. Most likely it is not sharp, but represents a gradient in height, in order to approach the thickness of the fluid phase to the thickness of the gel phase. The free energy contribution of a gradient structure will be lower than that of a step like interface. How far this gradient region might extend is not known yet. Studies of the interfacial regions of domains on freestanding bilayers are rare.

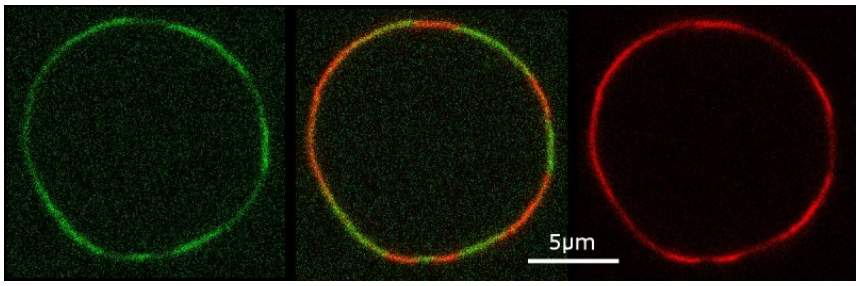

Figure 8.5
Partitioning behavior of Bodipy and DiI-C_{18}. (*left*) Bodipy is also present in the gel phase to a low extent. (*middle*) The superposition of the Bodipy and DiI-C_{18} fluorescence signal. (*right*) DiI-C_{18} is present in the fluid phase to a low extent.

A tool to study the interfacial regions could be Atomic Force Microscopy (AFM). The resolution of the AFM lies in the nm range. Nanodomain formation in DLPC/DPPC systems prepared on mica has been reported already [7]. No gradient in height that could explain the observed overlap, was reported from gel to fluid phase domains in this system. In this respect, however, supported bilayer systems should be considered with care, because strong interactions with the underlying mica occur. Additionally, large patches of membrane without any defects are seldom observed. For further studies it might be advisable to perform AFM investigations directly on GUVs. This possibility will be discussed further in the outlook section of this chapter.
Besides an overlap, areas on the sphere projected vesicles are visible, where no phase was assigned. These areas occur because the fluorescence signal in these zones was probably too low. These regions are exclusively present at the domain interfaces, too (see figure 8.6). This second effect indicates that especially the domain boundaries are difficult to allocate. It is possible, that the dye molecule partition behavior is different in the phase boundaries. This might be due to a height gradient in these regions, as stated above already. Actually, the properties of the domain interfaces are not well studied yet. The method we introduced here might be an adequate tool to investigate these areas. However, this depends on their measures, of course. If they extend further than the resolution limit of the microscope, the method described her could deliver valuable information about these zones. Correlation studies could be done in these regions.
The possibility of microdomains occurring in the DLPC/DPPC mixtures studied within this chapter cannot be excluded so far. The size of the microdomains reported in the study of Tokumasu et al. [7] lies in the range of about 20 to 80nm. Objects of this size cannot be observed with confocal microscopy, because of the resolution limit of about 500nm. The occurrence of Microdomains would lead to an underestimation of the fluid phase and an over-

estimation of the gel phase fractions calculated from GUV images. Gel microdomains have a higher molecule per area ratio than fluid microdomains.

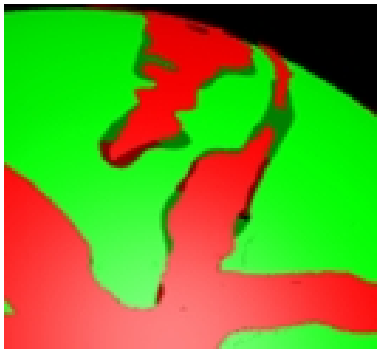

Figure 8.6
In many cases it was not possible to assign a fluid phase or a gel phase at the domain boundaries. These regions are transparent here. Due to the transparency the opposite inside of the vesicle is visible. The opposite inside is displayed slightly darker than the outer surface. This picture is a detail of the DLPC/DPPC 40:60 vesicle of figure 8.1.

Another factor that could affect the results presented in this chapter is the influence of the dyes to the melting transition of the lipids. Calorimetry clearly shows that the melting transition peak of a pure DPPC is influenced by a dye concentration of 1% already (see figure 8.7, that was taken from my diploma thesis [220]). The melting transition of pure DPPC shifts to lower temperatures for DiI-C_{18} and Bodipy. Therefore the dye concentrations were kept minimal in the experiments. The concentrations of Bodipy and DiI-C_{18} were 1% and 0.5%, respectively. In order to include the influence of the dye molecules to the melting behavior of the lipid membranes into this study, the heat capacity profiles to draw the phase diagram should be measured with fluorophores included. On the basis of the shift of pure lipid melting transitions the error can be estimated to be about 1%.

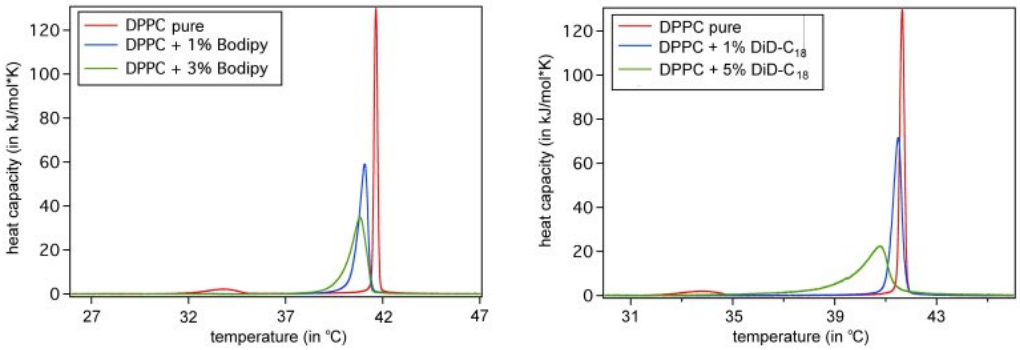

Figure 8.7
The influence of fluorescent dye molecules on the melting transition of pure lipid bilayers studied with calorimetry. At 1% dye concentration an effect is already observed. (*left*) Bodipy shifts the melting transition midpoint to lower temperatures. (*right*) DiD-C_{18}, a dye similar to DiI-C_{18} shifts the melting transition midpoint to lower temperatures, also.

The data presented here has to be treated preliminary only, however, the first outcome already makes clear what has to be done experimentally to improve the method. The Bodipy dye turned out to be an improper fluorophore for these studies, because of its photobleaching susceptibility. It should be replaced by a more stable fluorophore in the future. The fluorophores should be selected in a way that no overlap of the emission spectra of the two fluorophores occurs, but

most of the fluorescence emission is selected. An overlap of the emission spectra could lead to a signal from the opposite phase. Special attention should be directed to the filters applied on the microscope. The applied microscope filters have to match the fluorescence emission spectrum of the dyes perfectly, in order to collect most fluorescence. In addition, more dyes should be checked for their partition behavior in order to find one that shows stronger preference for one of the phases, than the dyes used within this study did.

8.3 Outlook

This chapter introduced a new technique to calculate gel/fluid area fractions from 3D GUV images. The procedure offers a great variety of possibilities to quantify phase separation directly from spherical free standing bilayers. GUVs have the highly visible feature that no boundary effects with supporting material occur. This is usually a strong criticism in AFM and BLM experiments.
Future experiments could investigate the area distribution function, the boundary contour length or membrane shapes. Additionally, the influence of cholesterol and other molecules to domain structure could be quantified.
This technique might also be used to investigate the properties of the phase boundary, as this study shows that more attention should be directed to the phase boundaries.
One point that was mentioned in the discussion section already, is that AFM experiments should be performed on GUVs directly. Probably complete spherical GUVs might be difficult to keep in place in order to place a AFM cantilever on the top. However, if the electroformation method is applied in the right manner, lipid half spheres are easily obtained. These lipid half spheres have an awkward shape sometimes (see figure 8.8), but they are fixed in place and will not slip when they are approached with the AFM cantilever. A question that has to be answered then is, of course, if the membrane is too soft when it is not supported. In this case the cantilever will just push on the membrane but might not detect the domains.
Another technique that could be applied would be Stimulated Emission Depletion (STED) microscopy, that was introduced by Dyba and Hell in 2002 [221]. The resolution of a STED microscopy is far below 100nm and could be used to investigate the domain interfaces if they extend further than this distance.

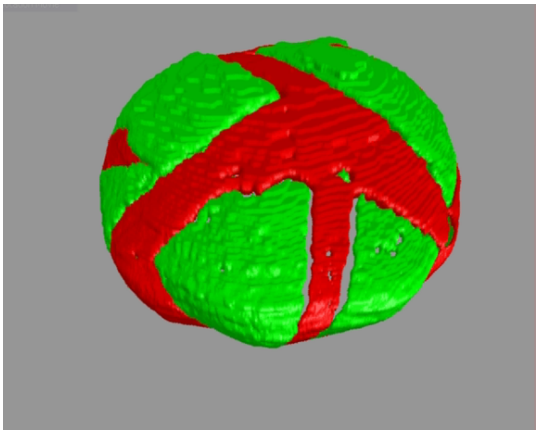

Figure 8.8
A lipid half sphere produced with the electroformation on ITOs. It is composed of a DLPC/DPPC 30:70 mixture.

Chapter 9

Conclusion

This thesis contributes to the understanding of phase transitions of model membranes. Several different experimental and theoretical techniques have been applied to study phase transitions and lateral phase separation in artificial model membranes. With these techniques a broad spectrum of different aspects related to model membranes has been studied.
For the first time, absence of liquid ordered/liquid disordered phase coexistence was observed in POPC/ceramides membranes containing more than 20 mol % cholesterol. In contrast, in POPC/cerebrosides lipid membranes containing more than 25 mol % cholesterol, the coexistence of two liquid ordered phases was observed. These two findings are remarkable as the structure of both molecules is nearly the same. They only differ in the headgroup structure and cerebrosides can be converted to ceramides by enzyme activity and vice versa. Therefore the enzyme activity could lead to drastic changes in the membrane properties. This could be of vital importance for biological systems, but has to be elaborated in future experiments.

An improved method to investigate the melting of single components with FTIR in binary lipid mixtures, namely the difference spectra method, was implemented. The routine was programmed in a user friendly way to make it easy to use to anybody. The comparison to Monte Carlo simulations showed that the spectroscopic results match calorimetric data well. Monte Carlo simulations proved to be an essential tool to deepen the understanding of the experimental results. The Difference Spectra Method will be an important technique to investigate the impact of small molecules to binary or even more complex lipid mixtures. Here, small molecules could be cholesterol or anesthetics, for example.

It was shown experimentally, that the phase transition affects the permeability of lipid membranes. The results are consistent with previous reported data [9, 77]. In this thesis it is speculated that the permeability scales with the heat capacity and the assumption was based on theoretical considerations. To prove this, permeability measurements on BLMs consisting of binary lipid mixtures were conducted for the first time. Preliminary results presented within this thesis indicate that the theory seems to be right, but more experimental evidence has to be collected in future experiments.
A new protocol to extract the gel/fluid area domain ratios from 3D GUVs images composed of binary lipid mixtures was introduced. It was shown that the preliminary data fit the values expected from ideal solution theory well. This is of great importance for future experiments, as it indicates that the domains displayed on GUVs can be treated as thermodynamic phases.

However, this preliminary study suffers from basic experimental problems. The technique is of great importance for the investigation of GUVs as model systems, as it allows quantitative analysis of what has been inspected only visually yet. This is a great aspect for the future investigation of free standing lipid bilayers.
The GUV experiments indicate that the domain boundaries are very peculiar regions. Monte Carlo simulations show that fluctuations at the domain interfaces are strongest and a high membrane permeability was assigned to these regions [73, 217]. The domain boundaries did not gain much attention in the past, but I think that they have to be taken into account stronger in the future. The peculiar properties of the domain interfaces could be of great importance for biological systems.

This thesis also demonstrates clearly that it is of vital importance to apply several techniques to the lipid systems of interest, as fine aspects might get lost due to the limited resolution of experimental setups. Onesided investigation with a single technique can easily lead to a misinterpretation. This occurred in the interpretation of Massey's spectroscopic data [112]. He concluded that no phase separation is present in POPC/ceramide lipid membranes. The application of several techniques, such as Confocal Fluorescence Microscopy, Two Photon Microscopy, Differential Scanning Calorimetry and Fourier Transform Infra Red spectroscopy demonstrated the contrary. Gel/fluid phase separation on the macroscopic scale was observed in this case.
In the case of POPC/cerebrosides lipid mixtures containing high fractions of cholesterol, the existence of two liquid ordered phases was observed. The experiments presented here show that phase coexistence was observed to higher cholesterol concentrations than in an AFM and fluorescence microscopy study by Lin et al [155]. In the case of Lin et al. conclusions were drawn from fluorescence microscopy, as AFM already failed to detect the coexisting domains. However, a changed partition behavior of the fluorescent probes, due to the changed properties of the coexisting domains containing increased amounts of cholesterol, could lead to misinterpretation. In our experiments Laurdan and other fluorescent probes were still able to detect phase separation to higher cholesterol concentrations than stated by Lin et al.
Additionally, the different lipid origin was referred to be an probable factor of differences in experimental results. The purity of samples purchased at different vendors varies. This has to be kept in mind when studies are compared.

As mentioned already, this thesis clearly demonstrates that different techniques have to be applied to study our systems of interest. Most of these techniques are expensive and therefore established in a few places only. The knowledge to operate them and how to interpret the data resides with the experimental setup usually. This implicates the establishment of cooperations and a lot of traveling between different laboratories, but also the demand to the single scientist not to concentrate on one technique. A broad knowledge about several techniques and how to combine them properly is necessary.
It is also demonstrated that the information which can be gained from theoretical simulations and predictions is of invaluable importance for the interpretation of experimental data.

Within the framework of this thesis, several techniques were made usable at the University of Southern Denmark in Odense and the Niels Bohr Institute in Copenhagen. These techniques will contribute strongly to the ongoing research in these institutions.

Appendix A

Abbreviations

AFM	Atomic Force Microscopy
BLM	Black Lipid Membrane
Bodipy	β-BODIPY®FL C_5-HPC
chol	Cholesterol
CFLSM	Confocal Fluorescence Laser Scanning Microscopy
CTB	Cholera Toxin B Subunit
DiI-C_{18}	$DiIC_{18}(3)$
dDMPC-d54	1,2-Dimyristoyl-D54-sn-Glycero-3-Phosphocholine
DLPC	1,2-Dilauroyl-sn-Glycero-3-Phosphocholine
DMPC	1,2-Dimyristoyl-sn-Glycero-3-Phosphocholine
DOPC	1,2-Dioleoyl-sn-Glycero-3-Phosphocholine
DPH	1,6-diphenyl-1,3,5-hexatriene (DPH)
dPOPC-d31	1-Palmitoyl(D31)-2-Oleoyl-sn-Glycero-3-Phosphocholine
DPPC	1,2-Dipalmitoyl-sn-Glycero-3-Phosphocholine
DSC	Differential Scanning Calorimetry
DSPC	1,2-Distearoyl-sn-Glycero-3-Phosphocholine
FCS	Fluorescence Correlation Spectroscopy
FTIR	Fourier Transform Infra Red Spectroscopy
FRET	Förster Resonance Energy Transfer
GalCer	Cerebrosides
G_{M1}	Ganglioside
GP	Generalized Polarisation
GUV	Giant Unilamellar Vesicle
ITO	Indium Tin Oxide
Laurdan	6-dodecanoyl-2-dimethylaminonaphthalene
LUV	Large Unilamellar Vesicle
NMR	Nuclear Magnetic Resonance
PEG	Polyethylene Glycol
PLA_2	Phospholipase A_2
POPC	1-Palmitoyl-2-Oleoyl-sn-Glycero-3-Phosphocholine
PSF	Point Spread Funcition
SC	Stratum Corneum
STED	Stimulated Emission Depletion

SUV	Small Unilamellar Vesicle
TFE	Trifluoroethanol
TPM	Two Photon Microscopy

Bibliography

[1] **Adam, G.** and **M. Delbrück** (1968). *Structural Chemistry in Molecular Biology*, chapter Reduction of Dimensionality in Biological Space. Freeman, San Francisco, pages 198–215.

[2] **Gennis, R.** (1989). *Molecular Structure and Function*. Springer.

[3] **Janiak, M. J.**, **D. M. Small** and **G. G. Shipley** (1979). Temperature and compositional dependence of the structure of hydrated dimyristoyl lecithin. *J. Biol. Chem.* 254:6068–6078.

[4] **Koynova, R.** and **M. Caffrey** (1994). Phases and phase transitions of the hydrated phosphatidylethanolamines. *Chem. Phys. Lipids* 69:1–34.

[5] **Koynova, R.** and **M. Caffrey** (1995). Phases and phase transitions of the sphingolipids. *Biochim. Biophys. Acta - Lipids Lipid Met.* 1255:213–236.

[6] **Koynova, R.** and **M. Caffrey** (1998). Phases and phase transitions of the phosphatidylcholines. *Biochim. Biophys. Acta - Reviews on Biomembranes* 1376:91–145.

[7] **Tokumasu, F.**, **A. J. Jin**, **G. W. Feigenson** and **J. A. Dvorak** (2003). Nanoscopic Lipid Domain Dynamics Revealed by Atomic Force Microscopy. *Biophys. J.* 84:2609–2618.

[8] **Burns, A.** (2003). Domain Structure in Model Membrane Bilayers Investigated by Simultaneous Atomic Force Microscopy and Fluorescence Imaging. *Langmuir* 19:8358–8363.

[9] **Papahadjopoulos, D.**, **K. Jacobson**, **S. Nir** and **I. Isac** (1973). Phase transitions in phospholipid vesicles. Fluorescence polarization and permeability measurements concerning the effect of temperature and cholesterol. *Biochim. Biophys. Acta - Biomembranes* 311:330–348.

[10] **Halstenberg, S.**, **T. Heimburg**, **T. Hianik**, **U. Kaatze** and **R. Krivanek** (1998). Cholesterol-Induced Variations in the Volume and Enthalpy Fluctuations of Lipid Bilayers. *Biophys. J.* 75:264–271.

[11] **Heimburg, T.** (1998). Mechanical aspects of membrane thermodynamics. Estimation of the mechanical properties of lipid membranes close to the chain melting transition from calorimetry. *Biochim. Biophys. Acta - Biomembranes* 1415:147–162.

[12] **Ivanova, V. P.**, **I. M. Makarov**, **T. E. Schaffer** and **T. Heimburg** (2003). Analyzing Heat Capacity Profiles of Peptide-Containing Membranes: Cluster Formation of Gramicidin A. *Biophys. J.* 84:2427–2439.

[13] **Veatch, S. L.** and **S. L. Keller** (2005). Seeing spots: Complex phase behavior in simple membranes. *Biochim. Biophys. Acta - Mol. Cell Res.* 1746:172–185.

[14] **de la Serna, B. J.**, **J. Perez-Gil**, **A. C. Simonsen** and **L. A. Bagatolli** (2004). Cholesterol Rules: Direct Observation of the Coexistence of Two Fluid Phases in Native Pulmonary Surfactant Membranes at Physiological Temperatures. *J. Biol. Chem.* 279:40715–40722.

[15] **Ipsen, J.**, **G. Karlstrom**, **O. G. Mourtisen**, **H. Wennerstrom** and **M. J. Zuckermann** (1987). Phase equilibria in the phosphatidylcholine-cholesterol system. *Biochim. Biophys. Acta - Biomembranes* 905:162–172.

[16] **Huang, J.** and **G. W. Feigenson** (1999). A Microscopic Interaction Model of Maximum Solubility of Cholesterol in Lipid Bilayers. *Biophys. J.* 76:2142–2157.

[17] **Singer, S. J.** and **G. L. Nicolson** (1972). The Fluid Mosaic Model of the Structure of Cell Membranes. *Science* 175:720–731.

[18] **Steim, J. M.**, **M. E. Tourtellotte**, **J. C. Reinert**, **R. N. McElhaney** and **R. L. Rader** (1969). Calorimetric Evidence for the Liquid-Crystalline State of Lipids in a Biomembrane. *Proc .Natl. Acad. Sci. USA* 63:104–109.

[19] **Reinert, J. C.** and **J. M. Steim** (1970). Calorimetric Detection of a Membrane-Lipid Phase Transition in Living Cells. *Science* 168:1580–1582.

[20] **Hinz, H.-J.** and **J. M. Sturtevant** (1972). Calorimetric Studies of Dilute Aqueous Suspensions of Bilayers Formed from Synthetic l-agr-Lecithins. *J. Biol. Chem.* 247:6071–6075.

[21] **Melchior, D. L.** and **J. M. Steim** (1976). Thermotropic Transitions in Biomembranes. *Annu. Rev. Biophys. Bio.* 5:205–238.

[22] **Mabrey, S.** and **J. M. Sturtevant** (1976). Investigation of Phase Transitions of Lipids and Lipid Mixtures by High Sensitivity Differential Scanning Calorimetry. *Proc .Natl. Acad. Sci. USA* 73:3862–3866.

[23] **Jackson, M. B.** and **J. M. Sturtevant** (1977). Studies of the lipid phase transitions of Escherichia coli by high sensitivity differential scanning calorimetry. *J. Biol. Chem.* 252:4749–4751.

[24] **Jain, M.** and **H. White** (1977). Long-range order in biomembranes. *Adv. Lipid Res.* 15:1–60.

[25] **Mouritsen, O. G.** and **M. Bloom** (1984). Mattress model of lipid-protein interactions in membranes. *Biophys. J.* 46:141–153.

[26] **Grainger, D. W.**, **A. Reichert**, **H. Ringsdorf** and **C. Salesse** (1989). An enzyme caught in action: Direct imaging of hydrolytic function and domain formation of phospholipase A_2 in phosphatidylcholine monolayers. *FEBS Letters* 252:73–82.

[27] **Meller, P.**, **R. Peters** and **H. Ringsdorf** (1989). Microstructure and lateral diffusion in monolayers of polymerizable amphiphiles. *Colloid Polym. Sci.* 267:97–107.

[28] **Korlach, J.**, **P. Schwille**, **W. W. Webb** and **G. W. Feigenson** (1999). Characterization of lipid bilayer phases by confocal microscopy and fluorescence correlation spectroscopy. *P. Natl. Acad. Sci. USA* 96:8461–8466.

[29] **Bagatolli, L. A.** and **E. Gratton** (1999). Two-Photon Fluorescence Microscopy Observation of Shape Changes at the Phase Transition in Phospholipid Giant Unilamellar Vesicles. *Biophys. J.* 77:2090–2101.

[30] **Dumas, F.**, **M. C. Lebrun** and **J.-F. Tocanne** (1999). Is the protein/lipid hydrophobic matching principle relevant to membrane organization and functions? *FEBS Letters* 458:271–277.

[31] **Lichtenberg, D.**, **G. Romero**, **M. Menashe** and **R. Biltonen** (1986). Hydrolysis of dipalmitoylphosphatidylcholine large unilamellar vesicles by porcine pancreatic phospholipase A_2. *J. Biol. Chem.* 261:5334–5340.

[32] **Simons, K.** and **E. Ikonen** (1997). Functional rafts in cell membranes. *Nature* 387:569–572.

[33] **Jacobson, K.** and **C. Dietrich** (1999). Looking at lipid rafts? *Trends Cell Biol.* 9:87–91.

[34] **Bagatolli, L. A.** and **E. Gratton** (2000). A Correlation between Lipid Domain Shape and Binary Phospholipid Mixture Composition in Free Standing Bilayers: A Two-Photon Fluorescence Microscopy Study. *Biophys. J.* 79:434–447.

[35] **Gliss, C.**, **H. Clausen-Schaumann**, **R. Gunther**, **S. Odenbach**, **O. Randl** and **T. Bayerl** (1998). Direct Detection of Domains in Phospholipid Bilayers by Grazing Incidence Diffraction of Neutrons and Atomic Force Microscopy. *Biophys. J.* 74:2443–2450.

[36] **Loura, L.**, **A. Fedorov** and **M. Prieto** (2000). Membrane Probe Distribution Heterogeneity: A Resonance Energy Transfer Study. *J. Phys. Chem. B* 104:6920–6931.

[37] **Lagerholm, B. C.**, **G. E. Weinreb**, **K. Jacobson** and **N. L. Thompson** (2005). Detecting Microdomains in Intact Cell Membranes. *Annu. Rev. Phys. Chem.* 56:309–336.

[38] **Bouwstra, J. A.**, **P. L. Honeywell-Nguyen**, **G. S. Gooris** and **M. Ponec** (2003). Structure of the Skin Barrier and its Modulation by Vesicular Formulations. *Prog. Lipid Res.* 42:1–36.

[39] **Ongpipattanakul, B.**, **M. L. Francoeur** and **R. O. Potts** (1994). Polymorphism in stratum corneum lipids. *Biochim. Biophys. Acta - Biomembranes* 1190:115–122.

[40] **Gay, C. L.**, **R. H. Guy**, **G. M. Golden**, **V. H. Mak** and **M. L. Francoeur** (1994). Characterization of Low-Temperature (i.e. < 65°C) Lipid Transitions in Human Strateum Corneum. *J. Invest. Dermatol.* 103:233–239.

[41] **Bouwstra, J.**, **G. Gooris**, **W. Bras** and **D. Downing** (1995). Lipid organization in pig stratum corneum. *J. Lipid Res.* 36:685–695.

[42] **Walters, K.** and **J. Hadgraft** (1993). *Pharmaceutical skin penetration enhancement*. Marcel Dekker, New York.

[43] **Hope, M.** and **C. Kitson** (1993). Liposomes. A perspective for dermatologists. *Dermatol. Clin.* 11:143–154.

[44] **Guy, R.**, **M. Delgado-Charro** and **Y. Kalia** (2001). Iontophoretic Transport across the Skin. *Skin Pharmacol. Appl. Skin Physiol.* 14:35–40.

[45] **Vanbever, R.** and **V. Preat** (1999). In vivo efficacy and safety of skin electroporation. *Adv. Drug Deliver. Rev.* 35:77–88.

[46] **Sparr, E.** and **H. Wennerström** (2001). Responding Phospholipid Membranes—Interplay between Hydration and Permeability. *Biophys. J.* 81:1014–1028.

[47] **Hodgkin, A. L.** and **A. F. Huxley** (1952). A quantitative description of membrane current and its application to conduction and excitation in nerve. *J. Physiol.* 117:500–544.

[48] **Heimburg, T.** and **A. D. Jackson** (2005). On soliton propagation in biomembranes and nerves. *Proc .Natl. Acad. Sci. USA* 102:9790–9795.

[49] **Melo, E. C.**, **I. M. Lourtie**, **M. B. Sankaram**, **T. E. Thompson** and **W. L. Vaz** (1992). Effects of domain connection and disconnection on the yields of in-plane bimolecular reactions in membranes. *Biophys. J.* 63:1506–1512.

[50] **Vaz, W. L. C.** and **P. F. F. Almeida** (1993). Phase topology and percolation in multi-phase lipid bilayers: is the biological membrane a domain mosaic? *Curr. Opin. Struc. Biol.* 3:482–488.

[51] **Salinas, D. G.**, **M. De La Fuente** and **J. G. Reyes** (2005). Changes of Enzyme Activity in Lipid Signaling Pathways Related to Substrate Reordering. *Biophys. J.* 89:885–894.

[52] **Lee, A. G.** (1977). Lipid phase transitions and phase diagrams II. Mixtures involving lipids. *Biochim. Biophys. Acta - Rev. Biomem.* 472:285–344.

[53] **Feigenson, G. W.** (2007). Phase Boundaries and Biological Membranes. *Annu. Rev. Bioph. Biom.* 36:63–77.

[54] **Feigenson, G. W.** and **J. T. Buboltz** (2001). Ternary Phase Diagram of Dipalmitoyl-PC/Dilauroyl-PC/Cholesterol: Nanoscopic Domain Formation Driven by Cholesterol. *Biophys. J.* 80:2775–2788.

[55] **de Almeida, R. F.**, **L. M. Loura**, **A. Fedorov** and **M. Prieto** (2005). Lipid Rafts have Different Sizes Depending on Membrane Composition: A Time-resolved Fluorescence Resonance Energy Transfer Study. *J. Mol. Biol.* 346:1109–1120.

[56] **Elliott, R.**, **I. Szleifer** and **M. Schick** (2006). Phase Diagram of a Ternary Mixture of Cholesterol and Saturated and Unsaturated Lipids Calculated from a Microscopic Model. *Phys. Rev. Lett.* 96:098101–4.

[57] **Komura, S.**, **H. Shirotori** and **P. D. Olmsted** (2005). Phase behaviour of three-component lipid mixtures. *J. Phys. Condens. Mat.* 17:S2951–S2956.

[58] **Doniach, S.** (1978). Thermodynamic fluctuations in phospholipid bilayers. *J. Chem. Phys.* 68:4912–4916.

[59] **Pink, D. A.**, **T. J. Green** and **D. Chapman** (1980). Raman scattering in bilayers of saturated phosphatidylcholines. Experiment and theory. *Biochemistry* 19:349–356.

[60] **Sperotto, M. M.** and **O. G. Mouritsen** (1991). Monte Carlo simulation studies of lipid order parameter profiles near integral membrane proteins. *Biophys. J.* 59:261–270.

[61] **Jørgensen, K.**, **M. M. Sperotto**, **O. G. Mouritsen**, **J. H. Ipsen** and **M. J. Zuckermann** (1993). Phase equilibria and local structure in binary lipid bilayers. *Biochim. Biophys. Acta - Biomembranes* 1152:135–145.

[62] **Jørgensen, K.** and **O. G. Mouritsen** (1995). Phase separation dynamics and lateral organization of two-component lipid membranes. *Biophys. J.* 69:942–954.

[63] **Sugár, I. P.**, **R. L. Biltonen** and **N. Mitchard** (1994). Monte Carlo simulations of membranes: Phase transition of small unilamellar dipalmitoylphosphatidylcholine vesicles. In **M. L. Johnson** and **L. Brand**, editors, *Part B: Numerical Computer Methods*, volume Volume 240. Academic Press, pages 569–593.

[64] **Jerala, R.**, **P. F. Almeida** and **R. L. Biltonen** (1996). Simulation of the gel-fluid transition in a membrane composed of lipids with two connected acyl chains: application of a dimer-move step. *Biophys. J.* 71:609–615.

[65] **Sugár, I. P.**, **T. E. Thompson** and **R. L. Biltonen** (1999). Monte Carlo Simulation of Two-Component Bilayers: DMPC/DSPC Mixtures. *Biophys. J.* 76:2099–2110.

[66] **Heimburg, T.** and **R. L. Biltonen** (1996). A Monte Carlo simulation study of protein-induced heat capacity changes and lipid-induced protein clustering. *Biophys. J.* 70:84–96.

[67] **Hac, A. E.**, **H. M. Seeger**, **M. Fidorra** and **T. Heimburg** (2005). Diffusion in Two-Component Lipid Membranes–A Fluorescence Correlation Spectroscopy and Monte Carlo Simulation Study. *Biophys. J.* 88:317–333.

[68] **Seeger, H.** (2006). *Kinetics of Domain Formation in Lipid Membranes*. Ph.D. thesis, University of Göttingen.

[69] **Biltonen, R. L.** (1990). A statistical-thermodynamic view of cooperative structural changes in phospholipid bilayer membranes: their potential role in biological function. *J. Chem. Thermodyn.* 22:1–19.

[70] **Glauber, R. J.** (1963). Time-Dependent Statistics of the Ising Model. *J. Math. Phys.* 4:294–307.

[71] **Hill, T.** (1962). *Introduction to Statistical Thermodynamics*. Addison-Wesley.

[72] **Kubo, R.** (1966). The fluctuation-dissipation theorem. *Rep. Prog. Phys.* 29:255–284.

[73] **Cruzeiro-Hansson, L.** and **O. G. Mouritsen** (1988). Passive ion permeability of lipid membranes modelled via lipid-domain interfacial area. *Biochim. Biophys. Acta - Biomembranes* 944:63–72.

[74] **Nielsen, L. K.**, **T. Bjornholm** and **O. G. Mouritsen** (2000). Critical phenomena: Fluctuations caught in the act. *Nature* 404:352–352.

[75] **Anthony, F. H.**, **R. L. Biltonen** and **E. Freire** (1981). Modification of a vibrating-tube density meter for precise temperature scanning. *Anal. Biochem.* 116:161–167.

[76] **Nagle, J. F.** and **H. L. Scott** (1978). Lateral compressibility of lipid mono- and bilayers. Theory of membrane permeability. *Biochim. Biophys. Acta - Biomembranes* 513:236–243.

[77] **Antonov, V. F.**, **A. A. Anosov**, **V. P. Norik** and **E. Y. Smirnova** (2005). Soft Perforation of Planar Bilayer Lipid Membranes of Dipalmitoylphosphatidylcholine at the Temperature of the Phase Transition from the Liquid Crystalline to the Gel State. *Eur. Biophys. J.* 34:155.

[78] **Antonov, V. F.**, **E. V. Shevchenko**, **E. T. Kozhomkulov**, **A. A. Mol'nar** and **E. Y. Smirnova** (1985). Capacitive and ionic currents in BLM from phosphatidic acid in Ca^{2+}-induced phase transition. *Biochem. Biophys. Res. Comm.* 133:1098–1103.

[79] **Freeman, S. A.**, **M. A. Wang** and **J. C. Weaver** (1994). Theory of electroporation of planar bilayer membranes: predictions of the aqueous area, change in capacitance, and pore-pore separation. *Biophys. J.* 67:42–56.

[80] **Gurtovenko, A. A.** and **I. Vattulainen** (2007). Ion Leakage through Transient Water Pores in Protein-Free Lipid Membranes Driven by Transmembrane Ionic Charge Imbalance. *Biophys. J.* 92:1878–1890.

[81] **Fidorra, M.**, **L. Duelund**, **C. Leidy**, **A. C. Simonsen** and **L. A. Bagatolli** (2006). Absence of Fluid-Ordered/Fluid-Disordered Phase Coexistence in Ceramide/POPC Mixtures Containing Cholesterol. *Biophys. J.* 90:4437–4451.

[82] **Angelova, M. I.** and **D. S. Dimitrov** (1986). Liposome electroformation. *Faraday Discuss. Chem. Soc.* 81:303–311.

[83] **Angelova, M.** and **D. Dimitrov** (1988). A mechanism of liposome electroformation. *Progr. Coll. Pol. Sci.* 76:59–67.

[84] **Lasic, D. D.** (1988). The mechanism of vesicle formation. *Biochem. J.* 256:1–11.

[85] **Winterhalter, M.** and **D. D. Lasic** (1993). Liposome stability and formation: Experimental parameters and theories on the size distribution. *Chem. Phys. Lipids* 64:35–43.

[86] **Montal, M.** and **P. Mueller** (1972). Formation of Bimolecular Membranes from Lipid Monolayers and a Study of their Electrical Properties. *P. Natl. Acad. Sci. USA* 69:3561–3566.

[87] **Sandison, M. E.**, **M. Zagnoni**, **M. Abu-Hantash** and **H. Morgan** (2007). Micromachined glass apertures for artificial lipid bilayer formation in a microfluidic system. *J. Micromech. Microeng.* 17:S189–S196.

[88] **Simonsen, A.** and **L. Bagatolli** (2004). Structure of Spin-Coated Lipid Films and Domain Formation in Supported Membranes Formed by Hydration. *Langmuir* 20:9720–9728.

[89] **Kass, M.**, **A. Witkin** and **D. Terzopoulos** (1988). Snakes: Active contour models. *International Journal of Computer Vision* 1:321–331.

[90] **Ahlberg, J.** (1996). *Active Contours in Three Dimensions*. Master's thesis, Linköping University.

[91] **Göppert-Mayer, M.** (1931). Über Elementarakte mit zwei Quantensprüngen. *Ann. Phys.* 401:273–294.

[92] **Bagatolli, L. A.** and **E. Gratton** (2001). Direct Observation of Lipid Domains in Free-Standing Bilayers Using Two-Photon Excitation Fluorescence Microscopy. *J. Fluoresc.* 11:141–160.

[93] **Stelzer, E. H. K.**, **S. Hell**, **S. Lindek**, **R. Stricker**, **R. Pick**, **C. Storz**, **G. Ritter** and **N. Salmon** (1994). Nonlinear absorption extends confocal fluorescence microscopy into the ultra-violet regime and confines the illumination volume. *Opt. Commun.* 104:223–228.

[94] **Hell, S.** and **E. H. K. Stelzer** (1992). Fundamental improvement of resolution with a 4Pi-confocal fluorescence microscope using two-photon excitation. *Opt. Commun.* 93:277–282.

[95] **Parasassi, T.**, **E. K. Krasnowska**, **L. A. Bagatolli** and **E. Gratton** (1998). Laurdan and Prodan as Polarity-Sensitive Fluorescent Membrane Probes. *J. Fluoresc.* 4:365–373.

[96] **Parasassi, T.**, **G. De Stasio**, **A. d'Ubaldo** and **E. Gratton** (1990). Phase fluctuation in phospholipid membranes revealed by Laurdan fluorescence. *Biophys. J.* 57:1179–1186.

[97] **Leidy, C.**, **W. F. Wolkers**, **K. Jørgensen**, **O. G. Mouritsen** and **J. H. Crowe** (2001). Lateral Organization and Domain Formation in a Two-Component Lipid Membrane System. *Biophys. J.* 80:1819–1828.

[98] **Kolesnick, R. N.**, **F. M. Goni** and **A. Alonso** (2000). Compartmentalization of Ceramide Signaling: Physical Foundations and Biological Effects. *J. Cell. Physiol.* 184:285–300.

[99] **Carrer, D. C.** and **B. Maggio** (2001). Transduction to self-assembly of molecular geometry and local interactions in mixtures of ceramides and ganglioside GM1. *Biochim. Biophys. Acta - Biomembranes* 1514:87–99.

[100] **Li, L.**, **X. Tang**, **K. G. Taylor**, **D. B. DuPre** and **M. C. Yappert** (2002). Conformational Characterization of Ceramides by Nuclear Magnetic Resonance Spectroscopy. *Biophys. J.* 82:2067–2080.

[101] **Squier, C. A.**, **P. Cox** and **P. W. Wertz** (1991). Lipid Content and Water Permeability of Skin and Oral Mucosa. *J. Invest. Dermatol.* 96:123–126.

[102] **Lesch, C. A.**, **C. A. Squier**, **A. Cruchley**, **D. M. Williams** and **P. Speight** (1989). The Permeability of Human Oral Mucosa and Skin to Water. *J. Dent. Res.* 68:1345–1349.

[103] **Wertz, P. W.**, **D. C. Schwartzendruber**, **K. C. Madison** and **D. T. Downing** (1987). Composition and Morphology of Epidermal Cyst Lipids. *J. Investig. Dermatol.* 89:419–425.

[104] **Elias, P. M.** and **D. S. Friend** (1975). The Permeability Barrier in Mammalian Epidermis. *J. Cell. Biol.* 65:180–191.

[105] **Wertz, P. W.** and **D. T. Downing** (1983). Ceramides of Pig Epidermis: Structure Determination. *J. Lipid Res.* 24:759–765.

[106] **van Blitterswijk, W. J.**, **A. H. van der Luit**, **R. J. Veldman**, **M. Verheij** and **J. Borst** (2003). Ceramide: second messenger or modulator of membrane structure and dynamics? *Biochem. J.* 369:199–211.

[107] **Siskind, L. J.** and **M. Colombini** (2000). The Lipids C_2- and C_{16}-Ceramide Form Large Stable Channels. Implications for Apoptosis. *J. Biol. Chem.* 275:38640–38644.

[108] **Siskind, L. J.**, **R. N. Kolesnick** and **M. Colombini** (2002). Ceramide Channels Increase the Permeability of the Mitochondrial Outer Membrane to Small Proteins. *J. Biol. Chem.* 277:26796–26803.

[109] **Holopainen, J. M.**, **J. Y. A. Lehtonen** and **P. K. J. Kinnunen** (1997). Lipid microdomains in dimyristoylphosphatidylcholine-ceramide liposomes. *Chem. Phys. Lipids* 88:1–13.

[110] **Holopainen, J.**, **M. Subramanian** and **P. Kinnunen** (1998). Sphingomyelinase Induces Lipid Microdomain Formation in a Fluid Phosphatidylcholine/Sphingomyelin Membrane. *Biochemistry* 37:17562–17570.

[111] **Carrer, D. C.** and **B. Maggio** (1999). Phase behavior and molecular interactions in mixtures of ceramide with dipalmitoylphosphatidylcholine. *J. Lipid Res.* 40:1978–1989.

[112] **Massey, J. B.** (2001). Interaction of ceramides with phosphatidylcholine, sphingomyelin and sphingomyelin/cholesterol bilayers. *Biochim. Biophys. Acta - Biomembranes* 1510:167–184.

[113] **Hsueh, Y.-W.**, **R. Giles**, **N. Kitson** and **J. Thewalt** (2002). The Effect of Ceramide on Phosphatidylcholine Membranes: A Deuterium NMR Study. *Biophys. J.* 82:3089–3095.

[114] **Megha** and **E. London** (2004). Ceramide Selectively Displaces Cholesterol from Ordered Lipid Domains (Rafts): Implication for Lipid Raft Structure and Function. *J. Biol. Chem.* 279:9997–10004.

[115] **Holopainen, J. M.**, **M. I. Angelova** and **P. K. J. Kinnunen** (2000). Vectorial Budding of Vesicles by Asymmetrical Enzymatic Formation of Ceramide in Giant Liposomes. *Biophys. J.* 78:830–838.

[116] **Milhiet, P. E.**, **V. Vié**, **M.-C. Giocondi** and **C. L. Grimellec** (2001). AFM Characterization of Model Rafts in Supported Bilayers. *Single Mol.* 2:109–112.

[117] **Giocondi, M.-C.**, **V. Vie**, **E. Lesniewska**, **P.-E. Milhiet**, **M. Zinke-Allmang** and **C. Le Grimellec** (2001). Phase Topology and Growth of Single Domains in Lipid Bilayers. *Langmuir* 17:1653–1659.

[118] **Curatolo, W.** (1986). The interactions of 1-palmitoyl-2-oleylphosphatidylcholine and bovine brain cerebroside. *Biochim. Biophys. Acta - Biomembranes* 861:373–376.

[119] **Guard-Friar, D.**, **C. H. Chen** and **A. S. Engle** (1985). Deuterium isotope effect on the stability of molecules: phospholipids. *J. Phys. Chem.* 89:1810–1813.

[120] **Wang, G.** and **C.-H. Chen** (1993). Thermodynamic Elucidation of Structural Stability of Deuterated Biological Molecules: Deuterated Phospholipid Vesicles in H_2O. *Arch. Biochem. Biophys.* 301:330–335.

[121] **Bagatolli, L. A.** (2004). Direct Observation of Lipid Domains in Free Standing Bilayers. *Chem. Phys. Lipids* 122:137–145.

[122] **Jameson, D. M.** and **W. H. Sawyer** (1995). Fluorescence anisotropy applied to biomolecular interactions. In **K. Sauer**, editor, *Biochemical Spectroscopy*, volume Volume 246. Academic Press, pages 283–300.

[123] **Weber, G.** (1952). Polarization of the Fluorescence of Macromolecules. *Biochem. J.* 51:145–155.

[124] **Huang, H.-W.**, **E. M. Goldberg** and **R. Zidovetzki** (1999). Ceramides Modulate Protein Kinase C Activity and Perturb the Structure of Phosphatidylcholine/Phosphatidylserine Bilayers. *Biophys. J.* 77:1489–1497.

[125] **Dietrich, C.**, **L. A. Bagatolli**, **Z. N. Volovyk**, **N. L. Thompson**, **M. Levi**, **K. Jacobson** and **E. Gratton** (2001). Lipid Rafts Reconstituted in Model Membranes. *Biophys. J.* 80:1417–1428.

[126] **Maulik, P. R.** and **G. G. Shipley** (1996). Interactions of N-stearoyl sphingomyelin with cholesterol and dipalmitoylphosphatidylcholine in bilayer membranes. *Biophys. J.* 70:2256–2265.

[127] **Saslowsky, D. E.**, **J. Lawrence**, **X. Ren**, **D. A. Brown**, **R. M. Henderson** and **J. M. Edwardson** (2002). Placental Alkaline Phosphatase Is Efficiently Targeted to Rafts in Supported Lipid Bilayers. *J. Biol. Chem.* 277:26966–26970.

[128] **Chiantia, S.**, **N. Kahya**, **J. Ries** and **P. Schwille** (2006). Effects of Ceramide on Liquid-Ordered Domains Investigated by Simultaneous AFM and FCS. *Biophys. J.* 90:4500–4508.

[129] **Siskind, L. J.**, **A. Davoody**, **N. Lewin**, **S. Marshall** and **M. Colombini** (2003). Enlargement and Contracture of C_2-Ceramide Channels. *Biophys. J.* 85:1560–1575.

[130] **Pascher, I.** (1976). Molecular arrangements in sphingolipids Conformation and hydrogen bonding of ceramide and their implication on membrane stability and permeability. *Biochim. Biophys. Acta - Biomembranes* 455:433–451.

[131] **Leidy, C.**, **L. Linderoth**, **T. L. Andresen**, **O. G. Mouritsen**, **K. Jørgensen** and **G. H. Peters** (2006). Domain-Induced Activation of Human Phospholipase A_2 Type IIA: Local versus Global Lipid Composition. *Biophys. J.* 90:3165–3175.

[132] **Quist, A.**, **A. Chand**, **S. Ramachandran**, **C. Daraio**, **S. Jin** and **R. Lal** (2007). Atomic Force Microscopy Imaging and Electrical Recording of Lipid Bilayers Supported over Microfabricated Silicon Chip Nanopores: Lab-on-a-Chip System for Lipid Membranes and Ion Channels. *Langmuir* 23:1375–1380.

[133] **Norton, W. T.**, **T. Abe**, **S. E. Poduslo** and **G. H. DeVries** (1975). The lipid composition of isolated brain cells and axons. *J. Neurosci. Res.* 1:57–75.

[134] **Chen, Y. Q.**, **M. A. Rafi**, **G. de Gala** and **D. A. Wenger** (1993). Cloning and expression cDNA encoding human galactocerebrosidase, the enzyme deficient in globoid cell leukodystrophy. *Hum. Mol. Genet.* 2:1841–1846.

[135] **Hansson, G. C.** (1983). The subcellular localization of the glycosphingolipids in the epithelial cells of rat small intestine. *Biochim. Biophys. Acta - Biomembranes* 733:295–299.

[136] **Hauser, H.**, **K. Howell**, **R. M. C. Dawson** and **D. E. Bowyer** (1980). Rabbit small intestinal brush border membrane. Preparation and lipid composition. *Biochim. Biophys. Acta - Biomembranes* 602:567–577.

[137] **Tan, R. X.** and **J. H. Chen** (2003). The cerebrosides. *Nat. Prod. Rep.* 20:509–534.

[138] **Pascher, I.** and **S. Sundell** (1977). Molecular arrangements in sphingolipids. The crystal structure of cerebroside. *Chem. Phys. Lipids* 20:175–191.

[139] **Johnson, A.**, **A. McNabb** and **R. Rossiter** (1948). Lipids of normal brain. *Biochem. J.* 43:573.

[140] **P. Morell, W. N., R. Quarles** (1999). *Basic Neurochemistry*. Lippincott-Raven, New York, 6th edition.

[141] **Bosio, A.**, **E. Binczek** and **W. Stoffel** (1996). Functional breakdown of the lipid bilayer of the myelin membrane in central and peripheral nervous systemby disrupted galactocerebroside synthesis. *Proc .Natl. Acad. Sci. USA* 93:13280–13285.

[142] **Coetzee, T.**, **N. Fujita**, **J. Dupree**, **R. Shi**, **A. Blight**, **K. Suzuki**, **K. Suzuki** and **B. Popko** (1996). Myelination in the Absence of Galactocerebroside and Sulfatide: Normal Structure with Abnormal Function and Regional Instability. *Cell* 86:209–219.

[143] **Bosio, A.**, **E. Binczek**, **W. F. Haupt** and **W. Stoffel** (1998). Composition and Biophysical Properties of Myelin Lipid Define the Neurological Defects in Galactocerebroside- and Sulfatide-Deficient Mice. *J. Neurochem.* 70:308–315.

[144] **Suzuki, K.** (1998). Twenty Five Years of the "Psychosine Hypothesis": A Personal Perspective of its History and Present Status. *Neurochem. Res.* 23:251–259.

[145] **Suzuki, K.**, **M. T. Vanier** and **K. Suzuki** (1998). Induced Mouse Models of Abnormal Sphingolipid Metabolism. *J. Biochem.* 124:8–19.

[146] **Eto, Y.**, **K. Suzuki** and **K. Suzuki** (1970). Globoid cell leukodystrophy (Krabbe's disease): isolation of myelin with normal glycolipid composition. *J. Lipid Res.* 11:473–479.

[147] **Suzuki, K.** and **Y. Suzuki** (1970). Globoid Cell Leucodystrophy (Krabbe's Disease): Deficiency of Galactocerebroside beta -galactosidase. *Proc .Natl. Acad. Sci. USA* 66:302–309.

[148] **Beier, U. H.** and **T. Görögh** (2005). Implications of galactocerebrosidase and galactosylcerebroside metabolism in cancer cells. *Int. J. Cancer* 115:6–10.

[149] **Blanchette, C. D.**, **W.-C. Lin**, **T. V. Ratto** and **M. L. Longo** (2006). Galactosylceramide Domain Microstructure: Impact of Cholesterol and Nucleation/Growth Conditions. *Biophys. J.* 90:4466–4478.

[150] **Bunow, M. R.** (1979). Two gel states of cerebrosides calorimetric and raman spectroscopic evidence. *Biochim. Biophys. Acta - Lipid Lipid Met.* 574:542–546.

[151] **Maggio, B.**, **T. Ariga**, **J. M. Sturtevant** and **R. K. Yu** (1985). Thermotropic behavior of binary mixtures of diplamitoylphosphatidylcholine and glycosphingolipids in aqueous dispersions. *Biochim. Biophys. Acta - Biomembranes* 818:1–12.

[152] **Saxena, K.**, **R. I. Duclos**, **P. Zimmermann**, **R. R. Schmidt** and **G. G. Shipley** (1999). Structure and properties of totally synthetic galacto- and gluco-cerebrosides. *J. Lipid Res.* 40:839–849.

[153] **Curatolo, W.** and **L. Neuringer** (1986). The effects of cerebrosides on model membrane shape. *J. Biol. Chem.* 261:17177–17182.

[154] **Ruocco, M. J.**, **D. Atkinson**, **D. M. Small**, **R. P. Skarjune**, **E. Oldfield** and **G. G. Shipley** (1981). X-ray diffraction and calorimetric study of anhydrous and hydrated N-(palmitoylgalactosylsphingosine cerebroside). *Biochemistry* 20:5957–5966.

[155] **Lin, W.-C.**, **C. D. Blanchette** and **M. L. Longo** (2007). Fluid-Phase Chain Unsaturation Controlling Domain Microstructure and Phase in Ternary Lipid Bilayers Containing GalCer and Cholesterol. *Biophys. J.* 92:2831–2841.

[156] **Kulkarni, K.**, **D. Snyder** and **T. McIntosh** (1999). Adhesion between Cerebroside Bilayers. *Biochemistry* 38:15264–15271.

[157] **Sugimoto, Y.**, **H. Ninomiya**, **Y. Ohsaki**, **K. Higaki**, **J. P. Davies**, **Y. A. Ioannou** and **K. Ohno** (2001). Accumulation of cholera toxin and GM1 ganglioside in the early endosome of Niemann-Pick C1-deficient cells. *PNAS* 98:12391–12396.

[158] **Mertz, J. A.**, **J. A. McCann** and **W. D. Picking** (1996). Fluorescence Analysis of Galactose, Lactose, and Fucose Interaction with the Cholera Toxin B Subunit. *Biochemical and Biophysical Research Communications* 226:140–144.

[159] **Curatolo, W.**, **B. Sears** and **L. J. Neuringer** (1985). A calorimetry and deuterium NMR study of mixed model membranes of 1-palmitoyl-2-oleylphosphatidylcholine and saturated phosphatidylcholines. *Biochim. Biophys. Acta - Biomembranes* 817:261–270.

[160] **Koster, K. L.**, **M. S. Webb**, **G. Bryant** and **D. V. Lynch** (1994). Interactions between soluble sugars and POPC (1-palmitoyl-2-oleoylphosphatidylcholine) during dehydration: vitrification of sugars alters the phase behavior of the phospholipid. *Biochim. Biophys. Acta - Biomembranes* 1193:143–150.

[161] **Lavialle, F.** and **I. W. Levin** (1980). Raman spectroscopic study of the interactions of dimyristoyl- and 1-palmitoyl-2-oleoylphosphatidylcholine liposomes with myelin proteolipid apoprotein. *Biochemistry* 19:6044–6050.

[162] **Lee, A. G.** (1978). Calculation of phase diagrams for non-ideal mixtures of lipids, and a possible non-random distribution of lipids in lipid mixtures in the liquid crystalline phase. *Biochim. Biophys. Acta - Biomembranes* 507:433–444.

[163] **Ali, M.**, **K. Cheng** and **J. Huang** (2006). Ceramide Drives Cholesterol Out of the Ordered Lipid Bilayer Phase into the Crystal Phase in 1-Palmitoyl-2-oleoyl-*sn*-glycero-3-phosphocholine/Cholesterol/Ceramide Ternary Mixtures. *Biochemistry* 45:12629–12638.

[164] **Maggio, B.** (1994). The surface behavior of glycosphingolipids in biomembranes: A new frontier of molecular ecology. *Prog. Biophys. mol. Bio.* 62:55–117.

[165] **Ali, S.**, **J. M. Smaby**, **H. L. Brockman** and **R. E. Brown** (1994). Cholesterol's interfacial interactions with galactosylceramides. *Biochemistry* 33:2900–2906.

[166] **Mocchetti, I.** (2005). Exogenous gangliosides, neuronal plasticity and repair, and the neurotrophins. *Cell. Mol. Life Sci.* 62:2283–2294.

[167] **Ceccarelli, B.**, **F. Aporti** and **M. Finesso** (1976). Effects of brain gangliosides on functional recovery in experimental regeneration and reinnervation. *Adv. Exp. Med. Biol.* 71:275.

[168] **Norlén, L.**, **I. P. Gil**, **A. Simonsen** and **P. Descouts** (2007). Human stratum corneum lipid organization as observed by atomic force microscopy on Langmuir-Blodgett films. *J. Struct. Biol.* 158:386–400.

[169] **Marr, A. G.** and **J. L. Ingraham** (1962). Effect of Temperature on the Composition of Fatty Acids in Escherichia Coli. *J. Bacteriol.* 84:1260–1267.

[170] **Johnston, N. C.** and **H. Goldfine** (1982). Effects of Growth Temperature on Fatty Acid and Alk-1-Enyl Group Compositions of Veillonella parvula and Megasphaera elsdenii Phospholipids. *J. Bacteriol.* 149:567–575.

[171] **Kleinschmidt, M. G.** and **V. A. McMahon** (1970). Effect of Growth Temperature on the Lipid Composition of Cyanidium caldarium: II. Glycolipid and Phospholipid Components. *Plant Physiol.* 46:290–293.

[172] **Sinensky, M.** (1971). Temperature Control of Phospholipid Biosynthesis in Escherichia coli. *J. Bacteriol.* 106:449–455.

[173] **Lee, A. G.** (1991). Lipids and their effects on membrane proteins: Evidence against a role for fluidity. *Prog. Lipid Res.* 30:323–348.

[174] **Sackmann, E.** (1984). Physical Basis of Trigger Processes and Membrane Structure. In *Biological Membranes*. Academic Press, pages 105–143.

[175] **Brown, D. A.** and **E. London** (1998). Functions of lipid rafts in biological membranes. *Annu. Rev. Cell Dev. Biol.* 14:111–136.

[176] **Chapman, D.** (1971). Living systems. Liquid crystalline properties of phospholipids and biological membranes. *Symp. Faraday Soc.* 5:163–174.

[177] **Träuble, H.** (1971). Phasenumwandlungen in Lipiden. Mögliche Schaltprozesse in biologischen Membranen. *Naturwissenschaften* 58:277–284.

[178] **Thompson, T. E.**, **M. B. Sankaram**, **R. L. Biltonen**, **D. Marsh** and **W. L. C. Vaz** (1995). Effects of domain structure on in-plane reactions and interactions. *Mol. Membr. Biol.* 12:157–162.

[179] **Cannon, B.**, **M. Hermansson**, **S. Gyorke**, **P. Somerharju**, **J. A. Virtanen** and **K. H. Cheng** (2003). Regulation of Calcium Channel Activity by Lipid Domain Formation in Planar Lipid Bilayers. *Biophys. J.* 85:933–942.

[180] **Bolen, E. J.** and **J. J. Sando** (1992). Effect of phospholipid unsaturation on protein kinase C activation. *Biochemistry* 31:5945–5951.

[181] **Dibble, A.**, **A. Hinderliter**, **J. Sando** and **R. Biltonen** (1996). Lipid lateral heterogeneity in phosphatidylcholine/phosphatidylserine/diacylglycerol vesicles and its influence on protein kinase C activation. *Biophys. J.* 71:1877–1890.

[182] **Orr, J. W.** and **A. C. Newton** (1992). Interaction of protein kinase C with phosphatidylserine. 1. Cooperativity in lipid binding. *Biochemistry* 31:4661–4667.

[183] **Tang, D.**, **W. L. Dean**, **D. Borchman** and **C. A. Paterson** (2006). The influence of membrane lipid structure on plasma membrane Ca2+-ATPase activity. *Cell Calcium* 39:209–216.

[184] **Mendelsohn, R.**, **R. Dluhy**, **T. Taraschi**, **D. G. Cameron** and **H. H. Mantsch** (1981). Raman and Fourier transform infrared spectroscopic studies of the interaction between glycophorin and dimyristoylphosphatidylcholine. *Biochemistry* 20:6699–6706.

[185] **Lewis, R. N.** and **R. N. McElhaney** (1993). Studies of mixed-chain diacyl phosphatidylcholines with highly asymmetric acyl chains: a Fourier transform infrared spectroscopic study of interfacial hydration and hydrocarbon chain packing in the mixed interdigitated gel phase. *Biophys. J.* 65:1866–1877.

[186] **Tamm, L.** and **S. Tatulian** (1997). Infrared spectroscopy of proteins and peptides in lipid bilayers. *Q. Rev. Biophys.* 4:365–429.

[187] **Selle, C.** and **W. Pohle** (1998). Fourier transform infrared spectroscopy as a probe for the study of the hydration of lipid self-assemblies. II. Water binding versus phase transitions. *Biospectroscopy* 4:281–294.

[188] **Mendelsohn, R.**, **G. L. Liang**, **H. L. Strauss** and **R. G. Snyder** (1995). IR spectroscopic determination of gel state miscibility in long-chain phosphatidylcholine mixtures. *Biophys. J.* 69:1987–1998.

[189] **Reinl, H.**, **T. Brumm** and **T. M. Bayerl** (1992). Changes of the physical properties of the liquid-ordered phase with temperature in binary mixtures of DPPC with cholesterol: A ^{2}H-NMR, FT-IR, DSC, and neutron scattering study. *Biophys. J.* 61:1025–1035.

[190] **Heimburg, T.** and **D. Marsh** (1993). Investigation of secondary and tertiary structural changes of cytochrome c in complexes with anionic lipids using amide hydrogen exchange measurements: an FTIR study. *Biophys. J.* 65:2408–2417.

[191] **Mendelsohn, R.**, **G. Anderle**, **M. Jaworsky**, **H. H. Mantsch** and **R. A. Dluhy** (1984). Fourier transform infrared spectroscopic studies of lipid-protein interaction in native and reconstituted sarcoplasmic reticulum. *Biochim. Biophys. Acta - Biomembranes* 775:215–224.

[192] **Mantsch, H. H.** and **R. N. McElhaney** (1991). Phospholipid phase transitions in model and biological membranes as studied by infrared spectroscopy. *Chem. Phys. Lipids* 57:213–226.

[193] **Heimburg, T.** and **A. D. Jackson** (2007). The Thermodynamics of General Anesthesia. *Biophys. J.* 92:3159–3165.

[194] **Yoshikawa, K.**, **T. Fujimoto**, **T. Shimooka**, **H. Terada**, **N. Kumazawa** and **T. Ishii** (1988). Electrical oscillation and fluctuation in phospholipid membranes : Phospholipids can form a channel without protein. *Biophys. Chem.* 29:293–299.

[195] **Hladky, S.** and **D. Haydon** (1970). Discreteness of Conductance Change in Bimolecular Lipid Membranes in the Presence of Certain Antibiotics. *Nature* 225:451–453.

[196] **Gordon, L. G. M.** and **D. A. Haydon** (1972). The unit conductance channel of alamethicin. *Biochim. Biophys. Acta - Biomembranes* 255:1014–1018.

[197] **Arispe, N.**, **H. B. Pollard** and **E. Rojas** (1996). Zn^{2+} interaction with Alzheimer amyloid beta protein calcium channels. *Proc .Natl. Acad. Sci. USA* 93:1710–1715.

[198] **Gutsmann, T.**, **J. Larrick**, **U. Seydel** and **A. Wiese** (1999). Molecular Mechanisms of Interaction of Rabbit CAP18 with Outer Membranes of Gram-Negative Bacteria. *Biochemistry* 38:13643–13653.

[199] **Rokitskaya, T.**, **Y. Antonenko**, **E. Kotova**, **A. Anastasiadis** and **F. Separovic** (2000). Effect of Avidin on Channel Kinetics of Biotinylated Gramicidin. *Biochemistry* 39:13053–13058.

[200] **Abiror, I. G.**, **V. B. Arakelyan**, **L. V. Chernomordik**, **Y. A. Chizmadzhev**, **V. F. Pastushenko** and **M. R. Tarasevich** (1979). Electric breakdown of bilayer lipid membranes I. The main experimental facts and their qualitative discussion. *Bioelectrochem. Bioenerg.* 6:37–52.

[201] **Glaser, R. W.**, **S. L. Leikin**, **L. V. Chernomordik**, **V. F. Pastushenko** and **A. I. Sokirko** (1988). Reversible electrical breakdown of lipid bilayers: formation and evolution of pores. *Biochim. Biophys. Acta - Biomembranes* 940:275–287.

[202] **Barnett, A.** and **J. C. Weaver** (1991). Electroporation: A unified, quantitative theory of reversible electrical breakdown and mechanical rupture in artificial planar bilayer membranes. *Bioelectroch. Bioenergetics* 25:163–182.

[203] **Gögelein, H.** and **H. Koepsell** (1984). Channels in planar bilayers made from commercially available lipids. *Pflug. Arch. Eur. J. Phy.* 401:433–434.

[204] **Woodbury, D. J.** (1989). Pure lipid vesicles can induce channel-like conductances in planar bilayers. *J.Membrane Biol.* 109:145–150.

[205] **Antonov, V. F.**, **V. V. Petrov**, **A. A. Molnar**, **D. A. Predvoditelev** and **A. S. Ivanov** (1980). The appearance of single-ion channels in unmodified lipid bilayer membranes at the phase transition temperature. *Nature* 283:585–586.

[206] **Boheim, G.**, **W. Hanke** and **H. Eibl** (1980). Lipid Phase Transition in Planar Bilayer Membrane and Its Effect on Carrier- and Pore-Mediated Ion Transport. *Proc .Natl. Acad. Sci. USA* 77:3403–3407.

[207] **Tchoreloff, P.**, **A. Gulik**, **B. Denizot**, **J. E. Proust** and **F. Puisieux** (1991). A structural study of interfacial phospholipid and lung surfactant layers by transmission electron microscopy after Blodgett sampling: influence of surface pressure and temperature. *Chem. Phys. Lipids* 59:151–165.

[208] **Rand, R. P.**, **D. Chapman** and **K. Larsson** (1975). Tilted hydrocarbon chains of dipalmitoyl lecithin become perpendicular to the bilayer before melting. *Biophys. J.* 15:1117–1124.

[209] **Subramaniam, S.** and **H. M. McConnell** (1987). Critical mixing in monolayer mixtures of phospholipid and cholesterol. *J. Phys. Chem.* 91:1715–1718.

[210] **Karnovsky, M.**, **A. Kleinfeld**, **R. Hoover** and **R. Klausner** (1982). The concept of lipid domains in membranes. *J. Cell Biol.* 94:1–6.

[211] **Bagatolli, L. A.** and **E. Gratton** (2000). Two Photon Fluorescence Microscopy of Coexisting Lipid Domains in Giant Unilamellar Vesicles of Binary Phospholipid Mixtures. *Biophys. J.* 78:290–305.

[212] **Samsonov, A. V.**, **I. Mihalyov** and **F. S. Cohen** (2001). Characterization of Cholesterol-Sphingomyelin Domains and Their Dynamics in Bilayer Membranes. *Biophys. J.* 81:1486–1500.

[213] **Veatch, S. L.** and **S. L. Keller** (2003). Separation of Liquid Phases in Giant Vesicles of Ternary Mixtures of Phospholipids and Cholesterol. *Biophys. J.* 85:3074–3083.

[214] **Veatch, S. L.**, **I. V. Polozov**, **K. Gawrisch** and **S. L. Keller** (2004). Liquid Domains in Vesicles Investigated by NMR and Fluorescence Microscopy. *Biophys. J.* 86:2910–2922.

[215] **Bacia, K.**, **D. Scherfeld**, **N. Kahya** and **P. Schwille** (2004). Fluorescence Correlation Spectroscopy Relates Rafts in Model and Native Membranes. *Biophys. J.* 87:1034–1043.

[216] **Bagatolli, L.**, **E. Gratton**, **T. K. Khan** and **P. L.-G. Chong** (2000). Two-Photon Fluorescence Microscopy Studies of Bipolar Tetraether Giant Liposomes from Thermoacidophilic Archaebacteria Sulfolobus acidocaldarius. *Biophys. J.* 79:416–425.

[217] **Seeger, H. M.**, **M. Fidorra** and **T. Heimburg** (2005). Domain Size and Fluctuations at Domain Interfaces in Lipid Mixtures. *Macromol. Symp.* 219:85–96.

[218] **Nagle, J. F.** and **S. Tristram-Nagle** (2000). Structure of lipid bilayers. *Biochimica et Biophysica Acta (BBA) - Reviews on Biomembranes* 1469:159–195.

[219] **Tristram-Nagle, S.**, **R. Zhang**, **R. M. Suter**, **C. R. Worthington**, **W. J. Sun** and **J. F. Nagle** (1993). Measurement of chain tilt angle in fully hydrated bilayers of gel phase lecithins. *Biophys. J.* 64:1097–1109.

[220] **Fidorra, M.** (2004). *Phasenverhalten von Phospholipiden*. Master's thesis, University of Göttingen.

[221] **Dyba, M.** and **S. W. Hell** (2002). Focal Spots of Size λ/23 Open Up Far-Field Florescence Microscopy at 33 nm Axial Resolution. *Phys. Rev. Lett.* 88:163901/1–163901/4.